Spring 2005

Shape Memory Alloy Applications on Control of Thermal Buckling, Panel Flutter and Random Vibration of Composite Panels

Xinyun Guo
Old Dominion University

SHAPE MEMORY ALLOY APPLICATIONS ON CONTROL OF THERMAL BUCKLING, PANEL FLUTTER AND RANDOM VIBRATION OF COMPOSITE PANELS

by

Xinyun Guo
B.S. July 1992, M.S. March 1995, Beijing Institute of Technology

A Dissertation Submitted to the Faculty of
Old Dominion University in Partial Fulfillment of the
Requirement for the Degree of

DOCTOR OF PHILOSOPHY

ENGINEERING MECHANICS

OLD DOMINION UNIVERSITY

May 2005

Approved by:

Chuh Mei (Director)

Osama A. Kandil (member)

Gene J.W. Hou (member)

ABSTRACT

SHAPE MEMORY ALLOY APPLICATIONS ON CONTROL OF THERMAL BUCKLING, PANEL FLUTTER AND RANDOM VIBRATION OF COMPOSITE PANELS

Xinyun Guo
Old Dominion University, 2005
Director: Dr. Chuh Mei

Shape Memory Alloy (SMA) has a unique ability to recover large prestrain (up to 8~10% elongation for Nitinol, a typical SMA material) completely when the alloy is heated (e.g. aerodynamic heating) above the austenite finish temperature A_f. An innovative concept is to utilize the large recovery stress by embedding the prestrained SMA in a traditional fiber-reinforced laminated composite plate, which is called SMA hybrid composite (SMAHC) plate. In this research, static thermal and aerothermal deflections, dynamic panel flutter and random response are investigated for traditional composite plates and SMAHC plates under combined aerodynamic, random and thermal loads by employing nonlinear finite element method. System equations are derived and based on classical laminated plate theory, von Karman nonlinear strain-displacement relation, first-order piston theory aerodynamics and quasi-steady thermal stress theory. Newton-Raphson iterative method is adopted for solving the static thermal and aerothermal buckling deflections. Both normal modes and new proposed aeroelastic modes are employed separately in solution procedures to transform the equations of

motion in structural node degree-of-freedom (DOF) into modal equations of motion. Time domain numerical integration technique is adopted for the dynamic analysis under the combined aerodynamic, random and thermal loads.

Numerical results of isotropic, traditional composite plates and SMAHC plates are determined, compared and discussed. Various plate behaviors are studied in detail. It is demonstrated that SMAHC plates can greatly suppress or reduce thermal buckling and panel flutter as compared with the traditional composite plates. While the SMAHC plates exhibit better performance at low levels of acoustic excitations, however, the SMAHC plates do not effectively suppress random response at high levels of acoustic excitations.

ACKNOWLEDGMENTS

I would like to express my greatest gratitude and appreciation to my academic advisor Dr. Chuh Mei for his priceless guidance, inspiration and encouragement. He has kept showing me a splendid and fantastic academic prospect, in which world he has kept working for more than 40 years. During countless lectures and discussions with him, what I have learned is not only in academic research, but also in the attitudes of life and working. I would not be writing this dissertation with him.

I also want to extend my deepest thanks to my committee members, Dr. Osama A. Kandil and Dr. Gene Hou, for their guidance and suggestions on the dissertation research, and their patience on reviewing the draft. I appreciate all the other faculty and staff members at the Department of Aerospace Engineering for their excellent work and contributions. I'm thankful to the Department of Aerospace Engineering for financial support for my Ph.D. research and study. Great thanks are also given to Adam Przekop and Mohamed S. Azzouz for their friendship and kind help in four years.

I do not know how to express my deepest love to my parents. Memories with my family are always my priceless treasure. The best way to pay back their greatest love is to make successes in my life.

Last but not the least, I want to express my deepest love to my wife, Weining Xu, and my new born daughter, Emily. I am so lucky to have her as my wife, a lovely, considerate and open-minded woman who will share with me the happiness and success, and will ease me when I encounter difficulties and losses.

TABLE OF CONTENTS

LIST OF FIGURES

LIST OF TABLES

LIST OF SYMBOLS

$\{a\}$, $\{b\}$	generalized coordinates
A	element area
A_s	austenite start temperature
A_{ss}, A_m	cross section area of SMA fibers and composite matrix
[A]	laminate in-plane stiffness matrix
$[a_a]$, $[A_a]$	element and system aerodynamic influence matrices
[B]	laminate coupling stiffness matrix
[C]	interpolation function matrix
[D]	laminate bending stiffness matrix
E	Young's modulus
g_a	nondimensional aerodynamic damping coefficient
G	shear modulus
[g], [G]	element and system aerodynamic damping matrices
$[\overline{G}]$	modal aerodynamic damping matrix
h	plate thickness
[H]	displacement function matrix
[k], [K]	element and system stiffness matrices
$[K_{lin}]$	combined system linear stiffness matrix
$[K_1]$, $[K_2]$	combined system first- and second-order nonlinear stiffness matrices
$[K_{tan}]$	system tangent stiffness matrix
$[\overline{K}]$	modal linear stiffness matrix
$[\overline{K}_q]$, $[\overline{K}_{qq}]$	modal nonlinear stiffness matrices

l_s, l_m	width of SMA fibers and composite matrix
L	panel length
M_∞	free stream Mach number
[m], [M]	element and system mass matrices
$[\overline{M}]$	modal mass matrix
{N}, {M}	force and moment resultant vectors
$[n_1]$, $[N_1]$	element and system first-order nonlinear incremental stiffness matrices
$[n_2]$, $[N_2]$	element and system second-order nonlinear incremental stiffness matrices
P_a	aerodynamic pressure
q	dynamic pressure / natural coordinate
{p}, {P}	element and system force vectors
$\{\overline{P}\}$	modal force vector
[Q]	lamina reduced stiffness matrix
$[\overline{Q}]$	transformed lamina reduced stiffness matrix
T	temperature
[T]	transformation matrix
u, v	in-plane displacements
v_s, v_m	volume fractions of SMA fibers and composite matrix
V	airflow velocity
w	transverse displacement
{w}, {W}	element and system node degree-of-freedom vectors
x, y, z	Cartesian coordinates

Greek symbols

α	coefficient of thermal expansion (CTE)
β	$\sqrt{M_\infty^2 - 1}$
Δ	increase value
$\{\varepsilon\}$	strain vector
ϕ	fiber orientation angle
$\{\phi\}$, $\{\Phi\}$	element and system eigenvectors
$[\Phi]$	system eigenvector or modal matrix
$\{\kappa\}$	bending curvature vector
λ	nondimensional dynamic pressure
Λ	flow yawed angle
μ	air-panel mass ratio
ν, ν_{12}, ν_{21}	Poisson's ratios
$[\theta]$	slope matrix
ρ	mass density
$\{\sigma\}$	stress vector
ω	frequency
ζ	structural modal damping ratio

Subscripts

a	air
abs	total

b	bending
cr	critical
m	membrane / composite matrix
NB	stiffness matrices due to in-plane force component $\{N_b\}$
Nm	stiffness matrices due to in-plane force component $\{N_m\}$
NΔT	stiffness matrices due to in-plane force component $\{N_{\Delta T}\}$
r	recovery stress of SMA
s	static / quantity related to SMA
t	time dependent
u, v, w	in-plane and transverse displacements
ΔT	thermal
ε	strain
λ	aerodynamic load
σ	stress

CHAPTER I INTRODUCTION

1.1 Motivations

High-speed flight vehicles cruise at supersonic speeds, causing skin-panel temperatures to potentially reach several hundred degrees due to aerodynamic heating, e.g. maximum 350°F for High Speed Commercial Transport (HSCT) cruising at Mach 2.4 proposed in 1990. The aircraft structure must withstand high thermal load. Large thermal deflections of the skin panels may occur. This would alter the vehicle's configuration and affect its aerodynamic characteristics, leading to poor flight performance. In addition, when the surface area is exposed to engine noise, jet exhaust or shock boundary layer interaction, the skin panels will endure very high acoustic pressure. Typically, the surface thermal protection system (TPS) composed by the skin panels will be exposed to a severe aerodynamic, acoustic and thermal environment. High temperature resistant composite materials with light weight, high stiffness, high structural damping ratio, and high fatigue life are therefore adopted in the TPS. The flight vehicles such as HSCT, X-33 Advanced Technology Demonstrator, the Reusable Launch Vehicle (RLV), and the Joint Strike Fighter (JSF) all will operate at supersonic/hypersonic speeds. The severe flight environment leads to various loads[1], including aerodynamic pressure, acoustic excitation and thermal load, etc. (Fig. 1.1).

The journal model used for this dissertation is AIAA Journal

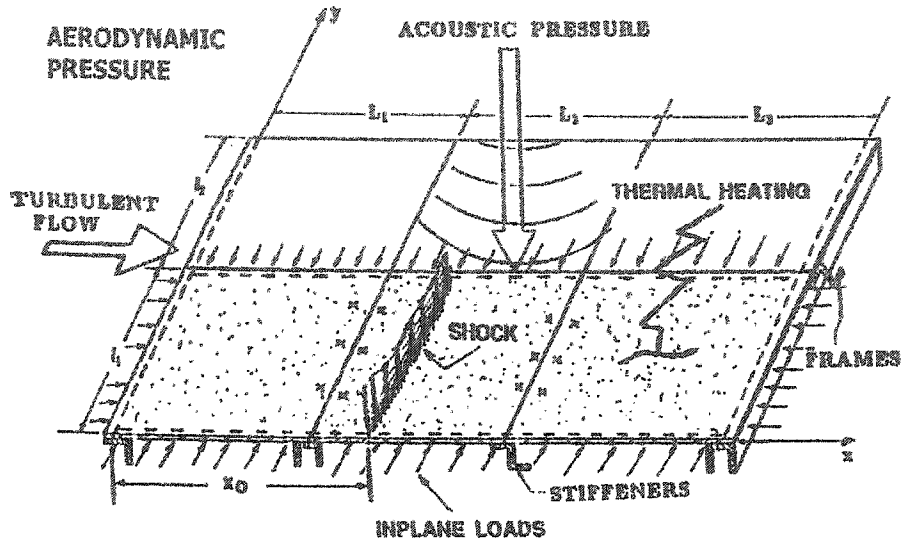

Fig. 1.1 Various loads on surface panels of supersonic/hypersonic flight vehicles[1]

It is also well known that panel flutter occurs resulting from airflow acting on only one side of the surface panel. There exists a critical non-dimensional dynamic pressure λ_{cr} as shown in Fig. 1.2.[2] Below λ_{cr}, the panel undergoes linear random vibration with small amplitudes. The dominant frequency is observed near the lowest natural frequency of the panel. Neglecting structural nonlinearity, linear theory indicates that beyond λ_{cr}, the panel motion becomes unstable and grows exponentially with time. Therefore, nonlinear effect must be considered in vibration analysis beyond λ_{cr}. In fact, the effect of in-plane forces will be significant, and in-plane displacement is coupled with transverse displacement when vibration amplitude becomes large. So the plate motion becomes a bounded limit cycle oscillation (LCO).

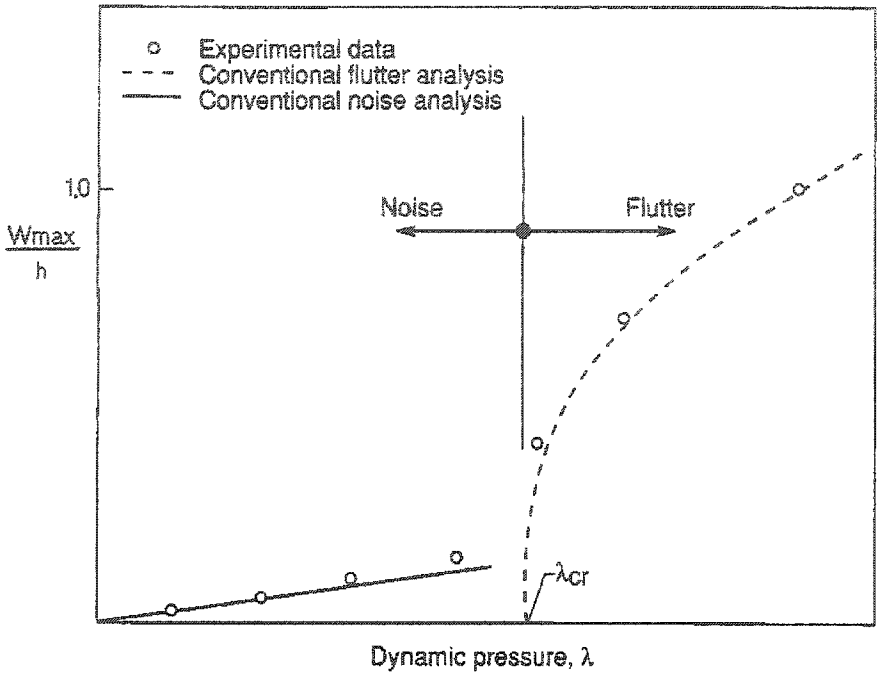

Fig. 1.2 Panel flutter: theory and experiment[2]

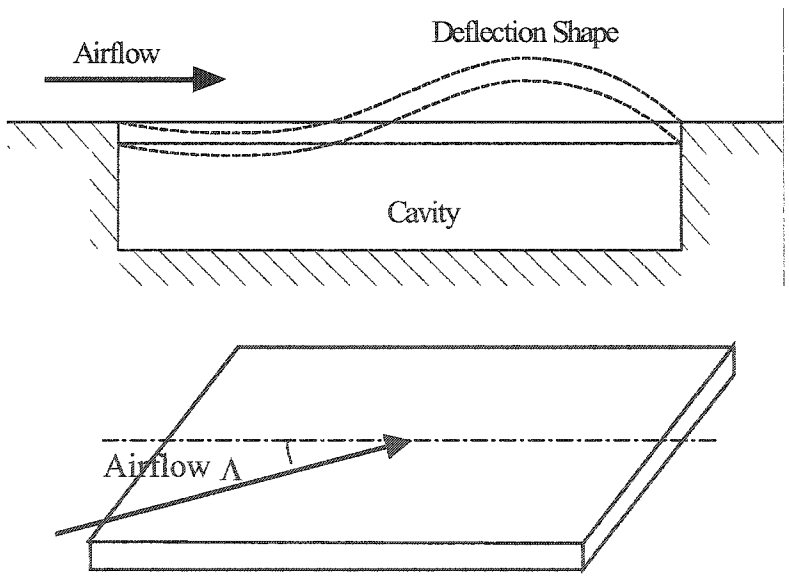

Fig. 1.3 Schematic of panel flutter deflection shape and airflow yaw angle

Another effect of the supersonic flow at $\Lambda = 0$ is that the deflection shape is no longer symmetric with respect to the mid-span of the plate. Furthermore, the airflow can be yawed, that is the direction of airflow has a nonzero angle with respect to the panel x-directions as shown in Fig. 1.3.

It could be expected that the skin panel will undergo various complex types of motion with the combined thermal, aerodynamic and acoustic loads. It is well known that a skin panel with immovable boundary conditions will become thermally buckled if the temperature rise is high; the panel will flutter if airflow speed is high; and the panel will undergo large amplitude nonlinear random vibration at high level acoustic pressure. However, a survey of the literature shows that very few analytical works have been reported on the study of panel response under the three combined loads. Reliable experimental data are difficult and costly to acquire due to difficulties with combined loads of temperature, high Mach number and high acoustic intensity. Thus, it is desirable to develop an improved mathematical and computational prediction method.

Study of panel flutter usually involves the methods of transforming Partial Differential Equations (PDE) into Ordinary Differential Equations (ODE) by using Galerkin's approach or finite element modal method. However, it is still time consuming to acquire a converged solution because a large number of modes have to be used for nonlinear panel flutter analysis with airflow yaw angles involved. Aeroelastic modes are thus developed to reduce the number of modes used in flutter related analysis. This is another motivation of this dissertation.

The investigation of shape memory alloys, which will be introduced in the next section, for the control of thermal buckling, panel flutter and random response under

combined aerodynamic, acoustic and thermal loads is the third motivation of this dissertation.

1.2 Shape Memory Alloys

The term Shape Memory Alloys (SMA) is applied to a group of metallic alloys that can demonstrate the ability to return to some previously defined shape or size when subjected to the appropriate thermal procedure. Generally speaking, these materials can be plastically deformed at some relatively low temperature, and upon exposure to some higher temperature will return to their shape prior to the deformation. It is so called shape memory effect (SME). SME can be described as follows: an object in the low-temperature martensitic phase, when plastically deformed and the external stresses removed, will regain (memorize) its original shape when heated.

A relatively wide variety of alloys are known to exhibit the SME. They are the nickel-titanium alloys and copper-base alloys such as Cu-Al-Ni, Cu-Zn, Cu-Zn-Al, Cu-Zn-Ga, Au-Cd, Ni-Al and Fe-Pt, etc. One of the most common SMA materials is nickel-titanium alloy known as Nitinol (Ni: nickel, ti: titanium, nol: Naval Ordinance Laboratory, now Naval Surface Weapons Center).[3] The advantage of Nitinol is that the prestrain could reach as high as 8-10%, compared with 4-5% of copper-based alloys.

The SME phenomenon is due to the internal crystalline transformations from the low temperature martensite phase to the high temperature austenite phase. The transformation does not occur at a single temperature but over a range of temperatures that varies with each alloy system. The transformation also exhibits hysteresis in that the transformations on heating and on cooling do not overlap. A schematic of the

cooling/heating phase transformation phenomenon is shown in Fig. 1.4. Since this phase transformation is gradual and reversible, a very important state variable in the process is the martensite fraction ξ. There are four temperatures M_f, M_s, A_s, A_f denoting martensite finish, martensite start, austenite start and austenite finish, respectively.

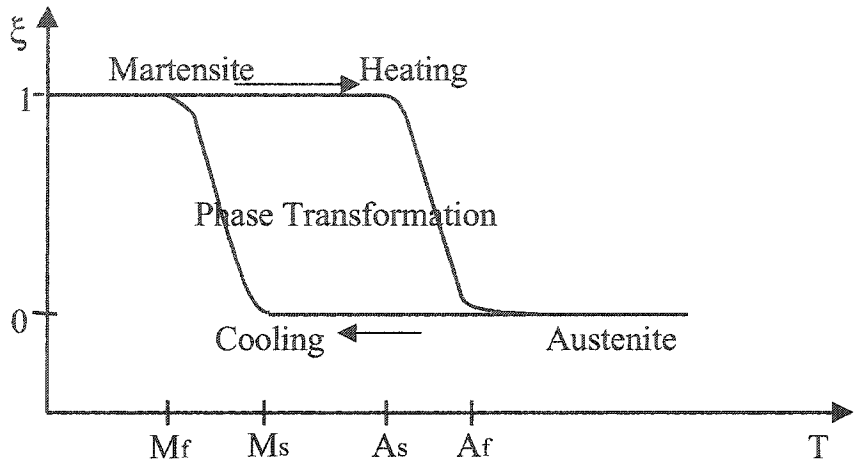

Fig. 1.4 Temperature-driven phase transformation of SMA

The mechanical properties of SMA materials vary greatly over the temperature range spanning their transformation. The martensite is easily deformed to several percent strains at quite a low stress, whereas the austenite has much higher yield stress. During the martensite phase, the internal stress in the SMA changes only slightly and a significant plastic strain is achieved. At $T < A_s$, during the stress-induced martensite phase transformation, a large residual strain ε_r remains after unloading, as shown schematically in Fig. 1.5. This strain can be recovered by heating SMA to temperature $T > A_f$. No such shape recovery is found in the austenite phase upon straining and heating, because no phase change occurs.

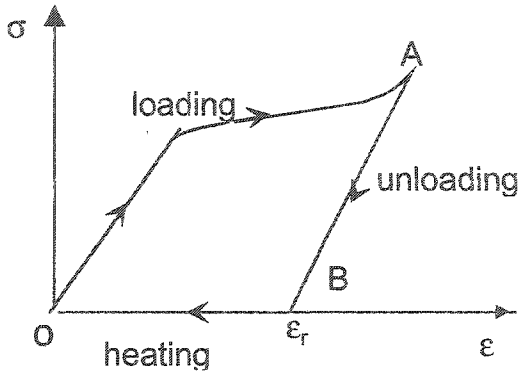

Fig. 1.5 Schematic of shape memory effect ($T < A_s$)

The transformation temperatures of SMA can be varied by the percentage of alloy content.[4] Nitinol A_s temperature versus nickel content is shown in Fig. 1.6. It is seen that with only three percent change of nickel, A_s varies from -50°C to 175°C. This characteristic enables the designers to adjust A_s more flexibly to satisfy the application requirements. One of the characteristics accompanying the phase transformation of Nitinol is Young's modulus.[4] A factor of 3 or 4 of Young's modulus at high temperature over the low temperature is as shown in Fig. 1.7.

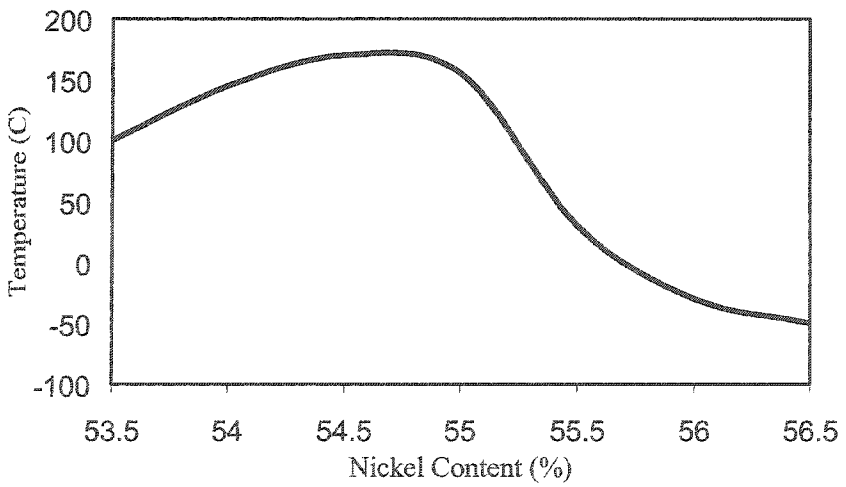

Fig. 1.6 Variation of As with nickel content[4]

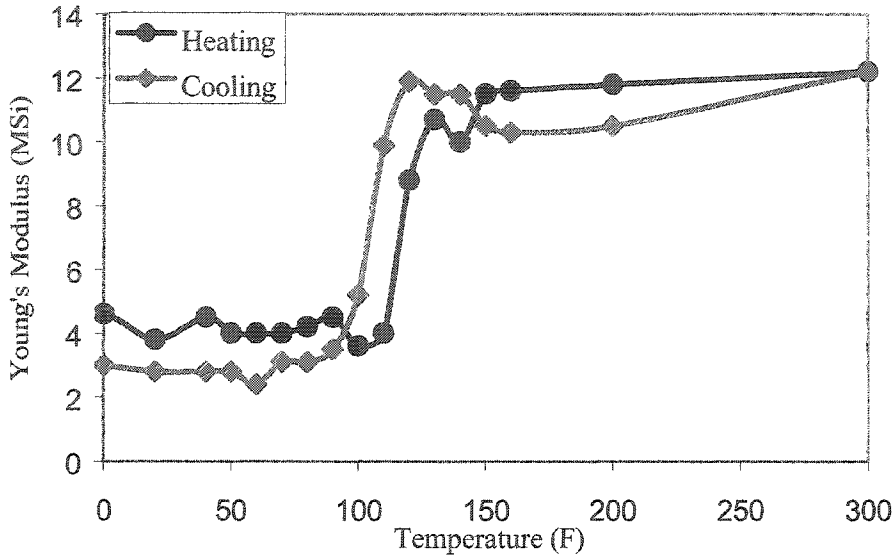

Fig. 1.7 Young's modulus of Nitinol versus temperature[4]

An innovative concept is to utilize the large recovery stress by embedding the prestrained SMA in a fiber-reinforced laminated composite plate.[5] If SMA fibers are loaded and plastically elongated at low temperature ($T < A_s$) during the training process, the fibers will generate martensite residual strain (prestrain ε_r) upon unloading. The treated SMA fibers with prestrain are then embedded inside a traditional composite laminate. The plate is turned into an SMAHC plate. The traditional composite laminate is considered as composite matrix. When the SMA fibers are heated above temperature A_s, since the fibers are restrained by the composite matrix, the tendency of the fibers to return to their normal or memorized length generates a large tensile stress (recovery stress). This stiffening behavior has been experimentally demonstrated with SMAHC beams.[4] The experimental data of recovery stress of Nitinol fibers with various prestrain levels is shown in Fig. 1.8. It is seen that a large recovery stress about 20-80 Ksi (138

MPa-551 MPa) can be generated with prestrain varying from 1% to 10%. The large recovery stress serves as a stiffened in-plane force for the composite structure, therefore plays a key role in the suppression of thermal buckling and vibration. Prestrain of 1%~5% is normally used because the fatigue life of SMA fiber will be quickly reduced at higher prestrains.

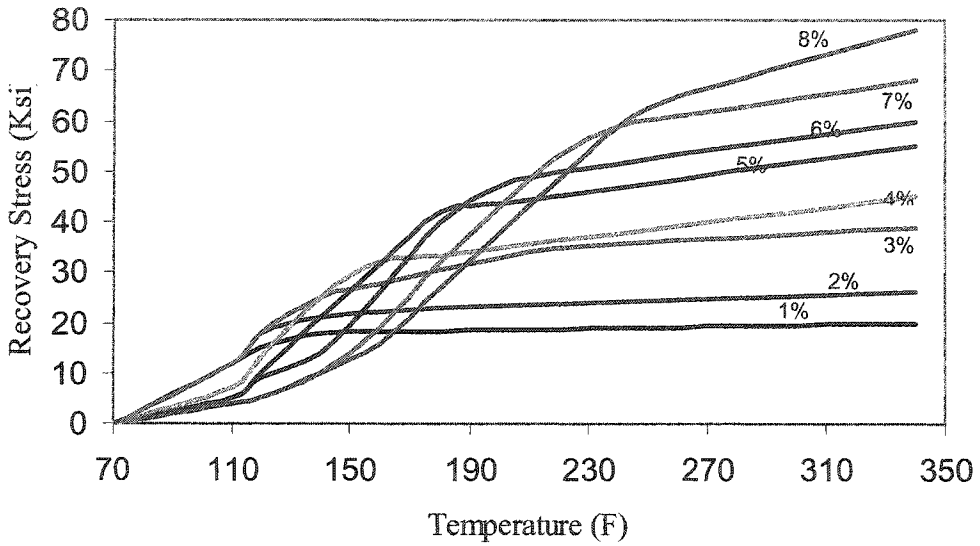

Fig. 1.8 Recovery stress of Nitinol versus temperature with various prestrain levels[4]

1.3 Dissertation Scope

In this dissertation, the static and dynamic response of traditional composite plates and SMAHC plates subjected to the combined aerodynamic, acoustic and thermal loads are studied. Different types of problems are addressed such as thermal bucking and postbuckling, static aerothermal buckling, panel flutter under combined aerodynamic and thermal loads, random response under combined acoustic and thermal loads, and dynamic response under three combined loads.

The documentation of this dissertation is organized as follows. In Chapter I, the general introduction is given about problem description and SMA. Chapter II is the literature survey on static and dynamic problems associated with thermal buckling, flutter and random response of plates. In Chapter III, the constitutive relations for an SMAHC lamina are developed. The stress-strain relations considering thermal effects are derived. The highly nonlinear material properties of SMA obtained from experimental data are taken into consideration. The finite element system governing equations are then derived based on von Karman nonlinear strain-displacement relations and virtual work principle. In Chapter IV, the solution procedures are developed. Newton-Raphson iterative procedure is employed for solving thermal and aerothermal buckling deflections. Two types of modal equations of motion are derived based on normal modes and aeroelastic modes, respectively. In panel flutter problems, dynamic responses are determined by employing an aeroelastic modal method. In random problems, random responses are characterized by Monte Carlo numerical simulation using the traditional normal modes. In chapters V to VIII, examples are presented with numerical results and discussions for thermal and aerothermal buckling (Chapter V), nonlinear panel flutter (Chapter VI), random vibration (Chapter VII), and dynamic response under combined aerodynamic, acoustic and thermal loads (Chapter VIII). They include: i) static thermal buckling deflections due to thermal load only, ii) static aerothermal buckling deflections due to combined aerodynamic and thermal loads, iii) nonlinear panel flutter under combined aerodynamic and thermal loads, iv) random vibration under combined acoustic and thermal loads, and v) dynamic response under combined aerodynamic, acoustic and thermal loads. The results obtained for SMAHC plates are compared with those for

traditional composite panels without SMA fibers. Finally, the concluding remarks and recommendation for future work are presented in Chapter IX.

CHAPTER II LITERATURE SURVEY

2.1 Thermal Buckling and Postbuckling

Thornton[6] did a thorough survey on the works on thermal buckling and postbuckling of plates and shells from the 1950s to 1993. Chia[7] also reviewed the geometrical nonlinear behaviors of composite plates, and addressed the results in static large deflection and postbuckling problems.

Several researchers studied thermal static stability. Hilburger et al.[8] determined the stable equilibrium of structures after the static snap-through occurred using a transient analysis. An initial disturbance was applied to the structure at an unstable equilibrium point so that a new stable equilibrium was obtained after the disturbance was damped out. Irschik[9] presented a Berger-type approximation for large deflections of a thermally loaded and initially curved plate. Bifurcation and snap-through phenomenon was shown and stability of the equilibrium solution was discussed. Birman and Bert[10] considered the thermal response of composite cylindrical shells subjected to compressive axial loads and elevated temperatures. It is showed that the increase of temperature at a constant compressive load could result in a snap-through of the shell to a new equilibrium position. Conditions for the snap-through were also presented.

Since the material properties of SMA are largely dependent on the variation of temperatures, the study of temperature-dependent (TD) material property effects is an important issue. Some researchers studied the effect of TD material properties on thermal buckling and postbuckling. Noor and Peters[11] studied the effects of variation of the elastic moduli, coefficients of thermal expansion (CTE) and fiber orientations of composite lamina on the postbuckling response of composite plates. Noor and Burton[12] reviewed the computational models for high temperature multi-layered composite plates and shells in the applications of heat transfer, thermal stress, bifurcation buckling, large deflection and postbuckling, etc. Effects of temperature-dependence of material properties, and sensitivity of the thermo-mechanical response were discussed in detail. Kamiya and Fukui[13] investigated the finite deflection and postbuckling of square isotropic plates with TD material properties. The finite difference method was employed with iteration solutions for plates in both simply supported and clamped boundary conditions. They concluded that TD material properties would lower the critical buckling temperature, and reduce the postbuckling stiffness and increase the deflection at increased temperatures. Chen and Chen[14,15] proposed a finite element method for thermal buckling and postbuckling behavior of laminated composite plates. Noor and Burton[16] studied the effect of TD material properties on the prebuckling stresses, critical temperatures and their sensitivity derivatives of antisymmetric angle-ply plates using the three-dimensional thermo-elasticity solutions. Numerical results showed that the influence of prebuckling stresses on critical temperature was less significant than the temperature-independent (TI) material property case. Lee and Lee[17] studied the thermal effect for stiffened composite plates with the material degradation on the buckling,

vibration and flutter characteristics using finite element method. It is interesting to note that the above authors[11-17] all assumed a linear relation between material property and temperature, which leads to simpler formulations.

Lee and Choi[18], and Lee, et al.[19] studied the thermal buckling and postbuckling of composite beams and shells with embedded SMA actuators, respectively. Based on the one-dimensional thermo-mechanical constitutive equation of SMA wire actuators, a simple formula was suggested to calculate the critical buckling temperature of a beam once SMA actuator is activated[18]. This constitutive equation of SMA was also incorporated into a finite element model as an ABAQUS subroutine to determine the thermal postbuckling lateral deflections of the beam[18], plate and shell[19]. The results showed an increased critical buckling temperature and reduced lateral deflection. It is also mentioned that the Austenite start temperature is significant in determine the critical temperature. However, the recovery stresses calculated from the theoretical constitutive equation were greatly different as compared with the experimental data. Thompson and Loughlan[20] did manufacturing and experiments of SMA wires embedded laminated panels, as well as a numerical structural finite element analysis using MSC/NASTRAN. The manufacturing methodology of the hybrid SMA carbon/epoxy panel was considered in detail. The panel studied was embedded with 23 0.3mm (0.012 in.) diameter SMA actuators with an initial prestrain 6%. Both experiments and numerical analysis showed that the out-of-plane displacement of the postbuckled laminated panel could be reduced, by utilizing the recovery forces generated from a small SMA actuator volume fraction.

Zhong[21] and Mei et al.[22] utilized an iteration method for the predication of critical temperature with TD material properties. An eigenvalue problem was first formed, and

the calculation was then iterated upon by updating the material properties at the updated temperature until the lowest eigenvalue was converged to 1. By doing so, the dependency of the critical temperature on the initial guess was eliminated. However, this method is not suitable for highly nonlinear or suddenly changed material properties such as SMA. Duan et al.[23] developed an increment-updated Lagrangian method to determine the critical temperature and postbuckling deflection of SMAHC plates. Due to the highly nonlinear dependency of SMA material properties on temperature, the temperature increment began at the reference temperature, at which the plate was assumed to be in a stress-free state (zero initial deflection and stresses). For each small temperature increment, the material properties of the SMA fibers and composite matrix were assumed constant, and the incremental deflection was solved using the Newton-Raphson iteration method. The total deflection was then obtained by adding the incremental deflection to the initial deflection obtained from the previous temperature increment. The initial deflection and initial stresses were then updated and considered in the formulation, and the next temperature increment was introduced. At a temperature that the first large deflection appeared, the plate was therefore becoming thermally buckled. The drawback of this method is that the formulation and solution procedures are quite complicated and computationally time-consuming.

2.2 Nonlinear Panel Flutter

Dowell[2] had an excellent review on both analytical and experimental research aspects of panel flutter in 1975. He grouped the vast amount of theoretical literature on linear and nonlinear panel flutter into four categories. Gary and Mei[24] added the fifth category for hypersonic flow flutter analysis. In 1999, Mei et al.[25] gave a most recent

review of nonlinear panel flutter at supersonic and hypersonic speeds. Cheng[26] pointed out the sixth category would be applying directly the Euler or the Navier-Stoke equations in spite of transonic, supersonic or hypersonic environments. The different categories of linear and nonlinear panel flutter are shown in Table 2.1.

Table 2.1 Panel flutter theories[26]

Type	Structure Theory	Aerodynamic Theory	Range of Mach No.
1	Linear	Linear Piston	$\sqrt{2}<M_\infty<5$
2	Linear	Linearized Potential Flow	$1< M_\infty<5$
3	Nonlinear	Linear Piston	$\sqrt{2}<M_\infty<5$
4	Nonlinear	Linearized Potential Flow	$1< M_\infty<5$
5	Nonlinear	Nonlinear Piston	$M_\infty>5$
6	Nonlinear	Euler or Navier-Stokes Equations	Transonic, Supersonic or Hypersonic

Various classical analysis methods have been employed to study panel flutter. PDE/Galerkin method was the mostly used to reduce the governing partial differential equations to a set of coupled ordinary differential equations by assuming a set of predefined modes which satisfy the geometrical conditions. For the nonlinear flutter of isotropic plate, Dowell[27,28] used the direct numerical integration approach and determined that 6 linear normal modes are required to obtain the converged limit cycle solution. For the flutter analysis of a cantilever plate, Ye and Dowell[29] employed a Rayleigh-Ritz approach with the direct numerical integration and found that the length-to-width ratio of the cantilever plate was a significant factor on flutter vibration. One of the classical analytical methods is harmonic balance method, which needs less computational time

than direct integration, but it is extremely tedious to implement. Kuo et al.[30], Yuen and Lau[31], Eastep and MacIntosh[32] applied this method in their studies. The perturbation method is another method adopted by Morino[33] and Kuo et al..[30]

All the classical studies in nonlinear panel flutter have some limitations: they only can treat isotropic or orthotropic rectangular plates and simple boundary conditions, because it is nearly impossible to make a suitable assumption on shape functions for general composite plates of arbitrary geometry. With the development of finite element techniques, applying finite element method on study of linear panel flutter was first due to Olson.[34,35] He used a frequency domain eigen-solution. Liaw and Yang[36] used a 48 DOF high-order rectangular element and investigated the structural uncertainties occurring during the fabrication process on nonlinear supersonic flutter of laminated composite plates. Han and Yang[37] employed a 54 DOF high-order triangular plate element to study the nonlinear panel flutter of three-dimensional rectangular plates. Dixon and Mei[38] studied the nonlinear flutter of rectangular composite panels. The LCO response was obtained using an extended 24 DOF Bogner-Fox-Schmit (BFS) rectangular plate element and a linearized updated mode with nonlinear time function (LUM/NTF) approximate solution procedure. They found that coalescence may occur between the eigenvalues of the first and third modes, rather than the first and the second modes, for some composite laminates. The LUM/NTF solution procedure in frequency domain was developed by Gray[39]. Xue[40] applied an extended Discrete Kirchhoff theory (DKT) triangular plate element to study nonlinear panel flutter with non-uniform temperature effects. Abdel-Motagaly et al.[41] employed an extended 15 DOF MIN3 triangular element

and studied composite panels subjected to the combined aerodynamic and acoustic pressures.

Flow yaw angle is another issue on flutter analysis. We know that a minimum of six (or 6×1) in-vacuo linear normal modes (NMs) is required for converged LCO of isotropic rectangular plates at supersonic flow speed at zero yaw angle.[27] It is then expected that 6×6 or 36 NMs are needed for isotropic rectangular plates for converged LCO at an arbitrary yawed supersonic flow.[42] Few investigations on LCO have dealt with yawed airflow. Friedmann and Hanin[43] were the first to study nonlinear flutter of rectangular isotropic or orthotropic panels with arbitrary supersonic flow directions. They used the first-order quasisteady aerodynamic theory and Galerkin's method with a 4×2 or eight NMs (four in the x-direction and two in the y-direction) model for panels of simply supported edges. Then numerical integration was employed for the LCO response. Chandiramani et al.[44,45] used the third-order piston theory aerodynamics and the higher-order shear deformation theory and investigated nonperiodic flutter of a buckled composite panel. The yawing of flow was considered, and Galerkin's method with a 2×2 or 4 modes model was employed for simply supported rectangular laminated composite panel. The numerical integration was used for quasi-periodic/chaotic flutter motion. For arbitrary laminated anisotropic composite rectangular plates, Abdel-Motagaly et al.[41] have shown that 36 or less NMs of the lowest natural frequencies are needed for accurate LCO even at zero yaw angle. An efficient iterative eigen-solution procedure was employed for the first time in determination of LCO from the coupled nonlinear modal equations. They have introduced a modal participation value for the selection of those NMs contributing the most to LCO. For nonlinear flutter suppression in controller

design, this would certainly cause complexity and difficulty in dealing with such a large number of NMs.[46,47] This leads to the investigation of whether it is possible to analyze nonlinear panel flutter using some reduced base modeling with fewer number of degrees-of-freedom (DOF), particularly much fewer than the number of NMs. Guo and Mei[48] presented an innovative reduced base method that it is feasible to use a small number of aeroelastic modes (AEMs) for isotropic and composite rectangular plates at zero or arbitrary flow yaw angle for flutter LCO response.

Thermal effects and in-plane loads also play important roles in panel flutter analysis. Houbolt[49] was the first to study the buckling stability and flutter boundaries for two-dimensional panels with uniform temperature distribution. Two linear modes were used for the thermal postbuckling deflection. Dowell[27,28] found that the critical dynamic pressure was reduced and chaotic oscillation might occur with the presence of temperature in establishing the temperature-dynamic pressure stability regions. With the presence of temperature, there are four types of panel behaviors: static flat and stable, aero-thermally buckled but dynamically stable, LCO and chaos. Xue and Mei[50] studied the non-uniform temperature effects on the two- and three-dimensional isotropic panels in arbitrary shapes using DKT element. Yuen and Lau[31] studied the effect of in-plane load on the nonlinear panel flutter with an incremental harmonic balance method. They stated that several LCO at a certain dynamic pressure were possible for a moderately high postbuckling load. Liaw[51] used a 48 DOF rectangular thin-plate finite element to study nonlinear panel flutter under sinusoidal temperature distributions. Zhou[52] transformed the finite element system dynamic equations from the structural node DOF to normal modal coordinates with temperature effects and the results agreed very well with classical

PDE/Gelarkin methods.[27] Nonlinear finite element modal method has gained popularity gradually because it makes it possible using time integration with less computational cost as compared with huge number of structural node DOF.

2.3 Random Vibration

In 1983, Crandall and Zhu[53] published a review article on the progress in random process and random fields, source of excitations, predication of random responses and reliability. Recently, resurgent interest in high-speed flight vehicles necessitates further development of sonic fatigue technology.[54,55] The surface TPS panels of advanced high-speed aircraft and spacecraft would exhibit large displacements under high acoustic loads, and possibly display buckling at elevated temperatures. Both of these effects are nonlinear in nature, and make prediction of fatigue life extremely difficult.[54-56] Experiments were performed to study thermally loaded panels under random excitation by Istenes et al.,[56] Ng and Clevenson[57] and Murphy et al..[58] Snap-through phenomenon and frequency shifting due to nonlinear large amplitude vibration were observed. But reliable experimental data is difficult to acquire at high acoustic intensity and elevated temperature due to costly instrumentation.[59]

There are five major analysis methods: (a) perturbation, (b) Fokker-Plank-Kolmogorov (FPK equation), (c) Monte Carlo, (d) equivalent linearization (EL), and (e) finite element (FE) numerical integration, for the prediction of nonlinear random response of panels.

Perturbation method[60] has been limited to very weak geometric nonlinear problems, thus not suitable for large nonlinear random vibration. FPK method[61] can lead to exact solutions only for single DOF systems. Heuer et al.[62] extended the application of FPK

approach to multi DOF by utilizing a multi-modal projection method. They investigated the nonlinear random vibration of thermally buckled skew plates. The probability of first occurrence of snap-through was determined. The method is tedious to implement. EL method has been widely used because of its ability to accurately capture the response statistics over a wide range of problems while maintaining a relatively low computational burden.[63,64] Ng[65] presented a single-mode method for the analysis of snap-through. He divided the random response with the compressive load larger than the critical value into three regions: no snap-through, intermittent snap-through and persistent snap-through. Lee[66] investigated the effects of thermal variation and thermal moment on the panel response. Locke and Mei,[67] and Mei and Chen[68] extended the finite element method to nonlinear random vibration analysis. The EL method was adopted to the nonlinear finite element modal equations (FE/EL) to determine RMS deflections and strains at different sound pressure levels. The application of EL method depends on the assumption of Gaussian distribution over the response, thus it cannot predict the occurrence of snap-through since snap-through is non-Gaussian in nature.

Monte Carlo simulation[69,70] was employed by Arnold and Vaicaitis,[71] Vaicaitis,[72] Vaicaitis and Kavallieratos[1] to study the nonlinear panel response and fatigue life subjected to acoustic excitation. The PDE/Galerkin method was employed and numerical integration was used to obtain time history of the panel response. Green and Killey[73] studied similar problem, but a narrow-band acoustic loads was used and initial imperfection were considered in the model. The use of PDE/Galerkin approach limits its applicability to rather simple structures.[71,72]

The fifth method is the finite element numerical integration approach, which actually combines the finite element and Monte Carlo simulation method.[73,74] One disadvantage is the computational cost, because the finite element model often includes hundreds, if not thousands, number of physical structural node DOF, and the nonlinear terms are updated and reassembled at each time step. Abdel-Motagaly et al.[41] used finite element numerical integration to study nonlinear panel response under combined aerodynamic and acoustic loads. Finite element system equations of motion were transferred to modal coordinates to reduce the large number of structural node DOF. Dhainaut et al.[75] adopted the same approach, and studied the random response to the acoustic loads at elevated temperatures environment. All the three types of motion can be predicted, which are (i) linear random vibration about one of the two thermally buckled positions, (ii) snap-through between the two buckled positions, and (iii) nonlinear random vibration over the two thermally buckled positions. Przekop[76] extended it to curved panels.

2.4 Combined Aerodynamic, Acoustic and Thermal Loads

For the effects of random acoustic pressure on a nonlinear fluttered plate at supersonic flow, there are very few publications addressing the problem. Eastep and McIntoch[32] studied the panel response under supersonic aerodynamic load, compressive end load (which is similar to thermal load) and random pressure using harmonic balance method and a two-mode approximation. Static deflection and LCO to varying dynamic pressure and compressive end load were studied on the nonlinear behavior from the interaction of the buckling and flutter phenomena. But they did not further investigate chaotic motion. Only small random load was then added into the system, and the panel motion was considered to be a superposition of a previously determined flutter motion

and a small random motion about the flutter motion. Superposition is not suitable for nonlinear analysis. Abdel-Motagaly et al.[41] studied the nonlinear panel response subjected to the combined aerodynamic and acoustic loads using nonlinear finite element modal and time domain integration methods. They showed that only the acoustic pressure needed to be considered if dynamic pressure is much lower than the critical value, whereas the combined loads have to be considered for the dynamic pressure higher than the critical dynamic pressure.

Duan[77] was the first one considered the nonlinear panel response under the combined aerodynamic, acoustic and thermal loads. He used two cases of formulations and solution procedures for panel response of an SMAHC plate. In case 1, the problem was defined for combined thermal load and dynamic pressure only. The Incremental Updated Lagrangian (IUL) method was employed. The drawback is that chaotic motion could not be determined due to a diverged static solution in the chaotic region. In case 2, the problem was for three combined loads, and the time domain integration was employed directly to the system modal equations of motion. The linear normal modes used in the modal reduction procedure.

In this dissertation, the IUL method mentioned above is discarded because of its tedious and time-consuming procedure and the failure in prediction of chaotic motion. The stress-strain constitutive relation is reexamined and expressed by considering the nonlinearity of thermal expansion effect and recovery stress of SMA. A new concept of transforming the system equation of motion into modal coordinated is proposed and validated in introducing aeroelastic modes (AEMs), which can further reduce the number of modes used in the panel flutter analysis.

2.5 SMA Applications

In 1997, Birman[78] reviewed three control concepts in an excellent review article on SMA structures and applications: active property tuning, active energy tuning and active shape control. Rogers et al.[79] studied thermal buckling and postbuckling of the SMAHC plates. They showed that the critical buckling temperature could be greatly increased and the postbuckling deflection could be reduced, by embedding SMA fibers in composite plates. Baz and Tampe,[80] and Baz et al.[81] used SMA in a different way. They placed the Nitinol fibers in resin sleeves, by which the fibers could slide along the sleeve surface. Once the SMA fibers were activated, a pair of concentrated axial force was applied at the two ends of the beam.

On the area of vibration control with SMA, Rogers et al.[82] studied the active strain energy tuning of plates using SMA fibers. Active modal modification was achieved by utilizing stiffness shifting of SMA during temperature activation. Active strain energy tuning utilizes large recovery stresses of SMA. Rogers et al.[83] also studied the structural acoustic control using SMA. Duan et al.[84] studied the frequency variation of the SMAHC plates at elevated temperatures. The results showed that the natural frequencies of SMAHC plates increased greatly compared with the same traditional composite plates without SMA. In addition, modal crossings between the second and the third lowest modes were observed. Suzuki and Degaki[85] studied the suppression of supersonic panel flutter using SMA where an SMA panel was attached on an aluminum base panel. It was demonstrated that the critical air speed or dynamic pressure could be greatly increased. Tawfik et al.[86] investigated the stability regions for the SMAHC plates with various SMA volume fractions and prestrain levels. An enlarged flat and stable region was achieved.

Turner[87] performed both finite element analysis and experiments on random response of an SMAHC beam, and found out that the response could be reduced greatly when SMA fibers were activated.

CHAPTER III FORMULATION

3.1 Introduction

The finite element governing equations for thermal buckling and postbuckling, nonlinear panel flutter and random vibration under the combined thermal, aerodynamic, and acoustic loadings to an SMAHC plate are derived in this chapter.

SMA undergoes phase transformation from martensite to austenite with the increase of temperature, and the process is inversed with the decrease of temperature. Accompanied with this, material properties are greatly varied and large recovery stresses can be generated if SMA fibers are constrained, which can be taken advantage to stiffen the composite plate. The approach is based on the understandings that, first, the thermal strain or deformation is a cumulative physical quantity, because thermal strain or displacement accrues with the increase of temperature; second, stress or force is an instant physical quantity, which can be measured and effective at that particular instant. Therefore, the thermal strain should be an integral of coefficient of thermal expansion (CTE) with respect to temperature, if CTE is a function of temperature. In case CTE is constant, the thermal strain is just the product of CTE and temperature change. However, stress or resultant force and moment is always evaluated with the instant elastic modulus and the total recovery stresses at a given temperature.

To analyze thermal buckling and postbuckling, nonlinear panel flutter problems under the influence of temperature, and random vibration under the three combined loadings, the finite element formulation and solution procedure, which account for the nonlinear properties of SMA as well as temperature-dependent material properties of composite matrix, have been developed and presented.

The following assumptions are considered throughout the derivation:

(1) The panel is thin (L/h > 40). Thus in-plane inertia, rotatory inertia and transverse shear deformation effects are negligible;

(2) von Karman nonlinear strain-displacement relations are valid ($|W_{max}/h| < 5$);

(3) General Hooke's law (elastic range) is valid;

(4) SMA fibers in each lamina are aligned the same direction as the fibers of the traditional composite lamina;

(5) SMA recovery stresses are functions of temperature only, i.e. not functions of internal stresses;

(6) The panel is in a supersonic airflow ($M_\infty > \sqrt{2}$), and the aerodynamic first-order piston theory is valid; and

(7) The quasi-steady state thermal stress theory with uniform temperature distribution is applied.

3.2 Constitutive Relations of an SMAHC Lamina

An SMAHC lamina is composed of traditional composites as matrix and prestrained SMA fibers, as shown in Fig. 3.1.

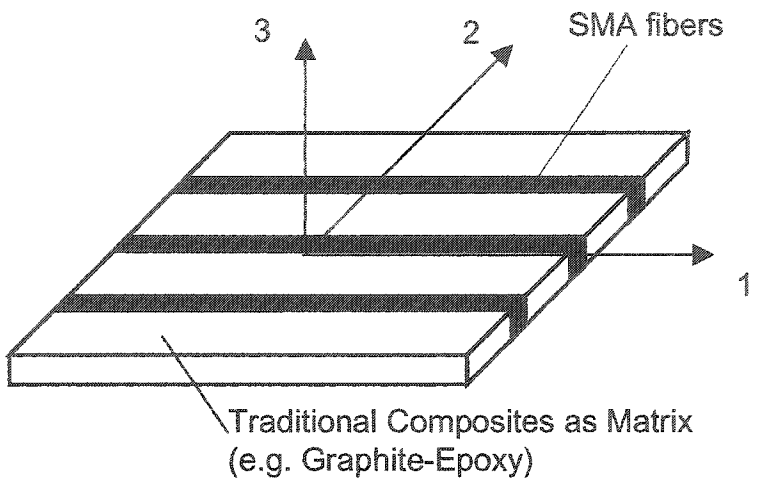

Fig. 3.1 A representative SMAHC lamina

3.2.1 Stress-Strain Relation in 1-Direction (Fiber Direction)

In order to derive the relation in 1-direction, it is assumed that the stress σ_1 acts alone on the lamina with the stress $\sigma_2 = 0$ and the SMA fibers and the composite matrix are strained by the same amount ε_1, as shown in Fig. 3.2.

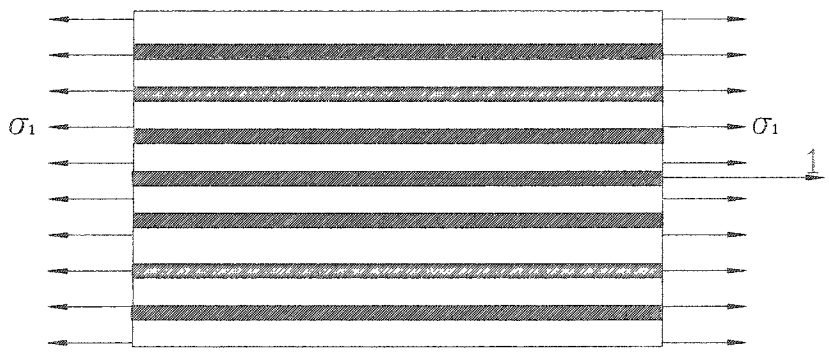

Fig. 3.2 Schematic of an SMAHC lamina under stress in 1-drection

The 1-direction stress-strain relation of the SMA fibers can be described as:

$$\sigma_{1s} = E_s \varepsilon_1 + \sigma_r, \qquad T \geq A_s \tag{3.1}$$

$$\sigma_{1s} = E_s \left(\varepsilon_1 - \int_{T_{ref}}^{T} \alpha_s d\tau \right), \qquad T < A_s \tag{3.2}$$

where A_s is the austenite start temperature, E_s is the Young's modulus, σ_r is the recovery stress, α_s is the CTE of SMA fibers, and subscript s denotes the SMA fibers. An integral is used to account for thermal strain since the CTE is a function of the temperature. In case CTE is constant, $\int_{T_{ref}}^{T} \alpha_s d\tau = \alpha_s \Delta T$. It is seen that when $T \geq A_s$, the recovery stress σ_r is activated. The SMA fibers are restrained not to return to their original length, and thermal expansion effect is included in the test data of σ_r. The value of σ_r depends on the temperature and SMA prestrain. When $T < A_s$, the SMA fibers have the same behavior as those of common alloys. E_s and σ_r are temperature-dependent, and σ_r is also dependent on the prestrain ε_r.

The 1-direction stress-strain relation for the composite matrix can be expressed as:

$$\sigma_{1m} = E_{1m} \left(\varepsilon_1 - \int_{T_{ref}}^{T} \alpha_{1m} d\tau \right) \tag{3.3}$$

where the subscript m denotes the composite matrix.

The resultant force in 1-direction is distributed over the SMA fibers and the composite matrix, which can be written as:

$$\sigma_1 A_1 = \sigma_{1s} A_{ss} + \sigma_{1m} A_m \tag{3.4}$$

where (σ_1, A_1), (σ_{1s}, A_{ss}) and (σ_{1m}, A_m) are the stress and cross section area of the SMAHC lamina, the SMA fibers, and the composite matrix, respectively. Thus, the average stress σ_1 is:

$$\sigma_1 = \sigma_{1s} v_s + \sigma_{1m} v_m \tag{3.5}$$

where $v_s = A_{ss}/A_1$, $v_m = A_m/A_1$ are the volume fractions of the SMA fibers and the composite matrix, respectively.

When $T \geq A_s$, by substituting Eqs. (3.1, 3.3) into Eq. (3.5), σ_1 becomes:

$$\begin{aligned} \sigma_1 &= \left(E_s \varepsilon_1 + \sigma_r\right) v_s + E_{1m}\left(\varepsilon_1 - \int_{T_{ref}}^{T} \alpha_{1m} d\tau\right) v_m \\ &= E_1 \varepsilon_1 + \sigma_r v_s - E_{1m} v_m \int_{T_{ref}}^{T} \alpha_{1m} d\tau \end{aligned} \tag{3.6}$$

where the Young's modulus of the SMAHC lamina in 1-direction is:

$$E_1 = E_s v_s + E_{1m} v_m \tag{3.7}$$

When $T < A_s$, by substituting Eq. (3.2) into Eq. (3.5), σ_1 becomes:

$$\begin{aligned} \sigma_1 &= E_s\left(\varepsilon_1 - \int_{T_{ref}}^{T} \alpha_s d\tau\right) v_s + E_{1m}\left(\varepsilon_1 - \int_{T_{ref}}^{T} \alpha_{1m} d\tau\right) v_m \\ &= E_1\left(\varepsilon_1 - \alpha_1 \Delta T\right) \end{aligned} \tag{3.8}$$

where the average combined CTE of the SMAHC lamina between T_{ref} and T is:

$$\alpha_1 = \frac{E_s \int_{T_{ref}}^{T} \alpha_s d\tau v_s + E_{1m} \int_{T_{ref}}^{T} \alpha_{1m} d\tau v_m}{E_1 \Delta T} \tag{3.9}$$

3.2.2 Stress-Stain Relation in 2-Direction

Assume there is no large volume change representative of diffusion phase changes and therefore no effect on the dimension in directions other than fiber direction beyond Poisson's contractions. Similarly, for an SMAHC lamina under the stress in 2-drection, as shown in Fig. 3.3, the stress-strain relations in 2-direction for the SMA fibers and the composite matrix become:

$$\sigma_{2s} = \sigma_2 = E_s\left(\varepsilon_{2s} - \int_{T_{ref}}^{T} \alpha_s d\tau\right) \tag{3.10}$$

$$\sigma_{2m} = \sigma_2 = E_{2m}\left(\varepsilon_{2m} - \int_{T_{ref}}^{T} \alpha_{2m} d\tau\right) \tag{3.11}$$

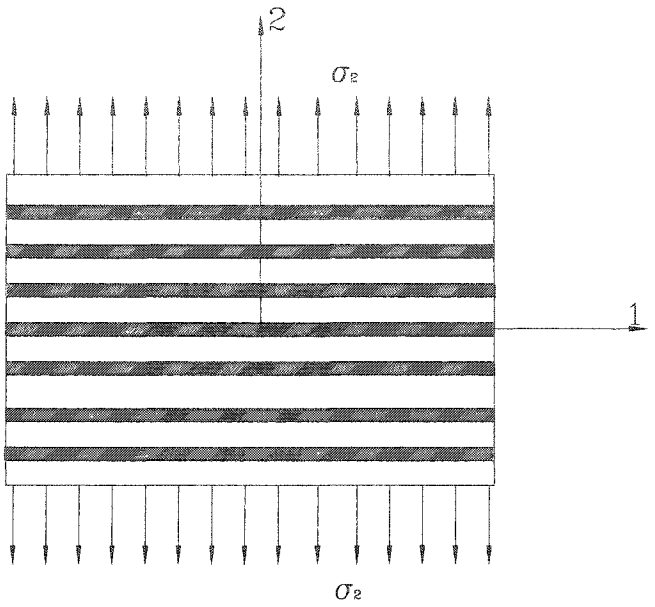

Fig. 3.3 Schematic of an SMAHC lamina under the stress in 2-drection

The total elongation of the composite lamina in 2-direction is the summation of the elongation of the SMA fibers and the composite matrix:

$$l\varepsilon_2 = l_s\varepsilon_{2s} + l_m\varepsilon_{2m} \tag{3.12}$$

where l, l_s and l_m are the widths in 2-direction of the SMAHC lamina, the SMA fibers and the composite matrix, respectively. Equation (3.12) can be written as:

$$\varepsilon_2 = \varepsilon_{2s} l_s / l + \varepsilon_{2m} l_m / l \tag{3.13}$$

Then the total strain in 2-direction becomes:

$$\varepsilon_2 = \varepsilon_{2s} v_s + \varepsilon_{2m} v_m \tag{3.14}$$

Since $\sigma_2 = \sigma_{2s} = E_s(\varepsilon_{2s} - \int_{T_{ref}}^{T} \alpha_s d\tau)$, Eqs. (3.13, 2.14) can be substituted into Eq. (3.10) to give:

$$\sigma_2 = E_2\left(\varepsilon_2 - \int_{T_{ref}}^{T} (\alpha_s v_s + \alpha_{2m} v_m) d\tau\right) \tag{3.15}$$

where the combined Young's modulus of the SMAHC lamina in 2-direction is:

$$E_2 = \frac{E_s E_{2m}}{E_s v_m + E_{2m} v_s} \tag{3.16}$$

We can define α_2 as the average combined CTE of the SMAHC lamina in 2-direction between T_{ref} and T, and it is given as:

$$\alpha_2 = \frac{\int_{T_{ref}}^{T} (\alpha_s v_s + \alpha_{2m} v_m) d\tau}{\Delta T} \tag{3.17}$$

3.2.3 Two-Dimensional Stress-Strain Relation

The two-dimensional stress-strain relation for an SMAHC lamina can be derived and expressed as two parts, one for $T < A_s$ and the other for $T \geq A_s$. The reason is that when $T \geq A_s$, the recovery stress σ_r is activated and accounted separately. When $T < A_s$, the SMA fibers is treated to have the same behavior as those of common alloys and thus accounted for by mixing with composite lamina.

$$\begin{Bmatrix} \sigma_1 \\ \sigma_2 \\ \tau_{12} \end{Bmatrix} = \begin{bmatrix} Q_{11} & Q_{12} & 0 \\ Q_{12} & Q_{22} & 0 \\ 0 & 0 & Q_{66} \end{bmatrix} \begin{Bmatrix} \varepsilon_1 \\ \varepsilon_2 \\ \gamma_{12} \end{Bmatrix} + \begin{Bmatrix} \sigma_r \\ 0 \\ 0 \end{Bmatrix} v_s - \begin{bmatrix} Q_{11m} & Q_{12m} & 0 \\ Q_{12m} & Q_{22m} & 0 \\ 0 & 0 & Q_{66m} \end{bmatrix} \int_{T_{ref}}^{T} \begin{Bmatrix} \alpha_{1m} \\ \alpha_{2m} \\ 0 \end{Bmatrix} d\tau v_m, \quad T \geq A_s \tag{3.18}$$

$$= [Q]\{\varepsilon\} + \{\sigma_r\} v_s - [Q_m] \int_{T_{ref}}^{T} \{\alpha_m\} d\tau \, v_m$$

$$\begin{Bmatrix}\sigma_1\\ \sigma_2\\ \tau_{12}\end{Bmatrix}=\begin{bmatrix}Q_{11} & Q_{12} & 0\\ Q_{12} & Q_{22} & 0\\ 0 & 0 & Q_{66}\end{bmatrix}\left(\begin{Bmatrix}\varepsilon_1\\ \varepsilon_2\\ \gamma_{12}\end{Bmatrix}-\begin{Bmatrix}\alpha_1\\ \alpha_2\\ 0\end{Bmatrix}\Delta T\right), \qquad T < A_s$$

$$=[Q](\{\varepsilon\}-\{\alpha\}\Delta T) \tag{3.19}$$

where [Q] and [Q_m] are the reduced stiffness matrices of the SMAHC lamina and the matrix, respectively. It is noticed that the CTEs α_1 and α_2 in Eq. (3.19) are the averaged value determined by Eqs. (3.9) and (3.17), respectively. The terms in [Q] can be evaluated[88] as:

$$Q_{11}=\frac{E_1}{1-\mu_{12}\mu_{21}}$$

$$Q_{12}=\frac{\mu_{12}E_2}{1-\mu_{12}\mu_{21}}=\frac{\mu_{21}E_1}{1-\mu_{12}\mu_{21}}$$

$$Q_{22}=\frac{E_2}{1-\mu_{12}\mu_{21}}$$

$$Q_{66}=G_{12} \tag{3.20}$$

$$E_1=E_s v_s+E_{1m}v_m$$

$$\mu_{12}=\mu_s v_s+\mu_{12m}v_m$$

$$E_2=\frac{E_s E_{2m}}{E_s v_m+E_{2m}v_s}$$

$$G_{12}=\frac{G_s G_{12m}}{G_s v_m+G_{12m}v_s}$$

where μ's are Possion's ratios, and G's are the shear moduli.

3.3 Constitutive Relations of an SMAHC plate

An SMAHC plate is composed of many layers of lamina as shown in Fig. 3.4. Each lamina has one orientation angle ϕ, which is the angle between the principle 1-direction of the lamina and the plate coordinate axis x.

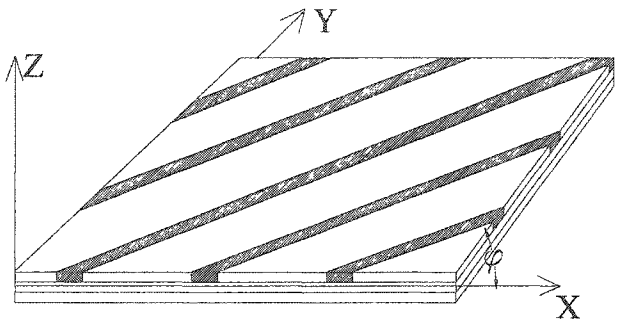

Fig. 3.4 A representative SMAHC plate with 3 layers of lamina

For the SMAHC lamina with an orientation angle ϕ, the stress and strain transformation relations from the principal directions 1, 2 to the x, y directions are:

$$\begin{Bmatrix}\sigma_1\\ \sigma_2\\ \tau_{12}\end{Bmatrix}=[T_\sigma(\phi)]\begin{Bmatrix}\sigma_x\\ \sigma_y\\ \tau_{xy}\end{Bmatrix},\qquad \begin{Bmatrix}\varepsilon_1\\ \varepsilon_2\\ \gamma_{12}\end{Bmatrix}=[T_\varepsilon(\phi)]\begin{Bmatrix}\varepsilon_x\\ \varepsilon_y\\ \gamma_{xy}\end{Bmatrix} \tag{3.21}$$

where

$$[T_\sigma(\phi)]=\begin{bmatrix}c^2 & s^2 & 2sc\\ s^2 & c^2 & -2sc\\ -sc & sc & c^2-s^2\end{bmatrix},\qquad [T_\varepsilon(\phi)]=\begin{bmatrix}c^2 & s^2 & sc\\ s^2 & c^2 & -sc\\ -2sc & 2sc & c^2-s^2\end{bmatrix} \tag{3.22}$$

where c=cosϕ, s=sinϕ.

The transformed reduced stiffness matrices are:

$$[\bar{Q}]=[T_\sigma(\phi)]^{-1}[Q][T_\varepsilon(\phi)],\qquad [\bar{Q}_m]=[T_\sigma(\phi)]^{-1}[Q_m][T_\varepsilon(\phi)]$$

$$\begin{Bmatrix}\sigma_{xr}\\ \sigma_{yr}\\ \tau_{xyr}\end{Bmatrix}=[T_\sigma(\phi)]^{-1}\begin{Bmatrix}\sigma_r\\ 0\\ 0\end{Bmatrix},\quad \begin{Bmatrix}\alpha_{xm}\\ \alpha_{ym}\\ \alpha_{xym}\end{Bmatrix}=[T_\varepsilon(\phi)]^{-1}\begin{Bmatrix}\alpha_{1m}\\ \alpha_{2m}\\ 0\end{Bmatrix},\quad \begin{Bmatrix}\alpha_x\\ \alpha_y\\ \alpha_{xy}\end{Bmatrix}=[T_\varepsilon(\phi)]^{-1}\begin{Bmatrix}\alpha_1\\ \alpha_2\\ 0\end{Bmatrix} \tag{3.23}$$

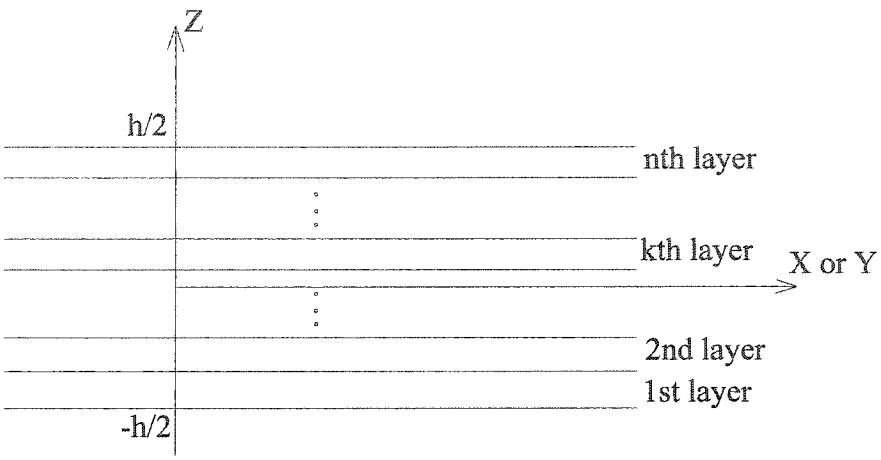

Fig. 3.5 Schematic of a general n layer SMAHC plate

Thus, the stress-strain relation for a general k[th] lamina as shown in Fig. 3.5 with an orientation angle ϕ becomes:

$$\{\sigma\}_k=\begin{Bmatrix}\sigma_x\\ \sigma_y\\ \sigma_{xy}\end{Bmatrix}_k=[\bar{Q}]_k\begin{Bmatrix}\varepsilon_x\\ \varepsilon_y\\ \gamma_{xy}\end{Bmatrix}+\begin{Bmatrix}\sigma_{xr}\\ \sigma_{yr}\\ \tau_{xyr}\end{Bmatrix}_k v_{sk}-[\bar{Q}_m]_k\int_{T_{ref}}^{T}\begin{Bmatrix}\alpha_{xm}\\ \alpha_{ym}\\ \alpha_{xym}\end{Bmatrix}_k d\tau v_m,\ T\geq A_s \tag{3.24}$$

$$\{\sigma\}_k=\begin{Bmatrix}\sigma_x\\ \sigma_y\\ \sigma_{xy}\end{Bmatrix}_k=[\bar{Q}]_k\left(\begin{Bmatrix}\varepsilon_x\\ \varepsilon_y\\ \gamma_{xy}\end{Bmatrix}-\begin{Bmatrix}\alpha_x\\ \alpha_y\\ \alpha_{xy}\end{Bmatrix}_k\Delta T\right),\qquad T<A_s \tag{3.25}$$

where subscript k denotes the general k[th] layer; $\lfloor\sigma_{xr}, \sigma_{yr}, \tau_{xyr}\rfloor_k^T$ are the recovery stress vector.

In the derivation of equations of motion, it is assumed that the panel is thin, i.e., the ratio of length or width over thickness is greater than 50. The rotary inertia and

transverse shear deformation effects are thus negligible. The relation between the total strain vector $\{\varepsilon\}$, and in-plane strains $\{\varepsilon^o\}$ and curvatures $\{\kappa\}$ based on classical plate theory is given by:

$$\{\varepsilon\} = \{\varepsilon^o\} + z\{\kappa\} \tag{3.26}$$

The in-plane strain vector $\{\varepsilon^o\}$ consists of two parts: mid-surface inplane strain and von Karman large deflection strain:

$$\{\varepsilon^o\} = \{\varepsilon_m^o\} + \{\varepsilon_\theta^o\} = \begin{Bmatrix} \dfrac{\partial u}{\partial x} \\ \dfrac{\partial v}{\partial y} \\ \dfrac{\partial u}{\partial y} + \dfrac{\partial v}{\partial y} \end{Bmatrix} + \frac{1}{2}\begin{Bmatrix} \left(\dfrac{\partial w}{\partial x}\right)^2 \\ \left(\dfrac{\partial w}{\partial y}\right)^2 \\ 2\dfrac{\partial w}{\partial x}\dfrac{\partial w}{\partial y} \end{Bmatrix} \tag{3.27}$$

and the bending curvature vector $\{\kappa\}$ is:

$$\{\kappa\} = \begin{Bmatrix} -\dfrac{\partial^2 w}{\partial x^2} \\ -\dfrac{\partial^2 w}{\partial y^2} \\ -2\dfrac{\partial^2 w}{\partial x \partial y} \end{Bmatrix} \tag{3.28}$$

where u, v, w are in-plane and bending displacements, respectively.

The resultant force and moment vectors per unit length are defined as:

$$(\{N\}, \{M\}) = \int_{-h/2}^{h/2} \{\sigma\}_k (1, z)\, dz \tag{3.29}$$

or

$$\begin{Bmatrix} N \\ M \end{Bmatrix} = \begin{bmatrix} A & B \\ B & D \end{bmatrix} \begin{Bmatrix} \varepsilon^o \\ \kappa \end{Bmatrix} + \begin{Bmatrix} N_r \\ M_r \end{Bmatrix} - \begin{Bmatrix} N_{\Delta T} \\ M_{\Delta T} \end{Bmatrix} \tag{3.30}$$

where [A], [B], and [D] are the laminate stiffness matrices. They are defined as:

$$A_{ij} = \int_{-h/2}^{h/2} \left(\overline{Q}_{ij}\right)_k dz, \quad i,j = 1,2,6$$

$$B_{ij} = \int_{-h/2}^{h/2} \left(\overline{Q}_{ij}\right)_k z dz, \quad i,j = 1,2,6 \tag{3.31}$$

$$D_{ij} = \int_{-h/2}^{h/2} \left(\overline{Q}_{ij}\right)_k z^2 dz, \quad i,j = 1,2,6$$

The vectors $\{N_r\}$, $\{M_r\}$, $\{N_{\Delta T}\}$ and $\{M_{\Delta T}\}$ are the resultant force and moment vectors per unit length, which are due to the recovery stress and thermal stress, respectively. They can be expressed as:

$$\begin{aligned}\left(\{N_r\},\{M_r\}\right) &= \int_{-h/2}^{h/2} \begin{Bmatrix} \sigma_{xr} \\ \sigma_{yr} \\ \tau_{xyr} \end{Bmatrix}_k v_{sk}(1, z)dz, \qquad T \geq A_s \\ &= 0, \qquad\qquad\qquad\qquad T < A_s \end{aligned} \tag{3.32}$$

$$\begin{aligned}\left(\{N_{\Delta T}\},\{M_{\Delta T}\}\right) &= \int_{-h/2}^{h/2} \left[\overline{Q}_m\right]_k \int_{T_{ref}}^{T} \begin{Bmatrix} \alpha_{xm} \\ \alpha_{ym} \\ \alpha_{xym} \end{Bmatrix}_k d\tau v_m(1, z)dz, \qquad T \geq A_s \\ &= \int_{-h/2}^{h/2} \left[\overline{Q}\right]_k \begin{Bmatrix} \alpha_x \\ \alpha_y \\ \alpha_{xy} \end{Bmatrix}_k \Delta T(1, z)dz, \qquad T < A_s \end{aligned} \tag{3.33}$$

3.4 Quasisteady First-Order Piston Aerodynamic Theory

Quasisteady first-order piston theory is a verified aerodynamic model,[2] which has been successfully applied to panel flutter studies. This theory describes the aerodynamic pressure on a skin panel of a flight vehicle at supersonic airflow. The theory is based on the assumption that: a) the local motion of the panel acts as a piston; b) the air is ideal and it has a constant specific heat; the process of the airflow is isentropic; c) the local panel motion velocity is much smaller than the airflow velocity; d) The airflow is parallel

to the panel surface; and e) the effect of any air entrapped below the panel (cavity) is neglected.

The first-order piston theory considering flow yaw angle is:

$$P_a = -\frac{2q}{\beta}\left[\frac{\partial w}{\partial x}\cos\Lambda + \frac{\partial w}{\partial y}\sin\Lambda + \frac{M_\infty^2 - 2}{M_\infty^2 - 1}\frac{1}{V}\frac{\partial w}{\partial t}\right] \tag{3.34}$$

where P_a is the aerodynamic pressure, V is the airflow velocity, M_∞ is the Mach number, $q = \frac{1}{2}\rho_a V^2$ is the dynamic pressure, Λ is the flow yaw angle with respect to plate x-direction, ρ_a is the air mass density, $\beta = \sqrt{M_\infty^2 - 1}$, w is the panel transverse displacement.

Equation (3.34) can also be written as:

$$P_a = -\left[\lambda\frac{D_{110}}{L^3}\left(\frac{\partial w}{\partial x}\cos\Lambda + \frac{\partial w}{\partial y}\sin\Lambda\right) + \frac{g_a}{\omega_o}\frac{D_{110}}{L^4}\frac{\partial w}{\partial t}\right] \tag{3.35}$$

where D_{110} is the first element in the laminate bending stiffness matrix [D] calculated when all the fibers of the SMAHC plate are aligned in the x-direction; L is the panel length; non-dimensional dynamic pressure λ, mass flow μ, non-dimensional aerodynamic damping g_a and its coefficient C_a, and reference frequency ω_o are given respectively by:

$$\begin{aligned}
\lambda &= \frac{2qL^3}{\beta D_{110}} \\
\mu &= \frac{\rho_a a}{\rho h} \\
C_a &= \left(\frac{M_\infty^2 - 2}{M_\infty^2 - 1}\right)^2 \frac{\mu}{\beta} \\
g_a &= \frac{\rho_a V\left(M_\infty^2 - 2\right)}{\beta^3 \rho h \omega_o} = \sqrt{\lambda C_a} \\
\omega_o &= \sqrt{\frac{D_{110}}{\rho h L^4}}
\end{aligned} \tag{3.36}$$

For an SMAHC panel, the values of ρ, D_{110} and ω_0 will change with different volume fractions of SMA. The parameters ρ, D_{110} and ω_0 are only served to transfer the coefficients in Eq. (3.34) into non-dimensional ones. For the purpose of comparison, dynamic pressure should be consistent for plate with or without SMA. Therefore, the parameters ρ, D_{110} and ω_0 are taken to be the values when the panel is a traditional composite ($v_m = 1$) with no SMA ($v_s = 0$). The comparison between composite plates with and without SMA is therefore meaningful.

3.5 Random Pressure Generation

When a vehicle flights at supersonic speeds, the skin panels will be exposed not only to temperature elevation and the aerodynamic pressure that lead to flutter, but also to the intense non-stationary pressures, such as turbulent boundary layer flow, engine noise and shocks, etc. These loads are usually accounted for in the form of random excitation pressures.

In this study, the random loads are assumed as stationary and Gaussian, and uniformly distributed over the panel surface. The random input is also assumed acting normally to the panel surface. Actually, for the time domain numerical integration method employed in this study, there is no restriction on the random input excitation. It can be Gaussian or non-Gaussian, as long as the time history is available.

The random pressure P(x,y,t) is characterized by a cross-spectrum density function $S_p(\xi,\eta,f)$, where $\xi = x_1 - x_2$, $\eta = y_1 - y_2$ are the spectral separations, and f is frequency in Hz. S_p can be obtained utilizing experimental data. By assumption, the cross-spectrum density of a truncated Gaussian white noise pressure uniformly distributed with spatial coordinates x and y is:

$$S_p(\xi,\eta,f)=\begin{cases} S_o = p_o^2 10^{SPL/10}, & 0 \le f \le f_u \\ 0, & f<0 \text{ or } f>f_u \end{cases} \tag{3.39}$$

where S_o is a constant, p_o is a reference pressure, $p_o = 2.9020\times10^{-9}$ Psi (20 μPa), SPL is sound pressure level in decibels, and f_u is upper cutoff frequency in Hz.

Shinozuka and Jan,[69] and Vaicaitis[72] utilized Fourier transformation to obtain random pressure P(t) (assumed uniform distribution on the panel, independent on x and y) for the given S_o and f_u by writing P(t) as a series of cosine functions with weighted amplitudes, almost evenly spaced frequencies, and random phase angles. The generated P(t) is treated as input. The Runge-Kutta integration is employed to obtain the displacement response. Utilizing Fortran or Matlab, Gaussian random pressure can be easily generated by calling functions. For Matlab, the Gaussian random pressure P with zero mean and power PW is expressed as:

$$P = sqrt(PW)\cdot randn([n,1]) \tag{3.40}$$

where *randn* is Gaussian random number generation function, n is the amount of random number need to be generated. For numerical integration, it is equal to time duration divided by time step. The power can be calculated from auto-spectrum density S_o and upper cutoff frequency f_u as

$$PW = S_o \cdot f_u \tag{3.41}$$

Accordingly, the overall SPL (OASPL) is just the power in the unit of dB and expressed as the summation of SPL and 10(log f_u). The time history, PSD and PDF of a typical simulated random load are shown in Fig. 3.6 with a cut-off frequency of 1024 Hz and SPL of 100 dB, which correspond to an OASPL of 130 dB.

The cutoff frequency f_u should be selected so that it not only covers the highest natural frequency in the simulation, but also considers the frequency shifting effect due to nonlinear large vibration. Generally speaking, the f_u should be selected at least twice the highest linear frequency.

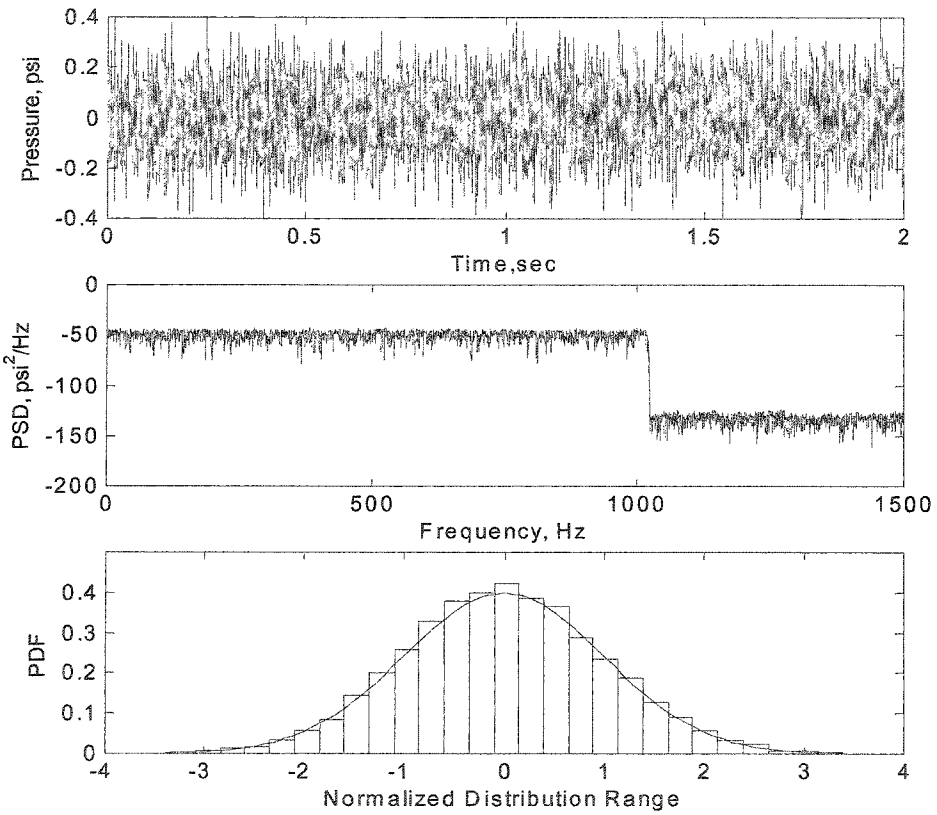

Fig. 3.6 Simulation of Band-Limited White Noise with SPL = 100 dB and f_u = 1024 Hz

3.6 Equations of Motion in Finite Element Formulation

3.6.1 Finite Element Expressions

Bogner-Fox-Schmit (BFS)[89] C^1 conforming rectangular element is extended and adopted in the study. As shown in Fig. 3.7, there are 16 bending degrees of freedom (DOF), $\{w_b\}_{16\times1}$, and 8 in-plane DOF, $\{w_m\}_{8\times1}$, in each element. They are expressed as:

$$\{w_b\}=\{w_1\ w_2\ w_3\ w_4\ w_{,x_1}\ w_{,x_2}\ w_{,x_3}\ w_{,x_4}\ w_{,y_1}\ w_{,y_2}\ w_{,y_3}\ w_{,y_4}\ w_{,xy_1}\ w_{,xy_2}\ w_{,xy_3}\ w_{,xy_4}\}^T$$

$$\{w_m\}=\{u_1\ u_2\ u_3\ u_4\ v_1\ v_2\ v_3\ v_4\}^T \tag{3.42}$$

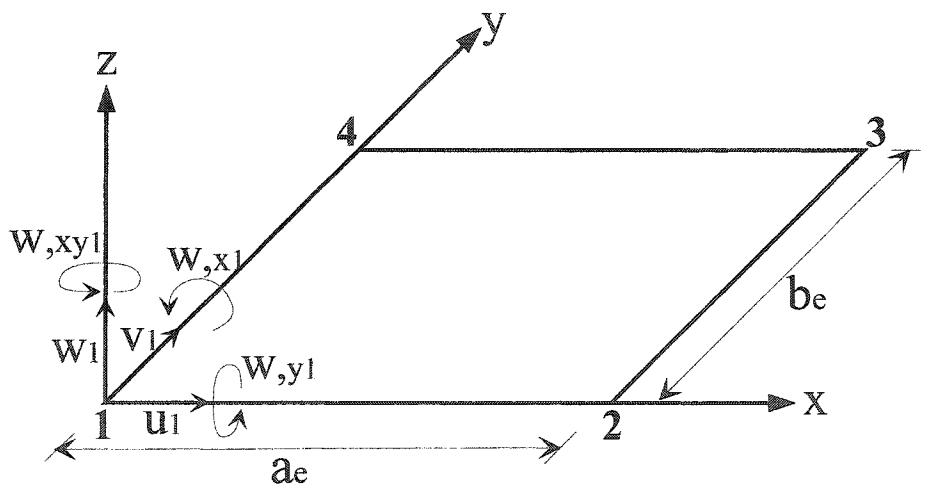

Fig. 3.7 Nodal degrees of freedom of a BFS C^1 conforming rectangular element

The element transverse displacement w and the in-plane displacements u and v can be approximated as a bi-cubic and a bilinear polynomial function of x, y, which can be expressed as:

$$\begin{aligned} w(x,y,z) &= a_1 + a_2x + a_3y + a_4x^2 + a_5xy + a_6y^2 + a_7x^3 + a_8x^2y + a_9xy^2 + a_{10}y^3 \\ &\quad + a_{11}x^3y + a_{12}x^2y^2 + a_{13}xy^3 + a_{14}x^3y^2 + a_{15}x^2y^3 + a_{16}x^3y^3 \\ &= [H_w(x,y)]\{a(t)\} \end{aligned} \tag{3.43}$$

where

$$[H_w(x,y)]=\{1 \;\; x \;\; y \;\; x^2 \;\; xy \;\; y^2 \;\; x^3 \;\; x^2y \;\; xy^2 \;\; y^3 \;\; x^3y \;\; x^2y^2 \;\; xy^3 \;\; x^3y^2 \;\; x^2y^3 \;\; x^3y^3\} \tag{3.44}$$

$$\{a\}=\{a_1 \;\; a_2 \;\; a_3 \;\; a_4 \;\; a_5 \;\; a_6 \;\; a_7 \;\; a_8 \;\; a_9 \;\; a_{10} \;\; a_{11} \;\; a_{12} \;\; a_{13} \;\; a_{14} \;\; a_{15} \;\; a_{16}\}^T \tag{3.45}$$

and

$$u(x,y,t) = b_1 + b_2x + b_3y + b_4xy = [H_u(x,y)]\{b(t)\} \tag{3.46}$$

where

$$[H_u(x,y)]=\{1 \;\; x \;\; y \;\; xy \;\; 0 \;\; 0 \;\; 0 \;\; 0\} \tag{3.47}$$

$$\{b\}=\{b_1 \;\; b_2 \;\; b_3 \;\; b_4 \;\; b_5 \;\; b_6 \;\; b_7 \;\; b_8\}^T \tag{3.48}$$

$$v(x,y,t) = b_5 + b_6x + b_7y + b_8xy = [H_v(x,y)]\{b(t)\} \tag{3.49}$$

where

$$[H_v(x,y)]=\{0 \;\; 0 \;\; 0 \;\; 0 \;\; 1 \;\; x \;\; y \;\; xy\} \tag{3.50}$$

The generalized coordinates {a} and {b} are related to the nodal DOF vectors by their respective transformation matrices as:

$$\begin{aligned} \{a\}&=[T_b]\{w_b\} \\ \{b\}&=[T_m]\{w_m\} \end{aligned} \tag{3.51}$$

The element displacement functions then can be expressed in terms of nodal displacement vectors as:

$$\begin{aligned} w &= [H_w(x,y)]\{a\}=[H_w(x,y)][T_b]\{w_b\} \\ u &= [H_u(x,y)]\{b\}=[H_u(x,y)][T_m]\{w_m\} \\ v &= [H_v(x,y)]\{b\}=[H_v(x,y)][T_m]\{w_m\} \end{aligned} \tag{3.52}$$

By using the finite element displacement functions, the in-plane strain vector components and the curvature vector components can be expressed in terms of the element nodal displacement vectors as follows:

$$\{\varepsilon_m^o\} = [C_m][T_m]\{w_m\} = [B_m]\{w_m\} \tag{3.53}$$

where

$$[C_m] = \begin{bmatrix} \dfrac{\partial}{\partial x}[H_u(x,y)] \\ \dfrac{\partial}{\partial y}[H_v(x,y)] \\ \dfrac{\partial}{\partial y}[H_u(x,y)] + \dfrac{\partial}{\partial x}[H_v(x,y)] \end{bmatrix} = \begin{bmatrix} 0 & 1 & 0 & y & 0 & 0 & 0 & 0 \\ 0 & 0 & 0 & 0 & 0 & 0 & 1 & x \\ 0 & 0 & 1 & x & 0 & 1 & 0 & y \end{bmatrix} \tag{3.54}$$

$$\{\varepsilon_\theta^o\} = \frac{1}{2}[\theta]\begin{Bmatrix} \dfrac{\partial w}{\partial x} \\ \dfrac{\partial w}{\partial y} \end{Bmatrix} = \frac{1}{2}[\theta][C_\theta][T_b]\{w_b\} = \frac{1}{2}[\theta][B_\theta]\{w_b\} \tag{3.55}$$

where

$$[\theta] = \begin{bmatrix} \dfrac{\partial w}{\partial x} & 0 \\ 0 & \dfrac{\partial w}{\partial y} \\ \dfrac{\partial w}{\partial y} & \dfrac{\partial w}{\partial x} \end{bmatrix} \tag{3.56}$$

$$[C_\theta] = \begin{Bmatrix} \dfrac{\partial}{\partial x}[H_w(x,y)] \\ \dfrac{\partial}{\partial y}[H_w(x,y)] \end{Bmatrix}$$

$$= \begin{bmatrix} 0 & 1 & 0 & 2x & y & 0 & 3x^2 & 2xy & y^2 & 0 & 3x^2y & 2xy^2 & y^3 & 3x^2y^2 & 2xy^3 & 3x^2y^3 \\ 0 & 0 & 1 & 0 & x & 2y & 0 & x^2 & 2xy & 3y^2 & x^3 & 2x^2y & 3xy^2 & 2x^3y & 3x^2y^2 & 3x^3y^2 \end{bmatrix} \tag{3.57}$$

$$\{\kappa\} = [C_b][T_b]\{w_b\} = [B_b]\{w_b\} \tag{3.58}$$

where

$$[C_b]=\begin{bmatrix} -\dfrac{\partial^2}{\partial x^2}[H_w(x,y)] \\ -\dfrac{\partial^2}{\partial y^2}[H_w(x,y)] \\ -2\dfrac{\partial^2}{\partial x\partial y}[H_w(x,y)] \end{bmatrix}$$

$$=-\begin{bmatrix} 0 & 0 & 0 & 2 & 0 & 0 & 6x & 2y & 0 & 0 & 6xy & 2y^2 & 0 & 6xy^2 & 2y^3 & 6xy^3 \\ 0 & 0 & 0 & 0 & 0 & 2 & 0 & 0 & 2x & 6y & 0 & 2x^2 & 6xy & 2x^3 & 6x^2y & 6x^3y \\ 0 & 0 & 0 & 0 & 2 & 0 & 0 & 4x & 4y & 0 & 6x^2 & 8xy & 6y^2 & 12x^2y & 12xy^2 & 18x^2y^2 \end{bmatrix} \quad (3.59)$$

Substituting Eqs. (3.53, 3.55 and 3.58) into Eq. (3.30), the resultant force vector {N} and moment vector {M} can be written as:

$$\{N\}=[A]\{\varepsilon^o\}+[B]\{\kappa\}+\{N_r\}-\{N_{\Delta T}\}=\{N_m\}+\{N_\theta\}+\{N_B\}+\{N_r\}-\{N_{\Delta T}\} \quad (3.60)$$

$$\{M\}=[B]\{\varepsilon^o\}+[D]\{\kappa\}+\{M_r\}-\{M_{\Delta T}\}=\{M_m\}+\{M_\theta\}+\{M_D\}+\{M_r\}-\{M_{\Delta T}\} \quad (3.61)$$

where

$$\{N_m\}=[A][B_m]\{w_m\} \quad (3.62)$$

$$\{N_\theta\}=\frac{1}{2}[A][\theta][B_\theta]\{w_b\} \quad (3.63)$$

$$\{N_B\}=[B][B_b]\{w_b\} \quad (3.64)$$

$$\{M_m\}=[B][B_m]\{w_m\} \quad (3.65)$$

$$\{M_\theta\}=\frac{1}{2}[B][\theta][B_\theta]\{w_b\} \quad (3.66)$$

$$\{M_D\}=[D][B_b]\{w_b\} \quad (3.67)$$

Substituting Eq. (3.52) into Eq. (3.35), noticing that w is the transverse displacement, the aerodynamic pressure can be expressed in finite element form as:

$$P_a=-\lambda\frac{D_{110}}{L^3}\left(\frac{\partial}{\partial x}[H_w]\cos\Lambda+\frac{\partial}{\partial y}[H_w]\sin\Lambda\right)[T_b]\{w_b\}-\frac{g_a}{\omega_o}\frac{D_{110}}{L^4}[H_w][T_b]\{\dot{w}_b\} \quad (3.68)$$

3.6.2 Element Equations of Motion

In this study, the governing equations are derived utilizing the principle of virtual work. This method states that the total work done by internal and external forces (including inertia forces) on an infinitesimal virtual displacement is zero:

$$\delta W = \delta W_{\text{int}} - \delta W_{ext} = 0 \tag{3.69}$$

The virtual work of the internal forces on a plate element is given by:

$$\delta W_{\text{int}} = \int_A \left(\left\{ \delta \varepsilon^o \right\}^T \{N\} + \{\delta \kappa\}^T \{M\} \right) dA \tag{3.70}$$

where A is the element area. The virtual in-plane strain and curvature vectors can be expressed as:

$$\left\{ \delta \varepsilon^o \right\} = \left\{ \delta \left(\varepsilon_m^o + \varepsilon_\theta^o \right) \right\} = \delta \left([B_m]\{w_m\} + \frac{1}{2}[\theta][B_\theta]\{w_b\} \right) \tag{3.71}$$

where

$$\delta([B_m]\{w_m\}) = [B_m]\{\delta w_m\} \tag{3.72}$$

$$\begin{aligned} \delta\left(\frac{1}{2}[\theta][B_\theta]\{w_b\} \right) &= \frac{1}{2}[\delta\theta][B_\theta]\{w_b\} + \frac{1}{2}[\theta][B_\theta]\{\delta w_b\} \\ &= \frac{1}{2}[\theta][B_\theta]\{\delta w_b\} + \frac{1}{2}[\theta][B_\theta]\{\delta w_b\} \\ &= [\theta][B_\theta]\{\delta w_b\} \end{aligned} \tag{3.73}$$

Therefore, Eq. (3.71) becomes:

$$\left\{ \delta \varepsilon^o \right\} = [B_m]\{\delta w_m\} + [\theta][B_\theta]\{\delta w_b\} \tag{3.74}$$

We also have:

$$\{\delta \kappa\} = \delta([B_b]\{w_b\}) = [B_b]\{\delta w_b\} \tag{3.75}$$

Substituting Eqs. (3.60, 3.61, 3.74 and 3.75) into Eq. (3.70), it yields:

$$\delta W_{\text{int}} = \int_A \left([B_m]\{\delta w_m\}+[\theta][B_\theta]\{\delta w_b\}\right)^T \cdot \left([A][B_m]\{w_m\}+\frac{1}{2}[A][\theta][B_\theta]\{w_b\}+[B][B_b]\{w_b\}+\{N_r\}-\{N_{\Delta T}\}\right) dA$$

$$+ \int_A \left([B_b]\{\delta w_b\}\right)^T \cdot \left([B][B_m]\{w_m\}+\frac{1}{2}[B][\theta][B_\theta]\{w_b\}+[D][B_b]\{w_b\}+\{M_r\}-\{M_{\Delta T}\}\right) dA$$

$$= \int_A \{\delta w_m\}^T [B_m]^T [A][B_m]\{w_m\} dA \quad (3.76\text{-}1)$$

$$+ \int_A \frac{1}{2}\{\delta w_m\}^T [B_m]^T [A][\theta][B_\theta]\{w_b\} dA \quad (3.76\text{-}2)$$

$$+ \int_A \{\delta w_m\}^T [B_m]^T [B][B_b]\{w_b\} dA \quad (3.76\text{-}3)$$

$$+ \int_A \{\delta w_m\}^T [B_m]^T \{N_r\} dA \quad (3.76\text{-}4)$$

$$- \int_A \{\delta w_m\}^T [B_m]^T \{N_{\Delta T}\} dA \quad (3.76\text{-}5)$$

$$+ \int_A \{\delta w_b\}^T [B_\theta]^T [\theta]^T [A][B_m]\{w_m\} dA \quad (3.76\text{-}6)$$

$$+ \int_A \frac{1}{2}\{\delta w_b\}^T [B_\theta]^T [\theta]^T [A][\theta][B_\theta]\{w_b\} dA \quad (3.76\text{-}7)$$

$$+ \int_A \{\delta w_b\}^T [B_\theta]^T [\theta]^T [B][B_b]\{w_b\} dA \quad (3.76\text{-}8)$$

$$+ \int_A \{\delta w_b\}^T [B_\theta]^T [\theta]^T \{N_r\} dA \quad (3.76\text{-}9)$$

$$- \int_A \{\delta w_b\}^T [B_\theta]^T [\theta]^T \{N_{\Delta T}\} dA \quad (3.76\text{-}10)$$

$$+ \int_A \{\delta w_b\}^T [B_b]^T [B][B_m]\{w_m\} dA \quad (3.76\text{-}11)$$

$$+ \int_A \frac{1}{2}\{\delta w_b\}^T [B_b]^T [B][\theta][B_\theta]\{w_b\} dA \quad (3.76\text{-}12)$$

$$+ \int_A \{\delta w_b\}^T [B_b]^T [D][B_b]\{w_b\} dA \quad (3.76\text{-}13)$$

$$+ \int_A \{\delta w_b\}^T [B_b]^T \{M_r\} dA \quad (3.76\text{-}14)$$

$$-\int_A \{\delta w_b\}^T [B_b]^T \{M_{\Delta T}\} dA \tag{3.76-15}$$

There are 15 terms, Eqs. (3.76-1) to (3.76-15), for the virtual work of internal forces. Equations. (3.76-1, -3, -11, -13) can be expressed as:

$$\begin{Bmatrix} \delta w_b \\ \delta w_m \end{Bmatrix}^T \begin{bmatrix} k_b & k_{bm} \\ k_{mb} & k_m \end{bmatrix} \begin{Bmatrix} w_b \\ w_m \end{Bmatrix} \tag{3.77}$$

where the linear stiffness matrices are:

$$[k_b] = \int_A [B_b]^T [D][B_b] dA \tag{3.78}$$

$$[k_{mb}] = [k_{bm}]^T = \int_A [B_m]^T [B][B_b] dA \tag{3.79}$$

$$[k_m] = \int_A [B_m]^T [A][B_m] dA \tag{3.80}$$

It is noticed that $[k_{mb}] = [k_{bm}]^T = 0$ for isotropic plates and symmetric laminate due to [B] = 0; and also

$$[\theta]^T \{N_{\Delta T}\} = \begin{bmatrix} \frac{\partial w}{\partial x} & 0 \\ 0 & \frac{\partial w}{\partial y} \\ \frac{\partial w}{\partial y} & \frac{\partial w}{\partial x} \end{bmatrix}^T \begin{Bmatrix} N_{\Delta Tx} \\ N_{\Delta Ty} \\ N_{\Delta Txy} \end{Bmatrix} = [N_{\Delta T}] \begin{Bmatrix} \frac{\partial w}{\partial x} \\ \frac{\partial w}{\partial y} \end{Bmatrix} = [N_{\Delta T}][B_\theta]\{w_b\} \tag{3.81}$$

where the thermal force matrix is written as:

$$[N_{\Delta T}] = \begin{bmatrix} N_{\Delta Tx} & N_{\Delta Txy} \\ N_{\Delta Txy} & N_{\Delta Ty} \end{bmatrix} \tag{3.82}$$

Substituting Eq. (3.81) into Eq. (3.76-10), we have:

$$-\begin{Bmatrix} \delta w_b \\ \delta w_m \end{Bmatrix}^T \begin{bmatrix} k_{\Delta Tb} & 0 \\ 0 & 0 \end{bmatrix} \begin{Bmatrix} w_b \\ w_m \end{Bmatrix} \tag{3.83}$$

where the thermal stiffness matrix is:

$$[k_{\Delta Tb}] = \int_A [B_\theta]^T [N_{\Delta T}][B_\theta] dA \tag{3.84}$$

Similarly, Eqs. (3.76-9) becomes:

$$\begin{Bmatrix} \delta w_b \\ \delta w_m \end{Bmatrix}^T \left(\begin{bmatrix} k_{rb} & 0 \\ 0 & 0 \end{bmatrix} \right) \begin{Bmatrix} w_b \\ w_m \end{Bmatrix} \tag{3.85}$$

where the stiffness matrix due to SMA fiber recovery stress σ_r is:

$$[k_{rb}] = \int_A [B_\theta]^T [N_r][B_\theta] dA \tag{3.86}$$

and the recovery force matrix is:

$$[N_r] = \begin{bmatrix} N_{rx} & N_{rxy} \\ N_{rxy} & N_{ry} \end{bmatrix} \tag{3.87}$$

Notice that:

$$[\theta]^T [A][B_m]\{w_m\} = [\theta]^T \{N_m\} = [N_m][B_\theta]\{w_b\} \tag{3.88}$$

where the force matrix due to in-plane displacement vector $\{w_m\}$ is:

$$[N_m] = \begin{bmatrix} N_{mx} & N_{mxy} \\ N_{mxy} & N_{my} \end{bmatrix} \tag{3.89}$$

Hence, Eqs. (3.76-2, -6) become:

$$\frac{1}{2} \begin{Bmatrix} \delta w_b \\ \delta w_m \end{Bmatrix}^T \begin{bmatrix} n_{1Nm} & n_{1bm} \\ n_{1mb} & 0 \end{bmatrix} \begin{Bmatrix} w_b \\ w_m \end{Bmatrix} \tag{3.90}$$

where the first-order nonlinear incremental stiffness matrices linearly dependent on $\{w\}$ are:

$$[n_{1Nm}] = \int_A [B_\theta]^T [N_m(\{w_m\})][B_\theta] dA \tag{3.91}$$

$$[n_{1mb}] = [n_{1bm}]^T = \int_A [B_m]^T [A][\theta(\{w_b\})][B_\theta] dA \tag{3.92}$$

Notice that:

$$[\theta]^T[B][B_b]\{w_b\}=[\theta]^T\{N_B\}=[N_B][B_\theta]\{w_b\} \tag{3.93}$$

where the force matrix due to transverse displacement vector $\{w_b\}$ is:

$$[N_B]=\begin{bmatrix} N_{Bx} & N_{Bxy} \\ N_{Bxy} & N_{By} \end{bmatrix} \tag{3.94}$$

Thus, Eqs. (3.76-8, -12) become:

$$\frac{1}{2}\begin{Bmatrix}\delta w_b \\ \delta w_m\end{Bmatrix}^T\begin{bmatrix} n_{1NB} & 0 \\ 0 & 0\end{bmatrix}\begin{Bmatrix} w_b \\ w_m\end{Bmatrix} \tag{3.95}$$

where the first-order nonlinear incremental stiffness matrix linearly dependent on $\{w_b\}$ is:

$$[n_{1NB}]=\int_A\left([B_\theta]^T[\theta(\{w_b\})]^T[B][B_b]+[B_\theta]^T[N_B(\{w_b\})][B_\theta]+[B_b]^T[B][\theta(\{w_b\})][B_\theta]\right)dA \tag{3.96}$$

Equation (3.76-7) can be written as:

$$\frac{1}{3}\begin{Bmatrix}\delta w_b \\ \delta w_m\end{Bmatrix}^T\begin{bmatrix} n_{2b} & 0 \\ 0 & 0\end{bmatrix}\begin{Bmatrix} w_b \\ w_m\end{Bmatrix} \tag{3.97}$$

where the second-order nonlinear incremental stiffness matrix quadratically dependent on $\{w_b\}$ is:

$$[n_{2b}]=\frac{3}{2}\int_A[B_\theta]^T[\theta(\{w_b\})]^T[A][\theta(\{w_b\})][B_\theta]dA \tag{3.98}$$

Equations (3.76-4, -14) can be expressed as:

$$\begin{Bmatrix}\delta w_b \\ \delta w_m\end{Bmatrix}^T\begin{Bmatrix} p_{rb} \\ p_{rm}\end{Bmatrix} \tag{3.99}$$

where the element bending and in-plane force vectors due to SMA recovery stress are:

$$\{p_{rb}\}=\int_A[B_b]^T\{M_r\}dA \tag{3.100}$$

$$\{p_{rm}\}=\int_A[B_m]^T\{N_r\}dA \tag{3.101}$$

Equations (3.76-5, -15) become:

$$-\begin{Bmatrix}\delta w_b\\ \delta w_m\end{Bmatrix}^T\begin{Bmatrix}p_{\Delta Tb}\\ p_{\Delta Tm}\end{Bmatrix} \tag{3.102}$$

where the element bending and in-plane force vectors due to thermal expansion are:

$$\{p_{\Delta Tb}\}=\int_A[B_b]^T\{M_{\Delta T}\}dA \tag{3.103}$$

$$\{p_{\Delta Tm}\}=\int_A[B_m]^T\{N_{\Delta T}\}dA \tag{3.104}$$

Hence, the virtual work of the internal forces on a plate element becomes:

$$\begin{aligned}\delta W_{\text{int}} =&\begin{Bmatrix}\delta w_b\\ \delta w_m\end{Bmatrix}^T\left(\begin{bmatrix}k_b & k_{bm}\\ k_{mb} & k_m\end{bmatrix}-\begin{bmatrix}k_{\Delta Tb} & 0\\ 0 & 0\end{bmatrix}+\begin{bmatrix}k_{rb} & 0\\ 0 & 0\end{bmatrix}\right.\\ &\left.+\frac{1}{2}\begin{bmatrix}n_{1Nm}+n_{1NB} & n_{1bm}\\ n_{1mb} & 0\end{bmatrix}+\frac{1}{3}\begin{bmatrix}n_{2b} & 0\\ 0 & 0\end{bmatrix}\right)\begin{Bmatrix}w_b\\ w_m\end{Bmatrix}\\ &+\begin{Bmatrix}\delta w_b\\ \delta w_m\end{Bmatrix}^T\left(\begin{Bmatrix}p_{rb}\\ p_{rm}\end{Bmatrix}-\begin{Bmatrix}p_{\Delta Tb}\\ p_{\Delta Tm}\end{Bmatrix}\right)\end{aligned} \tag{3.105}$$

The virtual work of the external forces on a plate element, considering inertia, aerodynamic and random pressure excitations, is:

$$\delta W_{ext} = \int_A[\delta w(-\rho h\ddot{w}+P_a+P(t))+\delta u(-\rho h\ddot{u})+\delta v(-\rho h\ddot{v})]dA \tag{3.106}$$

where P_a is the aerodynamic pressure, P(t) is the random excitation. By Eq. (3.52), the following expressions can be obtained:

$$\begin{aligned}\delta w &= [H_w][T_b]\{\delta w_b\}\\ \dot{w} &= [H_w][T_b]\{\dot{w}_b\}\\ \ddot{w} &= [H_w][T_b]\{\ddot{w}_b\}\\ \delta u &= [H_u][T_m]\{\delta w_m\}\\ \ddot{u} &= [H_u][T_m]\{\ddot{w}_m\}\end{aligned} \tag{3.107}$$

$$\delta v = [H_v][T_m]\{\delta w_m\}$$

$$\ddot{v} = [H_v][T_m]\{\ddot{w}_m\}$$

Substituting Eqs. (3.68 and 3.107) into Eq. (3.106), the finite element form of the virtual work of the external forces on an element becomes:

$$\begin{aligned}\delta W_{ext} = \int_A \Bigg[& \{\delta w_b\}^T [T_b]^T [H_w]^T \Bigg(-\rho h [H_w][T_b]\{\ddot{w}_b\} - \lambda \frac{D_{110}}{L^3}\left(\frac{\partial}{\partial x}[H_w]\cos\Lambda + \frac{\partial}{\partial y}[H_w]\sin\Lambda\right)[T_b]\{w_b\} \\ & - \frac{g_a}{\omega_o}\frac{D_{110}}{L^4}[H_w][T_b]\{\dot{w}_b\} + P(t)\Bigg) + \{\delta w_m\}^T [T_m]^T [H_u]^T \left(-\rho h [H_u][T_m]\{\ddot{w}_m\}\right) \\ & + \{\delta w_m\}^T [T_m]^T [H_v]^T \left(-\rho h [H_v][T_m]\{\ddot{w}_m\}\right) \Bigg] dA \qquad (2.108)\end{aligned}$$

$$= -\begin{Bmatrix}\delta w_b \\ \delta w_m\end{Bmatrix}^T \begin{bmatrix} m_b & 0 \\ 0 & m_m \end{bmatrix} \begin{Bmatrix}\ddot{w}_b \\ \ddot{w}_m\end{Bmatrix} - \begin{Bmatrix}\delta w_b \\ \delta w_m\end{Bmatrix}^T \begin{bmatrix} g & 0 \\ 0 & 0 \end{bmatrix} \begin{Bmatrix}\dot{w}_b \\ \dot{w}_m\end{Bmatrix}$$

$$- \lambda \begin{Bmatrix}\delta w_b \\ \delta w_m\end{Bmatrix}^T \begin{bmatrix} a_a(\Lambda) & 0 \\ 0 & 0 \end{bmatrix} \begin{Bmatrix} w_b \\ w_m\end{Bmatrix} + \begin{Bmatrix}\delta w_b \\ \delta w_m\end{Bmatrix}^T \begin{Bmatrix} p_t \\ 0\end{Bmatrix}$$

where mass matrices $[m_b]$ and $[m_m]$, aerodynamic damping matrix [g], aerodynamic stiffness matrix $[a_a]$, and random force vector $\{p_t\}$ are defined as:

$$[m_b] = \int_A \rho h [T_b]^T [H_w]^T [H_w][T_b] dA \qquad (3.109)$$

$$[m_m] = \int_A \rho h \left([T_m]^T [H_u]^T [H_u][T_m] + [T_m]^T [H_v]^T [H_v][T_m]\right) dA \qquad (3.110)$$

$$[a_a(\Lambda)] = \int_A \frac{D_{110}}{L^3}[T_b]^T [H_w]^T \left(\frac{\partial}{\partial x}[H_w]\cos\Lambda + \frac{\partial}{\partial y}[H_w]\sin\Lambda\right)[T_b] dA \qquad (3.111)$$

$$[g] = \int_A \frac{g_a}{\omega_o}\frac{D_{110}}{L^4}[T_b]^T [H_w]^T [H_w][T_b] dA \qquad (3.112)$$

$$\{p_t\} = \int_A [T_b]^T [H_w]^T P(t) dA \qquad (3.113)$$

Combining Eqs. (3.105, 3.108), the element equation of motion is expressed as:

$$\begin{bmatrix} m_b & 0 \\ 0 & m_m \end{bmatrix}\begin{Bmatrix} \ddot{w}_b \\ \ddot{w}_m \end{Bmatrix}+\begin{bmatrix} g(\lambda,C_a) & 0 \\ 0 & 0 \end{bmatrix}\begin{Bmatrix} \dot{w}_b \\ \dot{w}_m \end{Bmatrix}+\left(\lambda\begin{bmatrix} a_a(\Lambda) & 0 \\ 0 & 0 \end{bmatrix}+\begin{bmatrix} k_b & k_{bm} \\ k_{mb} & k_m \end{bmatrix}\right.$$

$$\left.-\begin{bmatrix} k_{\Delta Tb} & 0 \\ 0 & 0 \end{bmatrix}+\begin{bmatrix} k_{rb} & 0 \\ 0 & 0 \end{bmatrix}+\frac{1}{2}\begin{bmatrix} n_{1Nm}+n_{1NB} & n_{1bm} \\ n_{1mb} & 0 \end{bmatrix}+\frac{1}{3}\begin{bmatrix} n_{2b} & 0 \\ 0 & 0 \end{bmatrix}\right)\begin{Bmatrix} w_b \\ w_m \end{Bmatrix} \tag{3.114}$$

$$=\begin{Bmatrix} p_t \\ 0 \end{Bmatrix}+\begin{Bmatrix} p_{\Delta Tb} \\ p_{\Delta Tm} \end{Bmatrix}-\begin{Bmatrix} p_{rb} \\ p_{rm} \end{Bmatrix}$$

or simply

$$[m]\{\ddot{w}\}+[g]\{\dot{w}\}+\left(\lambda[a_a(\Lambda)]+[k]-[k_{N\Delta T}]+[k_r]+\frac{1}{2}[n_1]+\frac{1}{3}[n_2]\right)\{w\}$$

$$=\{p_t\}+\{p_{\Delta T}\}-\{p_r\} \tag{3.115}$$

where {w} is element nodal displacement vector; [m] and [g] are element mass and aerodynamic damping matrices, respectively; $[a_a]$, [k], $[k_{N\Delta T}]$, and $[k_r]$are element stiffness matrices: $[a_a]$ is due to aerodynamic loading, which is a function of flow yaw angle Λ; $[k_{N\Delta T}]$ is due to thermal stress generated by ΔT; $[k_r]$ is due to SMA fiber recovery stress σ_r. $[n_1]$ is element first-order nonlinear incremental stiffness matrix, which is linearly dependent on {w}; $[n_2]$ is element second-order nonlinear incremental stiffness matrix, which is quadratically dependent on $\{w_b\}$. The element force vectors $\{p_{\Delta T}\}$, $\{p_r\}$, $\{p_t\}$ are due to thermal stress generated by ΔT, $\{\sigma_r\}$ and random excitations, respectively.

3.6.3 System Equations of Motion and Physical Problems

Assembling the element equations of motion to system level by summing up the contributions from all elements and applying the boundary conditions, the system equations of motion become

$$\begin{bmatrix} M_b & 0 \\ 0 & M_m \end{bmatrix}\begin{Bmatrix} \ddot{W}_b \\ \ddot{W}_m \end{Bmatrix}+\begin{bmatrix} G(\lambda,C_a) & 0 \\ 0 & 0 \end{bmatrix}\begin{Bmatrix} \dot{W}_b \\ \dot{W}_m \end{Bmatrix}+\left(\lambda\begin{bmatrix} A_a(\Lambda) & 0 \\ 0 & 0 \end{bmatrix}+\begin{bmatrix} K_b & K_{bm} \\ K_{mb} & K_m \end{bmatrix}\right.$$

$$\left.-\begin{bmatrix} K_{\Delta Tb} & 0 \\ 0 & 0 \end{bmatrix}+\begin{bmatrix} K_{rb} & 0 \\ 0 & 0 \end{bmatrix}+\frac{1}{2}\begin{bmatrix} N_{1Nm}+N_{1NB} & N_{1bm} \\ N_{1mb} & 0 \end{bmatrix}+\frac{1}{3}\begin{bmatrix} N_{2b} & 0 \\ 0 & 0 \end{bmatrix}\right)\begin{Bmatrix} W_b \\ W_m \end{Bmatrix} \tag{3.116}$$

$$=\begin{Bmatrix} P_t(t) \\ 0 \end{Bmatrix}+\begin{Bmatrix} P_{\Delta Tb} \\ P_{\Delta Tm} \end{Bmatrix}-\begin{Bmatrix} P_{rb} \\ P_{rm} \end{Bmatrix}$$

or simply

$$[M]\{\ddot{W}\}+[G(\lambda,C_a)]\{\dot{W}\}+\left(\lambda[A_a(\Lambda)]+[K]-[K_{N\Delta T}]+[K_r]+\frac{1}{2}[N_1(\{W\})]+\frac{1}{3}[N_2(\{W\},\{W\})]\right)\{W\}$$

$$=\{P_t(t)\}+\{P_{\Delta T}\}-\{P_r\} \tag{3.117}$$

Equation (3.117) is a set of nonlinear differential equations describing the panel motion under the combined thermal, aerodynamic and random loads. Generally speaking, the physical problems associated with the system equations of motion can be categorized into two types: static and dynamic problems. For static problems, inertial term and damping term are dropped as well as random excitation $\{P_t(t)\}$. Therefore, for static thermal buckling problem, Eq. (3.117) becomes:

$$\left([K]-[K_{N\Delta T}]+[K_r]+\frac{1}{2}[N_1(\{W\})]+\frac{1}{3}[N_2(\{W\},\{W\})]\right)\{W\}=\{P_{\Delta T}\}-\{P_r\} \tag{3.118}$$

For static aerothermal buckling problem, accordingly, Eq. (3.117) becomes:

$$\left(\lambda[A_a(\Lambda)]+[K]-[K_{N\Delta T}]+[K_r]+\frac{1}{2}[N_1(\{W\})]+\frac{1}{3}[N_2(\{W\},\{W\})]\right)\{W\}=\{P_{\Delta T}\}-\{P_r\} \tag{3.119}$$

By considering various combinations of applied loads in several groups, the dynamic problem can be further divided into: (i) panel flutter problem with the thermal effect, (ii)

random vibration problem with thermal effect, and (iii) random-flutter vibration problem under combined three loads: thermal, aerodynamic and random loads.

Among the dynamic problems, panel flutter problem with thermal effect is well investigated in the literature.[25] Equation (3.117) becomes:

$$[M]\{\ddot{W}\}+[G(\lambda,C_a)]\{\dot{W}\}+\left(\lambda[A_a(\Lambda)]+[K]-[K_{N\Delta T}]+[K_r]+\frac{1}{2}[N_1(\{W\})]+\frac{1}{3}[N_2(\{W\},\{W\})]\right)\{W\}$$

$$=\{P_{\Delta T}\}-\{P_r\} \tag{3.120}$$

The plate could have four different behaviors: flat and stable (static), buckled but dynamically stable, LCO flutter and chaotic motion.

Random vibration problem with thermal effect is also investigated a great deal in the literature. Equation (3.117) becomes:

$$[M]\{\ddot{W}\}+[C]\{\dot{W}\}+\left([K]-[K_{N\Delta T}]+[K_r]+\frac{1}{2}[N_1(\{W\})]+\frac{1}{3}[N_2(\{W\},\{W\})]\right)\{W\}$$

$$=\{P_t(t)\}+\{P_{\Delta T}\}-\{P_r\} \tag{3.121}$$

Random response characteristics can be displayed by time history, phase plane, power spectrum density (PSD), and probability distribution function (PDF). The plate could demonstrate three types of random vibrations: (i) small random vibration about one of the two thermal BEPs, (ii) snap-through between the two BEPs (intermittent snap-through), and (iii) large random vibration over the two BEPs (persistent snap-through). However, investigation of plate response under all of the three loads simultaneously has seldom been found in the literature.

3.6.4 Condensed System Equations of Motion

Equation (3.116) can be condensed through separating $\{W_b\}$ and $\{W_m\}$. Rewrite Eq. (3.116) in the full expression in a simplified format as:

$$\begin{bmatrix} M_b & 0 \\ 0 & M_m \end{bmatrix}\begin{Bmatrix} \ddot{W}_b \\ \ddot{W}_m \end{Bmatrix}+\begin{bmatrix} G & 0 \\ 0 & 0 \end{bmatrix}\begin{Bmatrix} \dot{W}_b \\ \dot{W}_m \end{Bmatrix}+\left(\lambda\begin{bmatrix} A_a & 0 \\ 0 & 0 \end{bmatrix}+\begin{bmatrix} K_b & K_{bm} \\ K_{mb} & K_m \end{bmatrix}-\begin{bmatrix} K_{\Delta Tb} & 0 \\ 0 & 0 \end{bmatrix}+\begin{bmatrix} K_{rb} & 0 \\ 0 & 0 \end{bmatrix}\right.$$

$$\left.+\begin{bmatrix} K_{1Nm}+K_{1NB} & K_{1bm} \\ K_{1mb} & 0 \end{bmatrix}+\begin{bmatrix} K_{2b} & 0 \\ 0 & 0 \end{bmatrix}\right)\begin{Bmatrix} W_b \\ W_m \end{Bmatrix}=\begin{Bmatrix} P_b \\ P_m \end{Bmatrix} \tag{3.122}$$

where

$$\begin{bmatrix} K_{1Nm}+K_{1NB} & K_{1bm} \\ K_{1mb} & 0 \end{bmatrix}=\frac{1}{2}\begin{bmatrix} N_{1Nm}+N_{1NB} & N_{1bm} \\ N_{1mb} & 0 \end{bmatrix} \tag{3.123}$$

$$\begin{bmatrix} K_{2b} & 0 \\ 0 & 0 \end{bmatrix}=\frac{1}{3}\begin{bmatrix} N_{2b} & 0 \\ 0 & 0 \end{bmatrix} \tag{3.124}$$

$$\{P_b\}=\{P_t\}+\{P_{\Delta Tb}\}-\{P_{rb}\} \tag{3.125}$$

$$\{P_m\}=\{P_{\Delta Tm}\}-\{P_{rm}\} \tag{3.126}$$

First, separate Eq. (3.122) into two equations as:

$$[M_b]\{\ddot{W}_b\}+[G]\{\dot{W}_b\}+(\lambda[A_a]+[K_b]-[K_{\Delta Tb}]+[K_{rb}]+[K_{1Nm}]+[K_{1NB}]+[K_{2b}])\{W_b\}$$
$$+([K_{bm}]+[K_{1bm}])\{W_m\}=\{P_b\} \tag{3.127}$$

$$[M_m]\{\ddot{W}_m\}+([K_{mb}]+[K_{1mb}])\{W_b\}+[K_m]\{W_m\}=\{P_m\} \tag{3.128}$$

For a thin plate, neglecting the in-plane inertia term $[M_m]\{\ddot{W}_m\}$ will not bring significant error, because in-plane natural frequencies usually are 2 to 3 order higher than bending ones. Therefore, the in-plane displacement vector $\{W_m\}$ can be expressed in terms of bending displacement vector $\{W_b\}$ as:

$$\{W_m\} = [K_m]^{-1}[\{P_m\} - ([K_{mb}] + [K_{1mb}])\{W_b\}]$$
$$= [K_m]^{-1}\{P_m\} - [K_m]^{-1}[K_{mb}]\{W_b\} - [K_m]^{-1}[K1_{mb}]\{W_b\} = \{W_m\}_0 - \{W_m\}_1 - \{W_m\}_2 \quad (3.129)$$

where $\{W_m\}_0$ is a constant, $\{W_m\}_1$ is linearly dependent on $\{W_b\}$, and $\{W_m\}_2$ is quadratically dependent on $\{W_b\}$. Thus, the matrix $[K_{1Nm}(\{W_m\})]$ is evaluated by algebraic sum of three components: $[K_{1Nm}(\{W_m\}_0)]$, $[K_{1Nm}(\{W_m\}_1)]$ and $[K1_{Nm}(\{W_m\}_2)]$, which are independent, linearly dependent and quadratically dependent on $\{W_b\}$, respectively.

According to Eq. (3.88),

$$[K_{1bm}]\{W_m\} = [K_{1Nm}]\{W_b\} \quad (3.130)$$

similarly,

$$[K_{1bm}]\{W_m\}_0 = [K_{1Nm}(\{W_m\}_0)]\{W_b\} \quad (3.131)$$

Substituting Eq. (3.131) into Eq. (3.127) and reorganizing it, the transformed system equation in functions of $\{W_b\}$ only can be expressed as:

$$[M_b]\{\ddot{W}_b\} + [G]\{\dot{W}_b\} + ([K_{lin}] + [K_1] + [K_2])\{W_b\} = \{P_c\} \quad (3.132)$$

where the combined linear stiffness matrix $[K_{lin}]$ is:

$$[K_{lin}] = \lambda[A_a] + [K_b] - [K_{\Delta Tb}] + [K_{rb}] - [K_{bm}][K_m]^{-1}[K_{mb}] + 2[K_{1Nm}(\{W_m\}_0)] \quad (3.133)$$

the combined nonlinear stiffness matrices $[K_1]$ and $[K_2]$ are:

$$[K_1] = [K_{1NB}] - [K_{1Nm}(\{W_m\}_1)] - [K_{1bm}][K_m]^{-1}[K_{mb}] - [K_{bm}][K_m]^{-1}[K_{1mb}] \quad (3.134)$$

$$[K_2] = [K_{2b}] - [K_{1bm}][K_m]^{-1}[K_{1mb}] - [K_{1Nm}(\{W_m\}_2)] \quad (3.135)$$

The matrices $[K_1]$ and $[K_2]$ are linearly and quadratically dependent on bending displacement vector $\{W_b\}$, respectively; and the combined force vector $\{P_c\}$ is

$$\{P_c\} = \{P_b\} - [K_{bm}][K_m]^{-1}\{P_m\} \tag{3.136}$$

CHAPTER IV SOLUTION PROCEDURES

4.1 Introduction

For any approach adopted for solving thermal buckling and postbuckling, nonlinear panel flutter and random response problems of SMAHC plates, the nonlinear temperature-dependent material properties of SMA and/or composite matrix must be considered. In this chapter, detailed solution procedures are presented for solving all the physical problems described in Chapter II. Basically, for the static thermal buckling or aerothermal buckling problems, the system equations could be solved directly by Newton-Raphson method in structural node DOF; for dynamic panel flutter or random vibration under the influence of thermal load, the system equations of motion are first transferred into modal equations using either normal or aeroelastic modes, followed by time domain numerical method.

4.2 Static Aerothermal Buckling in Structural Node DOF

For thermal buckling and postbuckling problem under the influence of aerodynamic flow, the panel static response is the so-called aerothermal buckling. The inertia, damping and the random load $\{P_t\}$ are thus removed for this problem. Therefore, Eq. (3.119) becomes

$$\left(\lambda\begin{bmatrix}A_a(\Lambda) & 0\\ 0 & 0\end{bmatrix}+\begin{bmatrix}K_b & K_{bm}\\ K_{mb} & K_m\end{bmatrix}-\begin{bmatrix}K_{\Delta Tb} & 0\\ 0 & 0\end{bmatrix}+\begin{bmatrix}K_{rb} & 0\\ 0 & 0\end{bmatrix}\right.$$

$$\left.+\frac{1}{2}\begin{bmatrix}N_{1Nm}+N_{1NB} & N_{1bm}\\ N_{1mb} & 0\end{bmatrix}+\frac{1}{3}\begin{bmatrix}N_{2b} & 0\\ 0 & 0\end{bmatrix}\right)\begin{Bmatrix}W_b\\ W_m\end{Bmatrix}=\begin{Bmatrix}P_{\Delta Tb}\\ P_{\Delta Tm}\end{Bmatrix}-\begin{Bmatrix}P_{rb}\\ P_{rm}\end{Bmatrix} \tag{4.1}$$

Newton-Raphson method is employed to determine the aerothermal deflections for the whole temperature range investigated. The advantages are that, first it is a general-purposed method in the sense that it is applicable to all cases, e.g. symmetrical or asymmetrical lamination, uniform temperature or temperature gradient across the plate thickness, and single or multiple critical temperatures (which is possible when SMA is activated well above the reference temperature[87]); and second it yields aerothermal postbuckling deflection solutions. It is observed that thermal buckling and postbuckling is a special case of aerothermal buckling with $\lambda = 0$ in Eq. (4.1).

In order for Newton-Raphson iteration method to be capable of solving nonlinear algebraic equation, Eq. (4.1) is expressed as Taylor expansion:

$$\Phi(W+\Delta W)=\Phi(W)+\frac{d\Phi}{dW}\{\Delta W\}+O(\Delta W)^2=0 \tag{4.2}$$

where

$$\Phi(W)=\left(\lambda[A_a]+[K]-[K_{N\Delta T}]+[K_r]+\frac{1}{2}[N_1]+\frac{1}{3}[N_2]\right)\{W\}-\{P_{\Delta T}\}+\{P_r\} \tag{4.3}$$

$$\frac{d\Phi(W)}{dW}=\frac{d}{dW}\left[\left(\lambda[A_a]+[K]-[K_{N\Delta T}]+[K_r]+\frac{1}{2}[N_1]+\frac{1}{3}[N_2]\right)\{W\}\right]-\frac{d}{dW}[\{P_{\Delta T}\}-\{P_r\}] \tag{4.4}$$

The slope $\frac{d\Phi(W)}{dW}$ needs to be evaluated for a given initial guess {W}. Analyzing Eq. (4.4), the system aerodynamic stiffness matrix and linear stiffness matrices are independent of {W}, and thus it yields

$$\frac{d}{dW}[(\lambda[A_a]+[K]-[K_{N\Delta T}]+[K_r])\{W\}]=\lambda[A_a]+[K]-[K_{N\Delta T}]+[K_r] \tag{4.5}$$

The nonlinear stiffness matrices $[N_1]$ and $[N_2]$ are linearly and quadratically dependent on $\{W\}$, respectively, and the derivatives are:

$$\frac{d}{dW}\left[\left(\frac{1}{2}[N_1]+\frac{1}{3}[N_2]\right)\{W\}\right]=\frac{d}{dW}\left(\frac{1}{2}[N_1]+\frac{1}{3}[N_2]\right)\{W\}+\left(\frac{1}{2}[N_1]+\frac{1}{3}[N_2]\right) \tag{4.6}$$

The first term in above equation can be further broken down as:

$$d\left(\frac{1}{2}[N_1]+\frac{1}{3}[N_2]\right)\{W\}=d\begin{bmatrix}\frac{1}{2}[N_{1Nm}]+\frac{1}{2}[N_{1NB}]+\frac{1}{3}[N_{2b}] & \frac{1}{2}[N_{1bm}]\\ \frac{1}{2}[N_{1mb}] & 0\end{bmatrix}\begin{Bmatrix}W_b\\W_m\end{Bmatrix} \tag{4.7}$$

$$=\begin{bmatrix}\frac{1}{2}d[N_{1Nm}]\{W_b\}+\frac{1}{2}d[N_{1NB}]\{W_b\}+\frac{1}{3}d[N_{2b}]\{W_b\}+\frac{1}{2}d[N_{1bm}]\{W_m\}\\ \frac{1}{2}d[N_{1mb}]\{W_b\}\end{bmatrix}$$

The terms in the above equation can be deduced from their corresponding element matrices as:

$$d[n_{1Nm}]\{w_b\}=\int_A[B_\theta]^T d[N_m][B_\theta]dA\{w_b\}=\int_A[B_\theta]^T d[\theta]^T[A][B_m]dA\{w_m\} \tag{4.8}$$

$$=\int_A[B_\theta]^T[\theta]^T[A][B_m]dA\{dw_m\}=[n_{1bm}]\{dw_m\}$$

$$d[n_{1bm}]\{w_m\}=\int_A[B_\theta]^T d[\theta]^T[A][B_m]dA\{w_m\}=\int_A[B_\theta]^T[N_m][B_\theta]dA\{dw_b\} \tag{4.9}$$

$$=[n_{1Nm}]\{dw_b\}$$

$$d[n_{1mb}]\{w_b\}=\int_A[B_m]^T[A]d[\theta][B_\theta]dA\{w_b\}=\int_A[B_m]^T[A][\theta][B_\theta]dA\{dw_b\} \tag{4.10}$$

$$=[n_{1mb}]\{dw_b\}$$

$$d[n_{1NB}]\{w_b\} = \int_A \left([B_\theta]^T [A] d[\theta][B_\theta] + [B_\theta]^T d[\theta]^T [A] [B_\theta] + [B_\theta]^T d[N_\theta][B_\theta] \right) dA\{w_b\}$$

$$= \int_A \left([B_\theta]^T [A][\theta][B_\theta] + [B_\theta]^T [\theta]^T [A] [B_\theta] + [B_\theta]^T [N_\theta][B_\theta] \right) dA\{dw_b\} \tag{4.11}$$

$$= [n_{1NB}]\{dw_b\}$$

$$d[n_{2b}]\{w_b\} = \frac{3}{2} \int_A [B_\theta]^T d\left([\theta]^T [A][\theta] \right) [B_\theta] dA\{w_b\} = 2 \cdot \frac{3}{2} \int_A [B_\theta]^T [\theta]^T [A] d[\theta][B_\theta] dA\{w_b\}$$

(4.12)

$$= 2 \cdot \frac{3}{2} \int_A [B_\theta]^T [\theta]^T [A][\theta][B_\theta] dA\{dw_b\} = 2[n_{2b}]\{dw_b\}$$

The terms $d[\theta][\cdots]\{w_b\} = [\theta][\cdots]\{dw_b\}$ and $d\left([\theta]^T [A][\theta]\right) = 2[\theta]^T [A] d[\theta]$ in Eqs. (4.10) – (4.12) can be derived from their definitions using simple matrix manipulations. Assembling the above terms in Eqs. (4.8) – (4.12) into their system level, the following relation holds:

$$\frac{d}{dW}\left(\frac{1}{2}[N_1] + \frac{1}{3}[N_2] \right)\{W\} = \frac{1}{2}[N_1] + \frac{2}{3}[N_2] \tag{4.13}$$

Substituting Eq. (4.13) into Eq. (4.6), the latter becomes

$$\frac{d}{dW}\left[\left(\frac{1}{2}[N_1] + \frac{1}{3}[N_2] \right)\{W\} \right] = [N_1] + [N_2] \tag{4.14}$$

Since force vector $\{P_{\Delta T}\}$ and $\{P_r\}$ are independent on $\{W\}$, then

$$\frac{d}{dW}[\{P_{\Delta T}\} - \{P_r\}] = 0 \tag{4.15}$$

Combining Eqs. (4.5), (4.14), and (4.15), $\frac{d\Phi(W)}{dW}$ can be expressed as:

$$\frac{d\Phi(W)}{dW} = [K_{\tan}] = \lambda[A_a] + [K] - [K_{N\Delta T}] + [K_r] + [N_1] + [N_2] \tag{4.16}$$

The object is to find {W} such that $\Phi(W) = 0$. At a given ΔT, for the i^{th} iteration, Newton-Raphson iteration method can be written in the incremental form:

$$[K_{\tan}]_i \{\Delta W\}_{i+1} = \{\Delta P\}_i \tag{4.18}$$

where the tangent stiffness matrix $[K_{tan}]_i$ is

$$[K_{\tan}]_i = \lambda[A_a] + [K] - [K_{N\Delta T}] + [K_r] + [N_1]_i + [N_2]_i \tag{4.19}$$

and $\{\Delta P\}_i$ is the imbalanced force vector, which is expressed as:

$$\{\Delta P\}_i = \{P_{\Delta T}\} - \{P_r\} - \left(\lambda[A_a] + [K] - [K_{N\Delta T}] + [K_r] + \frac{1}{2}[N_1]_i + \frac{1}{3}[N_2]_i\right)\{W\}_i \tag{4.20}$$

The subscript i denotes that the nonlinear stiffness matrices are evaluated with the displacement of i^{th} iteration $\{W\}_i$. The increment displacement vector $\{\Delta W\}_{i+1}$ can be calculated from Eq. (4.18), then {W} is updated as:

$$\{W\}_{i+1} = \{W\}_i + \{\Delta W\}_{i+1} \tag{4.21}$$

The solution procedure seeks to reduce the imbalanced force vector $\{\Delta P\}$ and consequently $\{\Delta W\}$ to a specified small quantity: $\max|\{\Delta W\}|/h < 10^{-3}$ in this study.

To start the procedure, an initial non-zero trial of {W} is needed. In this paper, it is given as:

$$\{W\} = 0.1h\lfloor 1 \quad 1 \quad \ldots \quad 1 \rfloor^T \tag{4.22}$$

where h is the plate thickness. For the additional temperatures, the initial trial employed is the {W} from the previous temperature.

With the participation of aerodynamic load, the stability of Eq. (4.18) using Newton-Raphson method could be a problem. This is due to the skew-symmetric matrix $[A_a]$, which contributes to the instability of the system. Numerically, it is found that the

iterative solution will lose convergence when the plate goes near the chaotic region. It may be explained as: in a chaotic region, no equilibrium exists.

Once the static BEP {W} is obtained for a certain ΔT, the linear vibration frequency of the plate about this BEP {W} can be determined. By adding the inertia terms, the linear equation of vibration about a BEP {W} is:

$$[M]\{\ddot{W}\}_t + [K_{\tan}]\{W\}_t = 0 \tag{4.23}$$

where $\{W\}_t$ is the dynamic response of transverse displacement and $[K_{tan}]$ is just the tangent matrix determined in the last iteration using Eq. (4.19).[40]

Equation (4.23) can be solved as a standard linear eigenvalue problem to determine the vibration frequencies and mode shapes of a thermally loaded plate about the BEP. The characteristics obtained here can be used in selection of random excitation frequency range f_u in Eqs. (3.39) and (3.41) for numerical simulation.

4.3 Dynamic Response Using Modal Equations in Normal Modes

Rewrite the condensed system equations of motion, Eqs. (3.128) – (3.132), as

$$[M_b]\{\ddot{W}_b\} + [G]\{\dot{W}_b\} + ([K_{lin}] + [K_1] + [K_2])\{W_b\} = \{P_c\} \tag{4.24}$$

where

$$[K_{lin}] = \lambda[A_a] + [K_b] - [K_{\Delta Tb}] + [K_{rb}] - [K_{bm}][K_m]^{-1}[K_{mb}] + 2[K_{1Nm}(\{W_m\}_0)] \tag{4.25}$$

$$[K_1] = [K_{1NB}] - [K_{1Nm}(\{W_m\}_1)] - [K_{1bm}][K_m]^{-1}[K_{mb}] - [K_{bm}][K_m]^{-1}[K_{1mb}] \tag{4.26}$$

$$[K_2] = [K_{2b}] - [K_{1bm}][K_m]^{-1}[K_{1mb}] - [K_{1Nm}(\{W_m\}_2)] \tag{4.27}$$

$$\{P_c\} = \{P_b\} - [K_{bm}][K_m]^{-1}\{P_m\} \tag{4.28}$$

where $\{P_b\}$ is defined in Eq. (3.125). For a given set of T, λ, Λ and C_a (or $g_a = \sqrt{\lambda C_a}$), Eq. (4.24) can be solved by numerical integration in the structural node DOF. This approach turns out to be computationally costly because:

(1) At each time step, the element nonlinear stiffness matrices have to be evaluated and the system nonlinear stiffness matrices have to be assembled and updated,

(2) The number of structure bending DOF $\{W_b\}$ is usually very large, and

(3) The time step of the integration should be extremely small in order to make the solution accurate and stable.

An alternative and effective solution procedure is to transform Eq. (4.24) into the modal coordinates using reduced system normal modes (described in this section) or aeroelastic modes (next section 3.4). By expressing the system bending displacement $\{W_b\}$ as a linear combination of some known base functions (mode shapes) as:

$$\{W_b\} \approx \sum_{r=1}^{n} q_r \{\phi_r\} = [\Phi]\{q\} \tag{4.29}$$

where the rth normal mode (NM) $\{\phi_r\}$ and the corresponding linear frequency ω_r are obtained from the linear vibration of the system:

$$\omega_r^2 [M_b]\{\phi_r\} = \left([K_b] - [K_{bm}][K_m]^{-1}[K_{mb}]\right)\{\phi_r\} \tag{4.30}$$

Based on NMs, it is necessary to transform all the matrices in Eq. (4.24) into the modal coordinates. Those element nonlinear stiffness matrices are evaluated with the corresponding element components $\{w_b\}$, which in turn is obtained from the known system linear mode $\{\phi_r\}$.

The nonlinear stiffness matrices, which are directly related to $\{W_b\}$, can be expressed as the summation of the products of NM amplitudes q_r (r =1 to n) and nonlinear modal stiffness matrices as:

$$([K_{1NB}],[K_{1bm}],[K_{1mb}]) = \sum_{r=1}^{n} q_r \left([K_{1NB}]^{(r)},[K_{1bm}]^{(r)},[K_{1mb}]^{(r)}\right) \tag{4.31}$$

$$[K_{2b}] = \sum_{r=1}^{n}\sum_{s=1}^{n} q_r q_s \left([K_{2b}]^{(rs)}\right) \tag{4.32}$$

where the super indices of those nonlinear modal stiffness matrices denote that they are assembled from the corresponding element nonlinear stiffness matrices.

The in-plane displacement $\{W_m\}$, Eq. (3.129), is expressed as

$$\begin{aligned}
\{W_m\} &= [K_m]^{-1}\{P_m\} - [K_m]^{-1}[K_{mb}]\{W_b\} - [K_m]^{-1}[K1_{mb}]\{W_b\} \\
&= \{W_m\}_0 - [K_m]^{-1}[K_{mb}]\sum_{r=1}^{n} q_r\{\phi_r\} - [K_m]^{-1}\left(\sum_{r=1}^{n} q_r [K_{1mb}]^{(r)}\right)[\Phi]\{q\} \\
&= \{W_m\}_0 - \sum_{r=1}^{n} q_r\{\phi_r\}_m - \sum_{r=1}^{n}\sum_{s=1}^{n} q_r q_s \{\phi_{rs}\}_m \\
&= \{W_m\}_0 - \{W_m\}_1 - \{W_m\}_2
\end{aligned} \tag{4.33}$$

where the in-plane modes corresponding to the bending modes $\{\phi_r\}$ and $\{\phi_s\}$ are

$$\{\phi_r\}_m = [K]_m^{-1}[K_{mb}]\{\phi_r\} \tag{4.34}$$

$$\{\phi_{rs}\}_m = [K]_m^{-1}[K_{1mb}]^{(r)}\{\phi_s\} \tag{4.35}$$

Therefore, $[K_{1Nm}(\{W_m\}_1)]$ and $[K_{1Nm}(\{W_m\}_2)]$ can be expressed as:

$$[K_{1Nm}(\{W_m\}_1)] = \sum_{r=1}^{n} q_r [K_{1Nm}(\{\phi_r\}_m)] = \sum_{r=1}^{n} q_r [K_{1Nm}]^{(r)} \tag{4.36}$$

$$[K_{1Nm}(\{W_m\}_2)] = \sum_{r=1}^{n}\sum_{s=1}^{n} q_r q_s [K_{1Nm}(\{\phi_{rs}\}_m)] = \sum_{r=1}^{n}\sum_{s=1}^{n} q_r q_s [K_{2Nm}]^{(rs)} \tag{4.37}$$

and the first constant $\{W_m\}_0$ term in Eq. (4.33) has been considered in $\{K_{lin}]$ matrix in Eq. (4.25). The system dynamic equation is then transformed into the modal coordinates as:

$$[\overline{M}_b]\{\ddot{q}\} + [\overline{G}]\{\dot{q}\} + 2[\zeta_r \omega_r][\overline{M}_b]\{\dot{q}\} + ([\overline{K}] + [\overline{K}_q] + [\overline{K}_{qq}])\{q\} = \{\overline{P}_c\} \tag{4.38}$$

where the modal mass, modal aerodynamic damping and modal linear stiffness matrices $[\overline{M}_b],[\overline{G}],[\overline{K}]$ are given by:

$$([\overline{M}_b],[\overline{G}],[\overline{K}]) = [\Phi]^T([M_b],[G],[K_{lin}])[\Phi] \tag{4.39}$$

The first-order and second-order nonlinear modal stiffness matrices $[\overline{K}_q]$and $[\overline{K}_{qq}]$are:

$$[\overline{K}_q] = [\Phi]^T \sum_{r=1}^{n} q_r \left([K_{1NB}]^{(r)} - [K_{1Nm}]^{(r)} - [K_{1bm}]^{(r)}[K_m]^{-1}[K_{mb}] - [K_{bm}][K_m]^{-1}[K_{1mb}]^{(r)}\right)[\Phi] \tag{4.40}$$

$$[\overline{K}_{qq}] = [\Phi]^T \sum_{r=1}^{n}\sum_{s=1}^{n} q_r q_s \left([K_{2b}]^{(rs)} - [K_{2Nm}]^{(rs)} - [K_{1bm}]^{(r)}[K_m]^{-1}[K_{1mb}]^{(s)}\right)[\Phi] \tag{4.41}$$

The modal force vector $\{\overline{P}_c\}$ is given by:

$$\{\overline{P}_c\} = [\Phi]^T\{P_c\} \tag{4.42}$$

A modal structural damping matrix $2[\zeta_r \omega_r][\overline{M}_b]$ has been added to Eq. (4.38) to account for the structural damping effect on the system. The coefficient ζ_r is modal

damping ratio for the r^{th} mode. It can be determined experimentally, and ω_r is the r^{th} modal natural frequency.

With the given combined thermal, aerodynamic, and acoustic loadings, all the matrices and coefficients in Eq. (4.38) are defined and can be obtained utilizing the previously derived equations. Given the initial values of modal coordinates $\{q\}$and $\{\dot{q}\}$, Eq. (4.38) can be solved numerically for {q}, and the system nodal displacements $\{W_b\}$ and $\{W_m\}$ can then be obtained using Eqs. (4.29) and (4.33), respectively.

A small number of most contributing modes to the total response can be determined from their modal participation (MP) values, and it is defined as:

$$Participation\ of\ r^{th}\ \text{mode} = \begin{cases} \dfrac{RMS(q_r)}{\sum_{s=1}^{n} RMS(q_s)} & if\ random\ involved \\ \dfrac{\max|q_r|}{\sum_{s=1}^{n} \max|q_s|} & otherwise \end{cases} \tag{4.43}$$

where RMS stands for root-mean-square value. Those modes with significant participation values can be identified and they should be retained in the analysis.

The benefits of using the time domain numerical integration method to solve the system dynamic equations of Eq. (4.38) are:

(1) Compared with methods in structural node DOF, the computational cost is reduced dramatically;

(2) For panel flutter analysis under thermal load, compared with frequency domain method, all four types of panel behaviors can be determined: static flat and stable, buckled but dynamically stable, LCO and periodic/chaotic motion;

(3) For nonlinear random vibration problem, it does not need to assume that the random response distribution is Gaussian as using the equivalent linearization method, and the snap-through phenomenon can be determined; and

(4) It is by now the only efficient method to study the panel behavior under the combined thermal, aerodynamic and acoustic loadings.

4.4 Dynamic Response Using Modal Equations in Aeroelastic Modes

Traditionally, there are two distinct analysis methods in supersonic nonlinear panel flutter: the time domain and the frequency domain. In time domain approach, the coupled nonlinear modal (in NMs) equations are formulated from the governing partial differential equations (PDE's) in conjunction with Galerkin's method in the spatial domain,[27-29,30,31,33,43-45] or from the finite element modal formulation.[46,47] LCO responses are then determined from the nonlinear modal equations using techniques including numerical integration, harmonic balance, or perturbation method in the time domain. In frequency domain approaches, the coupled nonlinear equations of motion are formulated using finite element methods and expressed in the structural node DOF[40] or normal modal coordinates.[42] The panel responses are determined by an iterative linearized eigen-solution using the linearized updated mode with a nonlinear time function (LUM/NTF) approximation method.[40,50] It is found that six in-vacuo NMs (1,1) to (6,1) are needed for accurate analysis for a simply supported isotropic square plate at zero flow yaw angle.[27]

In the frequency domain analysis using the six in-vacuo NMs (1,1) to (6,1), shown in Fig. 4.1, for a simply supported isotropic square plate at $\Lambda = 0°$. It is noticed that the six

NMs are located on the vertical axis at $\lambda = 0$. The linear ($W_{max}/h = 0.0$) eigenvalues for modes (1,1) and (2,1) coalesce at the critical dynamic pressure $\lambda_{cr} = 512$. Using the LUM/NTF method, the converged iterative linearized eigenvalues κ versus λ for two typical large amplitudes at $W_{max}/h = 0.6$ and 1.2 are shown, and they coalesce at the flutter dynamic pressures λ_{f1} and λ_{f2}, respectively. The variation of LCO amplitude W_{max}/h versus dynamic pressure is thus determined and shown in Fig. 4.2. The LCO deflections at $W_{max}/h = 0.6$ and 1.2 are shown in Fig. 4.3.

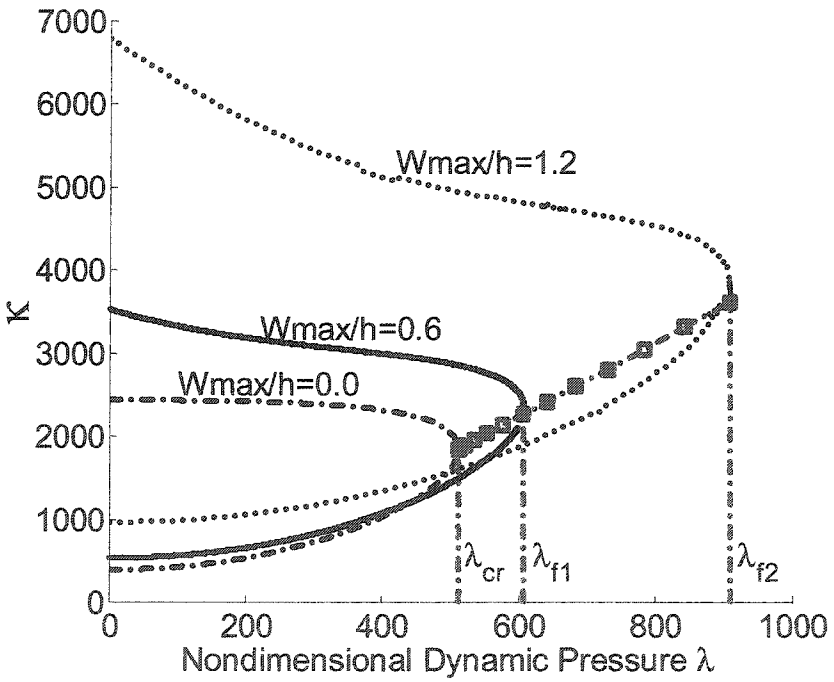

Fig. 4.1 Eigenvalues κ versus dynamic pressure for a simply supported isotropic square plate at $\Lambda = 0°$.

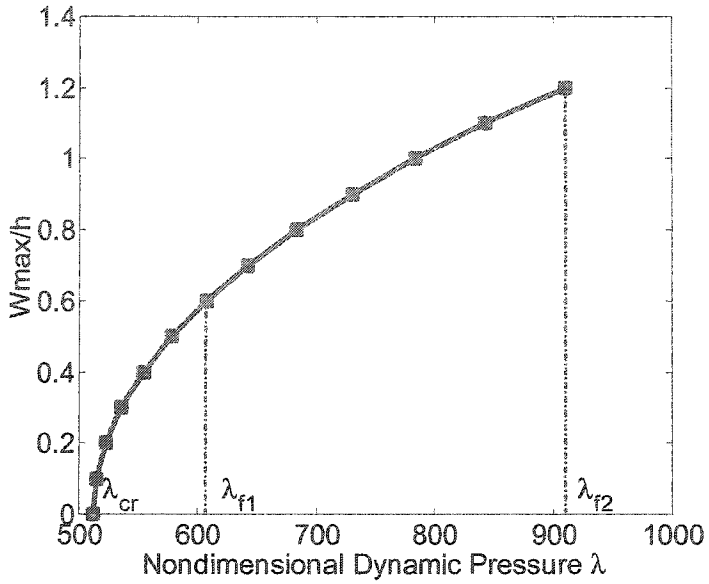

Fig. 4.2 LCO amplitudes versus dynamic pressure for a simply supported isotropic square plate at $\Lambda = 0°$.

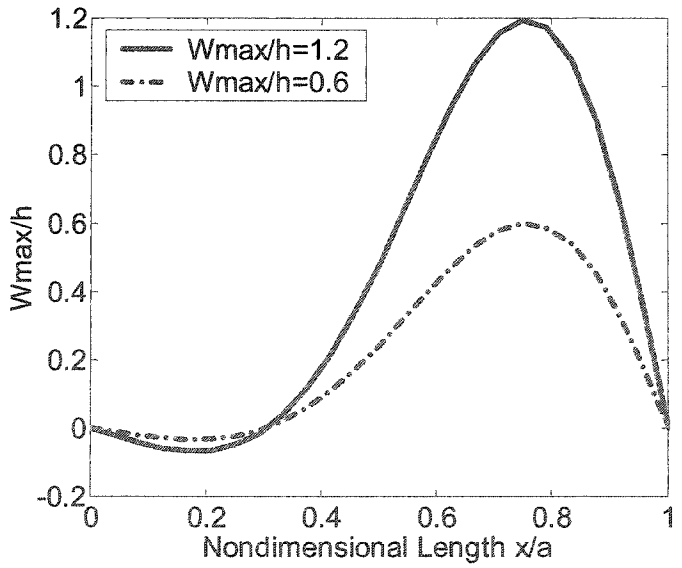

Fig. 4.3 LCO deflections of $W_{max}/h = 0.6$ and 1.2 at $y = b/2$ for a simply supported isotropic square plate at $\Lambda = 0°$.

Re-examining of Fig. 4.1, the LCO occurs at $\lambda > \lambda_{cr}$; while the six base NMs are located far away at $\lambda = 0$. Why does one not consider using the linear aeroelastic modes

(AEMs) that reside near the LCO in the κ-λ plot of Fig. 4.1. The AEMs[48] are the linear panel vibration modes under the influence of dynamic pressure $0 < \lambda < \lambda_{cr}$. A plot of the lowest two normalized AEMs at $\lambda = 510$ is shown in Fig. 4.4. By comparing the LCO deflection shapes in Fig. 4.3 and the AEMs in Fig. 4.4, it is now much certain that the use of AEMs will reduce the number of DOF for the limit-cycle analysis since the LCO deflections and the AEMs have great similarities in shape.

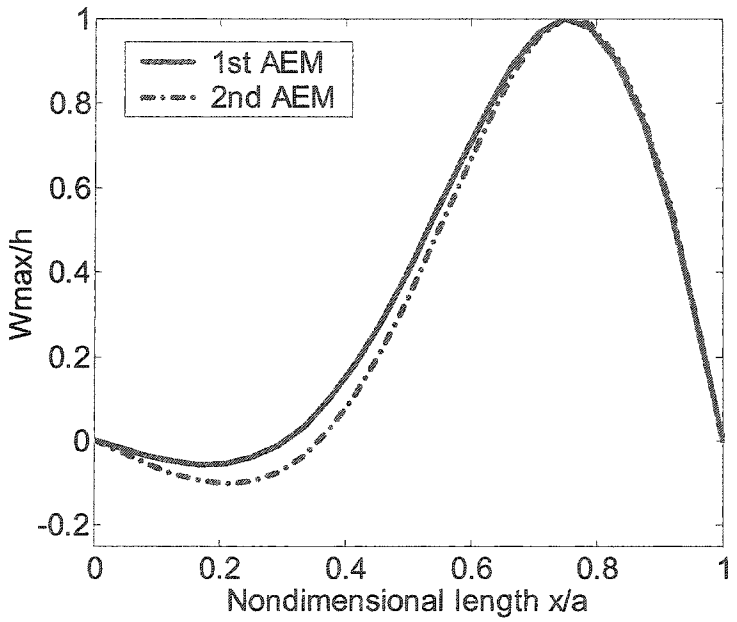

Fig. 4.4 Normalized AEMs at $\lambda_o = 510$ for a simply supported isotropic square plate at $\Lambda = 0°$.

The system bending displacement vector $\{W_b\}$ can now be expressed as a linear combination of some known base functions (modal transformation) as:

$$\{W_b\} \approx \sum_{r=1}^{n} q_r \{\phi_r\} = [\Phi]\{q\} \tag{4.44}$$

where the number of retained linear aeroelastic modes, n, is much smaller than the number of structural node DOF in bending $\{W_b\}$ as well as the number of NMs. The rth

AEM $\{\phi_r\}$ is a right eigenvector[90] and normalized with the maximum component to unity as shown in Fig. 4.4. The matrix of selected AEMs $[\Phi]$, which is the matrix of right eigenvectors, and the corresponding linear frequencies ω_r are obtained from the linear vibration of the system with the influence of aerodynamic influence matrix term

$$\omega_r^2[M_b]\{\phi_r\} = \left(\lambda_o[A_a]+[K_b]-[K_{bm}][K_m]^{-1}[K_{mb}]\right)\{\phi_r\} \tag{4.45}$$

where λ_o is a certain selected dynamic pressure value. The aerodynamic matrix $[A_a]$ is skew-symmetric and thus the combined matrix $\left(\lambda_o[A_a]+[K_b]-[K_{bm}][K_m]^{-1}[K_{mb}]\right)$ is asymmetrical. Hence, the desirable properties of the eigenvalues and eigenvectors associated with symmetric matrices no longer exist. In particular, for $\lambda_o < \lambda_{cr}$, the eigenvalues and eigenvectors are real, but the eigenvectors are no longer orthogonal. Here we utilize the concept of right and left eigenvectors[90] in order to transform the system equations into modal coordinates.

The system dynamic equation, Eq. (4.24), is transformed into the reduced AEM coordinates by using the similar manipulations as:

$$\left[\overline{M}_b\right]\{\ddot{q}\}+\left[\overline{G}\right]\{\dot{q}\}+2\left[\zeta_r\omega_r\right]\left[\overline{M}_b\right]\{\dot{q}\}+\left(\left[\overline{K}\right]+\left[\overline{K}_q\right]+\left[\overline{K}_{qq}\right]\right)\{q\}=\{\overline{P}_c\} \tag{4.46}$$

where the modal mass matrix, modal aerodynamic damping matrix and modal linear stiffness matrix are given by:

$$([\overline{M}_b],[\overline{G}],[\overline{K}]) = [\Phi_L]^T([M_b],[G],[K_{lin}])[\Phi] \tag{4.47}$$

The first-order and second-order nonlinear modal stiffness matrices $\left[\overline{K}_q\right]$ and $\left[\overline{K}_{qq}\right]$ are:

$$\left[\overline{K}_q\right]=[\Phi_L]^T\sum_{r=1}^{n}q_r\left([K_{1NB}]^{(r)}-[K_{1Nm}]^{(r)}-[K_{1bm}]^{(r)}[K_m]^{-1}[K_{mb}]-[K_{bm}][K_m]^{-1}[K_{1mb}]^{(r)}\right)[\Phi] \tag{4.48}$$

$$\left[\overline{K}_{qq}\right]=\left[\Phi_L\right]^T\sum_{r=1}^{n}\sum_{s=1}^{n}q_r q_s\left(\left[K_{2b}\right]^{(rs)}-\left[K_{2Nm}\right]^{(rs)}-\left[K_{1bm}\right]^{(r)}\left[K_m\right]^{-1}\left[K_{1mb}\right]^{(s)}\right)\left[\Phi\right] \quad (4.49)$$

The modal force vectors $\left\{\overline{P}_c\right\}$ is given by:

$$\left\{\overline{P}_c\right\}=\left[\Phi_L\right]^T\left\{P_c\right\} \quad (4.50)$$

where $[\Phi_L]$ is the matrix of left eigenvectors corresponding to the selected AEMs, which are the selected right eigenvectors. Because the original whole square matrix of left eigenvectors $[\Phi'_L]$ is related with the original whole square matrix of right eigenvectors $[\Phi']$ by $[\Phi'_L]^T = [\Phi']^{-1}$, $[\Phi_L]$ is obtained by extracting the corresponding parts from the $[\Phi']^{-1}$.[90]

Equation (4.46) is identical with Eq. (4.38) in format, while the difference lies on the modes they used and how the modal mass and stiffness matrices are evaluated. It will be demonstrated that with AEMs, the number of modes used can be greatly reduced compared with using NMs. AEMs can be used whenever there exists dynamic pressure, such as flutter with thermal load and flutter-random response under three combined loadings.

4.5 Strain Calculation

After the system nodal displacement vectors $\{W_b\}$ and $\{W_m\}$ are obtained in each time step, the strain vector for each element can be calculated from:

$$\{\varepsilon\}=\left\{\varepsilon_m^o\right\}+\left\{\varepsilon_\theta^o\right\}+z\{\kappa\}=\left[B_m\right]\{w_m\}+\left(\frac{1}{2}\left[\theta\right]\left[B_\theta\right]+z\left[B_b\right]\right)\{w_b\} \quad (4.51)$$

For a displacement-based finite element method, one expects the strain to be less accurate than the displacement. However, at Barlow points[91,92] inside the element, the accuracy of

the strain is equal to that of the displacement, or even higher. For the BFS C^1 rectangular element, the stiffness matrix is approximated by the area integration of a 6^{th}-order polynomial, so that 4^{th}-order Gauss quadrature can be used to exactly compute the area integration numerically. Barlow points are actually one order less Gauss points. Therefore, for BFS C^1 rectangular element, 3^{rd}-order Gauss points are adopted as Barlow points. In this study, the strain values at Barlow points are calculated from Eq. (4.51), the results are then extrapolated to the element node points. The strain values at a certain global node point are averaged from different element node values, which share the same global node number.

CHAPTER V STATIC THERMAL AND AEROTHERMAL RESPONSE

Examples are presented for an isotropic plate, a traditional composite plate, and three configurations of SMAHC plates. The numerical results and discussions include five sections: i) static thermal buckling and postbuckling due to thermal load only (Chapter V), ii) static aerothermal buckling and postbuckling due to combined aerodynamic and thermal loads (Chapter V), iii) panel flutter due to combined aerodynamic and thermal loads (Chapter VI), iv) random vibration due to combined acoustic and thermal loads (Chapter VII), and v) dynamic response due to combined aerodynamic, acoustic and thermal loads (Chapter VIII).

The static or dynamic response is investigated and displayed in various domains: i) the temperature-dynamic pressure (ΔT-λ) region for combined thermal and aerodynamic loads, ii) the temperature-acoustic sound pressure level (ΔT-SPL) domain due to combined thermal and acoustic loads, and iii) the temperature-dynamic pressure-sound pressure level (ΔT-λ-SPL) domain. The results determined for the SMAHC plates are compared with those for the isotropic and traditional composite plates.

For the purpose of comparison, the rectangular traditional composite plate and the SMAHC plates studied here have the identical dimensions, laminations and matrices. The plate dimension is 15×12×0.05 in. (38.1×30.5×0.13 cm), the lamination is eight layered with a stacking sequence $[0/-45/45/90]_s$, and the composition is Graphite-Epoxy.

Nitinol is chosen as the SMA fibers in the SMAHC plates. The Nitinol fibers are embedded in all eight layers and are along the same direction as the graphite fibers due to manufacture restrictions. The Young's modulus versus temperature, and recovery stresses versus temperature of Nitinol are testing data from Cross et al.[4] The phase transformation is activated at the room temperature 70°F (reference temperature). The other properties of Nitinol are given in Table 5.1. The material properties of graphite-epoxy are also considered as temperature dependent as shown in Table 5.1. The aluminum and titanium plates with the same configuration are included for comparisons.

Table 5.1 Material properties of Nitinol, graphite-epoxy composite lamina and titanium

Nitinol	Graphite-epoxy	Titanium
See Figs.1 and 2 for Young's modulus and recovery stresses	E_1 22.5×10^6 (1-3.53×10^{-4}·ΔT) psi (155 (1-6.35×10^{-4}·ΔT) GPa)	E 14.94×10^6 psi (103 GPa)
G 3.604×10^6 psi, $T<A_s$ (24.9 GPa)	E_2 1.17×10^6 (1-4.27×10^{-4}·ΔT) psi (8.07 (1-7.69×10^{-4}·ΔT) GPa)	ρ 0.424×10^{-3} lb-s^2/in.^{4} (4510 Kg/m^3)
3.712×10^6 psi, $T\geq A_s$ (25.6 GPa)	G_{12} 0.66×10^6 (1-6.06×10^{-4}·ΔT) psi (4.55 (1-1.09×10^{-3}·ΔT) GPa)	μ 0.37
ρ 0.6067×10^{-3} lb-s^2/in.^{4} (6450 Kg/m^3)	ρ 0.1458×10^{-3} lb-s^2/in.^{4} (1550 Kg/m^3)	α 4.78×10^{-6}/°F (8.6×10^{-6}/°C)
μ 0.3	μ_{12} 0.22	
α 5.7×10^{-6}/°F (10.26×10^{-6}/°C)	α_1 -0.04×10^{-6}(1-1.25×10^{-3}·ΔT)/°F (-0.07×10^{-6}(1-0.69×10^{-3}·ΔT) /°C)	
	α_2 16.7×10^{-6}(1+0.41×10^{-4}·ΔT)/°F (40.6×10^{-6}(1+0.28×10^{-4}·ΔT) /°C)	

5.1 Static Thermal Buckling and Postbuckling Response

In this section, the effects of SMA recovery stress on the reduction of static thermal deflection of SMAHC plates are studied. Rewrite Eq. (3.118) for static thermal buckling of a plate,

$$\left([K]-[K_{N\Delta T}]+[K_r]+\frac{1}{2}[N_1(\{W\})]+\frac{1}{3}[N_2(\{W\},\{W\})]\right)\{W\}=\{P_{\Delta T}\}-\{P_r\} \tag{5.1}$$

The thermal load is assumed to be uniformly distributed without temperature gradient across the thickness of the plate. Thermal deflection and the lowest natural frequency versus temperature are investigated.

The full plate is modeled with a 12×12 mesh or 144 BFS rectangular elements. All the four edges are all simply supported or all clamped. The in-plane support conditions are immovable as u(0,y) = u(a,y) = v(x,0) = v(x,b) = 0.

The Newton-Raphson iterative method is employed to determine the thermal deflections from the governing equations expressed in structural node DOF. Figure 5.1 shows the maximum thermal deflections for both simply supported and clamped composite plates. To simplify the comparisons between the traditional composite plate and the SMAHC plates, unless otherwise specified, only clamped cases are studied and presented.

The non-dimensional maximum thermal deflection versus temperature for the SMAHC plates with three configurations in volume fraction and prestrain of SMA: (v_s = 10% and ε_r = 3%), (v_s = 10% and ε_r = 5%) and (v_s = 15% and ε_r = 3%) are shown in Fig. 5.2. The temperature range investigated is ΔT = 0°F - 430°F (T = 70°F - 500°F) or ΔT =

0°C - 239°C . The thermal deflection for the traditional composite plate is also drawn in Fig. 5.2 for comparison. The critical temperatures for the titanium, traditional composite and SMAHC plates are shown in Table 5.2. It is seen that the higher the values of volume fraction and prestrain are, the higher the critical temperature is. The results clearly indicate that the large recovery stress introduced by the SMA results in a more stiffened plate for a wide range of temperature and thus a higher critical buckling temperature.

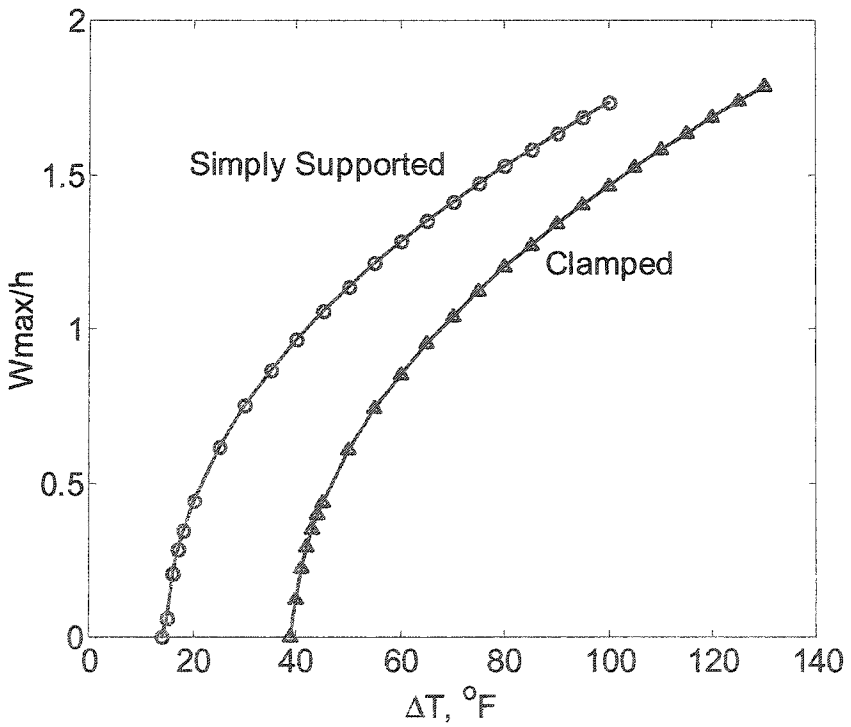

Fig. 5.1 The maximum thermal buckling deflection for traditional composite plates.

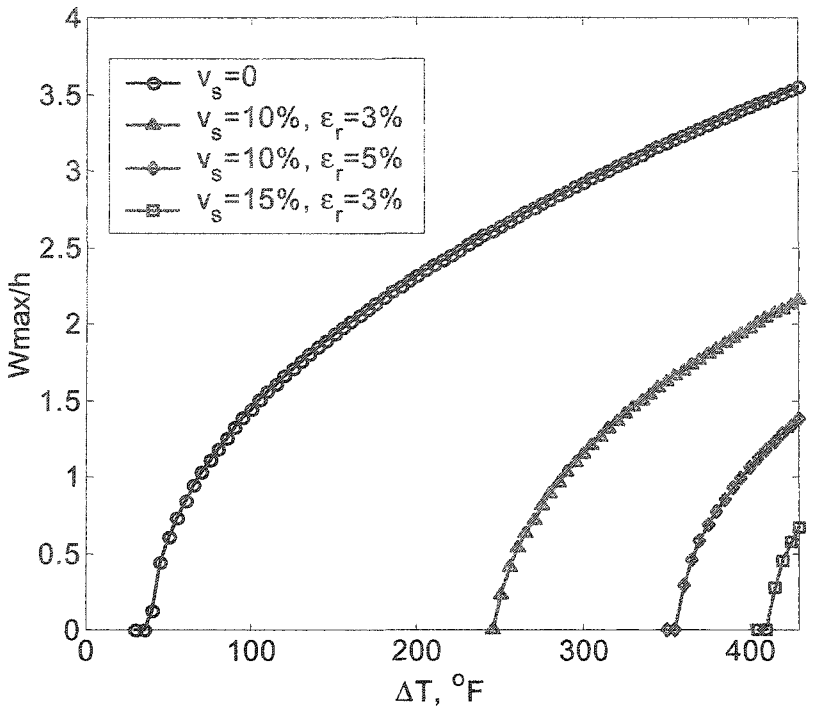

Fig. 5.2 The maximum thermal buckling deflection of a clamped traditional composite plate ($v_s = 0$) and the clamped SMAHC plates ($v_s \neq 0$).

Table 5.2 Critical buckling temperatures of the clamped titanium, traditional composite and SMAHC plates

	v_s	ε_r	ΔT_{cr} (°F)
Titanium	-	-	79.8
Graphite-Epoxy	-	-	39.3
SMAHC	10%	3%	245
	10%	5%	355
	15%	3%	410

The natural frequencies and mode shapes of linear vibration about the buckled equilibrium position (BEP) or the flat but pre-stressed (before buckling) plate can be determined by the eigenvalue problem described in Eq. (4.23). The fundamental natural frequency versus temperature for the SMAHC plates with three configurations of volume

fraction v_s and prestrain ε_r are shown in Fig. 5.3. It is seen from the figure that the fundamental frequencies go to zero at T_{cr} for all the plates. For the traditional composite plate, the frequency decreases all the way from T_{ref} through ΔT_{cr} purely due to the thermal expansion effect. At ΔT_{cr}, the plate loses the static stability and the bifurcation deflection happens. The frequency increases after passing ΔT_{cr} because of the geometrical nonlinearity of the buckled plate. For two of the three configurations of SMAHC plates, except (v_s = 10% and ε_r = 5%), the frequency first increases, then decreases before reach ΔT_{cr}. This is due to the counteraction between the SMA recovery stress and the thermal expansion effect. When the temperature is in the relatively low region, the SMA recovery tensile stress increases faster than the compressive stress due to the thermal expansion, and results in a more stiffened plate. After the recovery stresses increase slower at the moderate temperature region, the thermal expansion gradually becomes dominant, the plate becomes softer and the natural frequency begins to decrease. For the SMAHC (v_s = 10% and ε_r = 5%) plate, the recovery stress just increases not as fast as that due to the thermal expansion at the very beginning.

The mass density of graphite-epoxy is 1550 kg/m^3. Nitinol and titanium are much heavier. The savings in weight based on critical temperatures are presented in Fig. 5.4. For titanium and traditional composites plates, the thickness of the plates is varied through a multiple of the base thickness h = 0.05 in. It is shown that to achieve a given ΔT_{cr}, for example 350°F (T_{cr} = 420°F), the weight of a clamped SMAHC (v_s = 10% and ε_r = 5%) plate is about 0.53 lb (0.24 kg), while the weight is 1.2 lb (0.54 kg) for a traditional composite plate of thickness 3h (0.15 in.). It is obviously that the weight of

titanium plate is the heaviest and other means such as adding stiffeners and frames should be done for titanium plate to reach such a critical temperature value.

5.2 Static Aerothermal Buckling Deflections

Under the combined thermal and aerodynamic loads, if the airflow speed is low, the flutter will not occur. The plate may keep flat and stable, or becomes thermally buckled but dynamically stable under the influence of airflow. Rewrite the equation governing static aerothermal buckling of a plate, or Eq. (3.119)

$$\left(\lambda[A_a(\Lambda)]+[K]-[K_{N\Delta T}]+[K_r]+\frac{1}{2}[N_1(\{W\})]+\frac{1}{3}[N_2(\{W\},\{W\})]\right)\{W\}=\{P_{\Delta T}\}-\{P_r\} \qquad (5.2)$$

Notice that the airflow influence matrix $\lambda[A_a(\Lambda)]$ is added to the stiffness terms. Since aerothermal buckling is still a static problem, Newton-Raphson iterative method is used here. The full plate is modeled with a 12×12 mesh or 144 BFS rectangular elements, which is accurate enough. All the four edges are clamped. The in-plane support conditions are immovable as aforementioned.

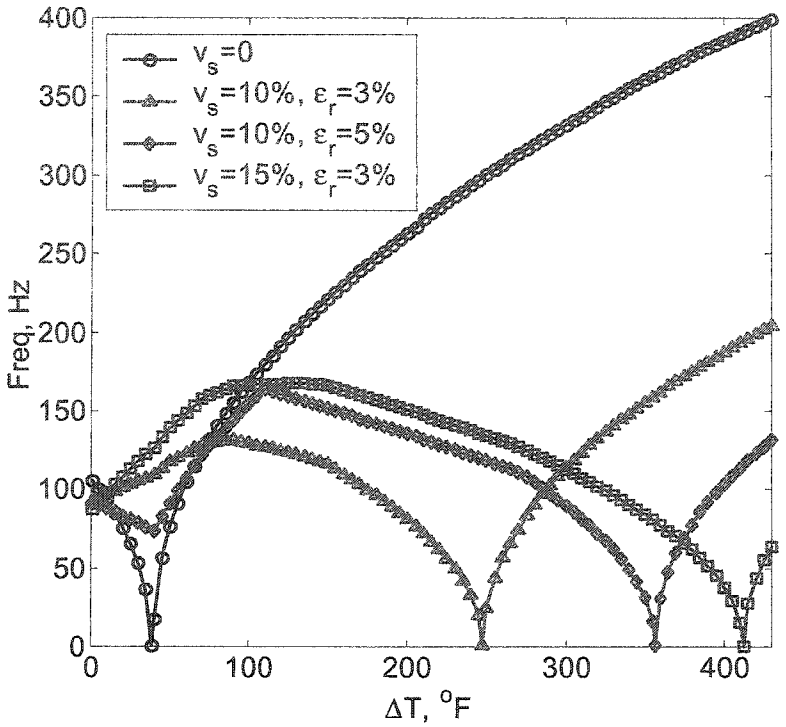

Fig. 5.3 Fundamental natural frequency of a clamped traditional composite plate and clamped SMAHC plates.

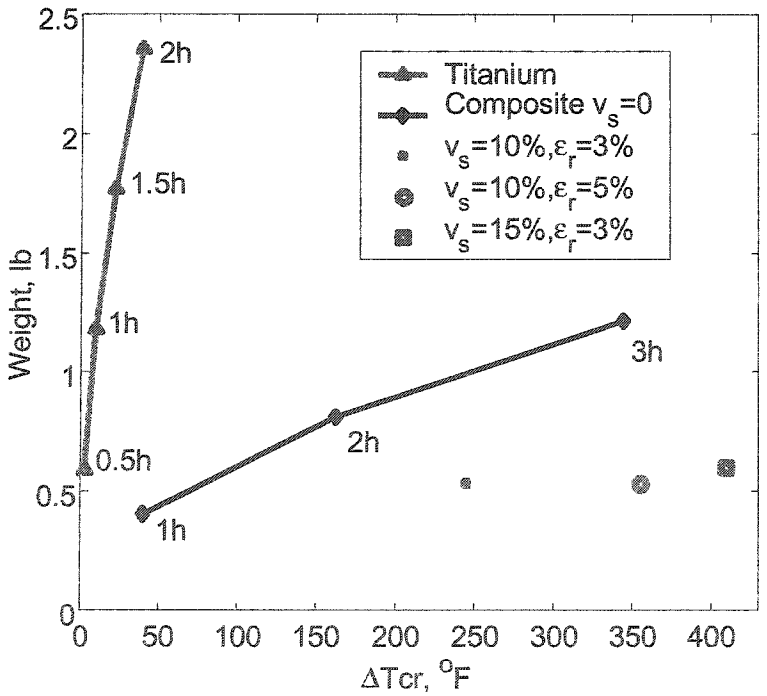

Fig. 5.4 Weights versus the critical temperatures for the clamped titanium, traditional composite and SMAHC plates.

The presence of airflow makes the panel stiffened so that the aerothermal deflection decreases as airflow dynamic pressure λ increases. This is demonstrated in Fig. 5.5, where the square of the deflections is plotted versus temperature[40,44] for the clamped traditional composite plate at $\Lambda = 0°$ and $\lambda = 0$, 90, 150, 160 and 170, respectively. It is found the convergence can't be achieved once λ is beyond 170, which indicates that a statically unstable region is reached. Figure 5.6 shows the shape of the aerothermal deflection at $\lambda = 120$, $\Lambda = 0°$ and $\Delta T = 150°F$. It is seen that the front part of the plate is "blow" to a dent with the maximum deflection position moving to the back part. Moreover, the dent is also not symmetrical about y-axis. This can be explained as: the $[0/-45/45/90]_s$ composite plate is much softer and tends to deform easily in the direction of $\theta = 45°$ than the direction of $\theta = -45°$.

At a flow angle $\Lambda = 45°$, as shown in Fig. 5.7, the statically unstable region is reached much earlier than at $\Lambda = 0°$, and λ can not be beyond 90 for a stable converged solution, which verified once more that the composite plate is much softer in the direction of $\theta = 45°$. This shows that the flow yaw angle $\Lambda = 45°$ results in a smaller aerothermal buckling region.

In this iterative procedure, the convergence often fails if the flow dynamic pressure is close enough or already getting into flutter or chaotic regions, which become a dynamic problem. Since the difficulty for the Newton-Raphson iteration method of obtaining a converged buckling deflection prevents a full investigation over the temperature-dynamic pressure (ΔT-λ) domain, the comparison between the SMAHC

plates and the traditional composite plate is described in the following section using numerical integration in time domain.

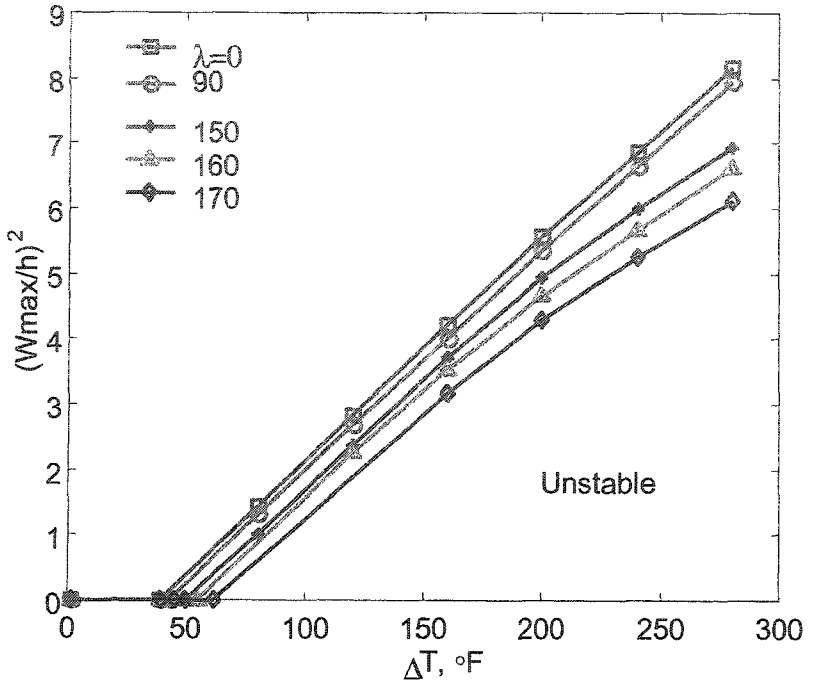

Fig. 5.5 Square of aerothermal deflections versus temperature for a clamped traditional composite plate at various dynamic pressure and $\Lambda = 0°$.

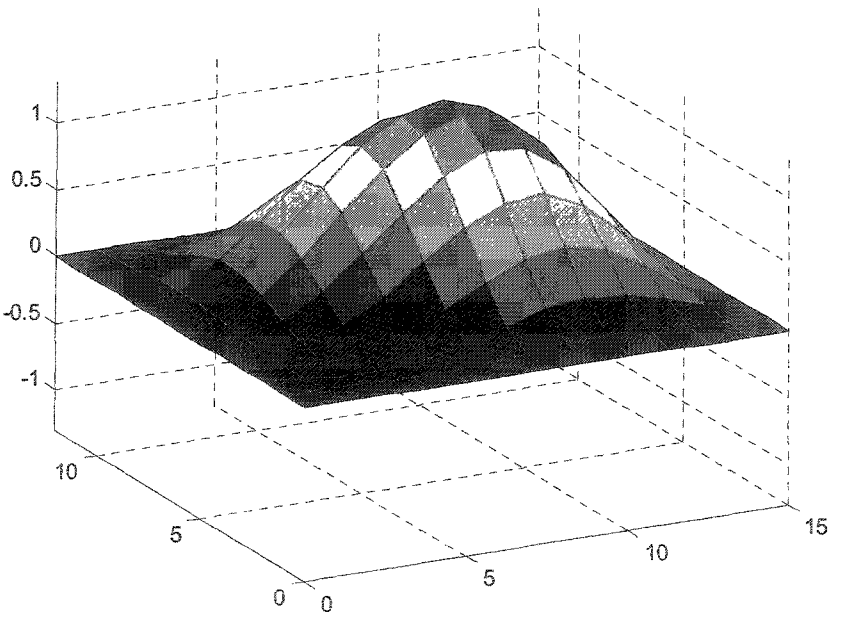

Fig. 5.6 Aerothermal deflection shape for a clamped traditional composite plate at λ = 120, $\Lambda = 0°$ and $\Delta T = 150°F$.

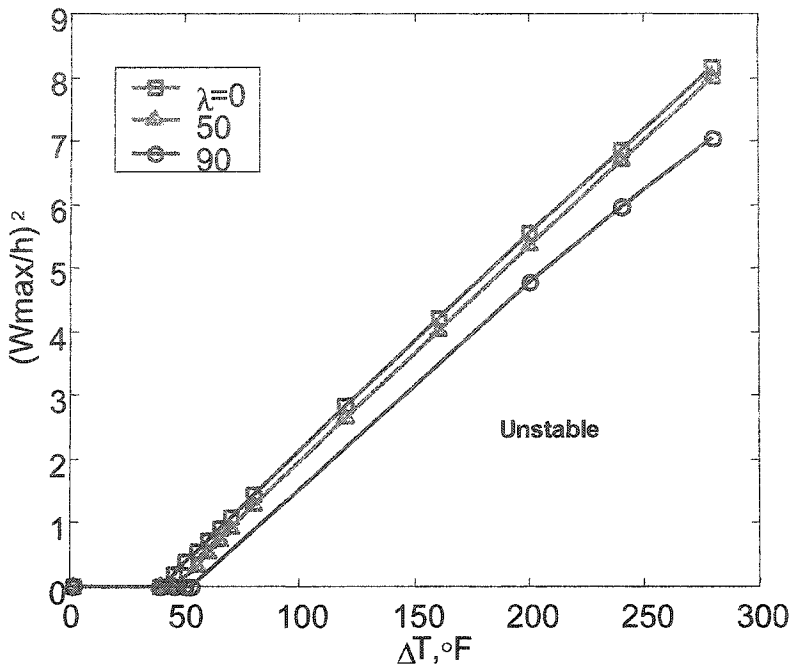

Fig. 5.7 Square of aerothermal deflections versus temperature for a clamped traditional composite plate at $\Lambda = 45°$.

CHAPTER VI PANEL FLUTTER AT ELEVATED TEMPERATURES

Once the plate falls into the flutter or dynamic regions, the Newton-Raphson iterative method used in Chapter V fails to yield converged aerothermal deflection. Therefore, numerical integration in time domain is used here to investigate the panel response in the entire temperature - dynamic pressure (ΔT-λ) domain. The system dynamic equation of motion in the reduced AEM coordinates is rewritten as

$$\left[\overline{M}_b\right]\{\ddot{q}\}+\left[\overline{G}\right]\{\dot{q}\}+2\left[\zeta_i\omega_i\right]\left[\overline{M}_b\right]\{\dot{q}\}+\left(\left[\overline{K}\right]+\left[\overline{K}_q\right]+\left[\overline{K}_{qq}\right]\right)\{q\}=\{\overline{P}_c\} \tag{6.1}$$

where

$$([\overline{M}_b],[\overline{G}],[\overline{K}])=[\Phi_L]^T([M_b],[G],[K_{lin}])[\Phi] \tag{6.2}$$

$$\left[\overline{K}_q\right]=[\Phi_L]^T\sum_{r=1}^{n}q_r\left([K_{1NB}]^{(r)}-[K_{1Nm}]^{(r)}-[K_{1bm}]^{(r)}[K_m]^{-1}[K_{mb}]-[K_{bm}][K_m]^{-1}[K_{1mb}]^{(r)}\right)[\Phi] \tag{6.3}$$

$$\left[\overline{K}_{qq}\right]=[\Phi_L]^T\sum_{r=1}^{n}\sum_{s=1}^{n}q_rq_s\left([K_{2b}]^{(rs)}-[K_{2Nm}]^{(rs)}-[K_{1bm}]^{(r)}[K_m]^{-1}[K_{1mb}]^{(s)}\right)[\Phi] \tag{6.4}$$

$$\{\overline{P}_c\}=[\Phi_L]^T\left(\{P_{\Delta Tb}\}-\{P_{rb}\}-[K_{bm}][K_m]^{-1}\{P_m\}\right) \tag{6.5}$$

and the modal matrix of AEMs [Φ] is obtained from

$$\omega_r^2[M_b]\{\phi_r\}=\left(\lambda_o[A_a]+[K_b]-[K_{bm}][K_m]^{-1}[K_{mb}]\right)\{\phi_r\} \tag{6.6}$$

6.1 Validation of AE Modal method

Either normal modes (NMs) or aeroelastic modes (AEMs) can be used in the finite element modal method. However, the newly introduced AEMs can greatly reduce the number of modes used in flutter analysis.[48] To validate the present modal formulation using AEMs, the LCO results for an aluminum square plate and a rectangular composite plate are determined and compared with LCO results using the NMs. LCO results are studied and presented for the plates at a zero flow angle ($\Lambda = 0°$) and then followed by the nonzero flow angles ($\Lambda \neq 0°$).

Three cases are considered. For a simply supported square aluminum plate of 12×12×0.050 in. (30.5×30.5×0.127 cm) at $\Lambda = 0°$, a 12×3 mesh, or 36 BFS elements in a half plate model is used; at $\Lambda \neq 0°$, a 12×12 mesh, or 144 BFS elements of the full plate model is used. The aerodynamic damping C_a is set as 0.01. For the simply supported isotropic rectangular plate of 15×12×0.050 in. (38.1×30.5×0.13 cm) at $\Lambda \neq 0°$, a 12×12 mesh full plate model is employed. A clamped three-layered [-40/40/-40] Graphite-Epoxy composite plate of 15×12×0.048 in. (38.1×30.5×0.12 cm) is also investigated. The full plate is modeled with 12×12 mesh or 144 BFS elements for both $\Lambda = 0°$ and $\Lambda \neq 0°$.

6.1.1 Zero Flow Angle ($\Lambda = 0°$) Case

For the simply supported isotropic square plate, it is known that $\lambda_{cr} = 512$.[27,40] First, the LCO amplitudes using 2 AEMs ($\lambda_o = 510$, see Fig. 4.4) are determined and compared with results using 6 NMs shown in Fig. 6.1. The present modal formulation using AEMs gives very accurate LCO response. The time history and phase plot of LCO using 2 AEMs at $\lambda = 890$ are shown in Fig. 6.2, which show a clear harmonic type of LCO.

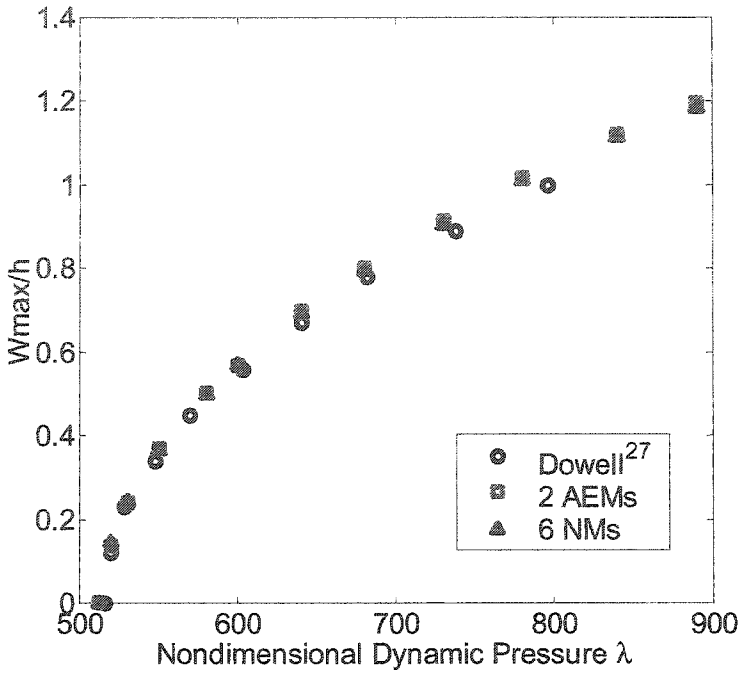

Fig. 6.1 Comparison of LCO amplitudes between Dowell[27] and finite element modal method using 2 AEMs and 6 NMs for a simply supported isotropic square plate at $\Lambda = 0°$.

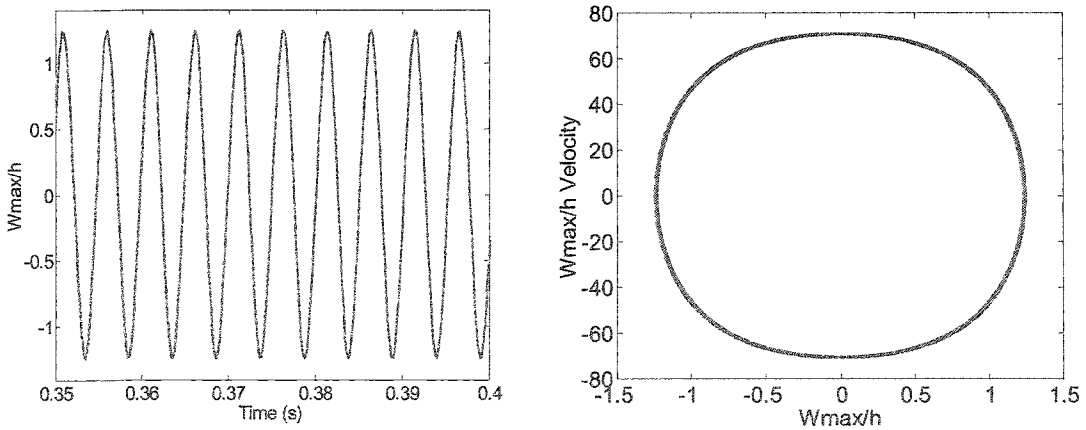

Fig. 6.2 Time history and phase plot using 2 AEMs for a simply supported isotropic square plate at $\lambda = 890$ and $\Lambda = 0°$.

The convergence of LCO amplitudes using various numbers of AEMs at $\lambda_0 = 510$ is investigated and shown in Fig. 6.3. It can be seen clearly that the LCO converges fast. It can be also seen in Table 6.1, which shows the modal participation (MP) percentage values for the 6 AEMs, where the first and second AEMs are dominant. Table 6.1 also

lists the MP values for 6 NMs, which show that the method using AEMs converges faster than NMs.

Table 6.1 Comparison of MP of 6 AEMs ($\lambda_o = 510$) and 6 NMs for the simply supported isotropic square plate at $\Lambda = 0°$

		Modal Participation, %					
W_{max}/h	Mode No.	q1	q2	q3	q4	q5	q6
0.24	AEM	53.18	46.35	0.36	0.05	0.03	0.01
	NM	42.37	41.82	11.87	2.46	1.03	4.31
0.51	AEM	63.93	34.83	0.91	0.21	0.08	0.03
	NM	59.86	30.50	5.96	2.28	0.88	0.46
1.02	AEM	67.32	29.43	1.51	1.16	0.44	0.14
	NM	29.33	45.76	15.23	7.49	0.80	1.38

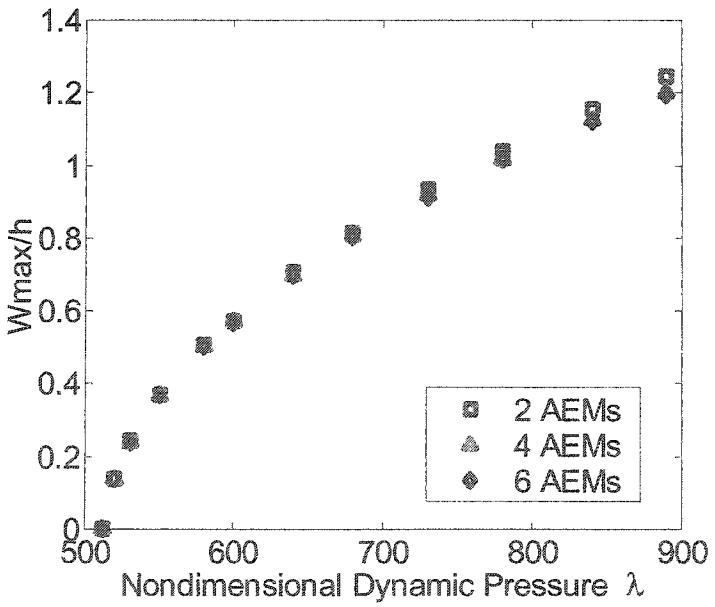

Fig. 6.3 Convergence of LCO amplitude using AEMs for a simply supported isotropic square plate at $\Lambda = 0°$.

One question arises in this procedure: where should the AEMs be selected? This is because the mode shapes of AEMs depend on dynamic pressure λ. Intuitively, λ_o should be selected near the onset of flutter. We know $\lambda_{cr} = 512$ for a simply supported isotropic square plate. So all the results obtained above are based on AEMs at $\lambda_o = 510$. To find out the effect of different λ_o values on LCO results, Fig. 6.4 shows the difference of LCO amplitudes using 2 AEMs at three different λ_o values. The largest difference of LCO amplitudes between $\lambda_o = 400$ and 510 is about 10%. This indicates that AEMs selection is not much sensitive to LCO results, but the closer to the coalescence λ_{cr}, the more accurate the result will be.

For the clamped rectangular laminated [-40/40/-40] composite plate, Fig. 6.5 shows the convergence and accuracy of LCO results using 2, 4 and 6 AEMs (λ_o = 245), respectively, and comparing with as many as 36 NMs. The MP values in Table 6.2 shows that higher modes gradually contributed more at larger LCO amplitudes and they should be included.

Table 6.2 MP of 6 AEMs ($\lambda_o = 245$) for a clamped traditional composite plate at $\Lambda = 0°$

	Modal Participation, %					
W_{max}/h	q1	q2	q3	q4	q5	q6
0.22	42.26	47.38	1.21	6.91	1.22	1.00
0.57	40.23	43.88	2.80	8.95	1.34	2.77
1.04	35.42	38.47	7.89	10.38	1.66	6.18

6.1.2 Nonzero Flow Angle ($\Lambda \neq 0°$) Case

For a particular flow yaw angle, the AEMs are selected and generated with respect to that flow angle, and then determine the LCO response of the specified flow angle. Figure 6.6 shows the LCO amplitudes of the simply supported isotropic square plate at $\Lambda = 15°$ using 2 and 6 AEMs ($\lambda_o = 515$) and compared with those using 36 NMs. The results show that even using 2 AEMs it is in good agreement with those using 36 NMs. It is seen from Table 6.3 that the first two AEMs are the most dominant with all others having very small contribution.

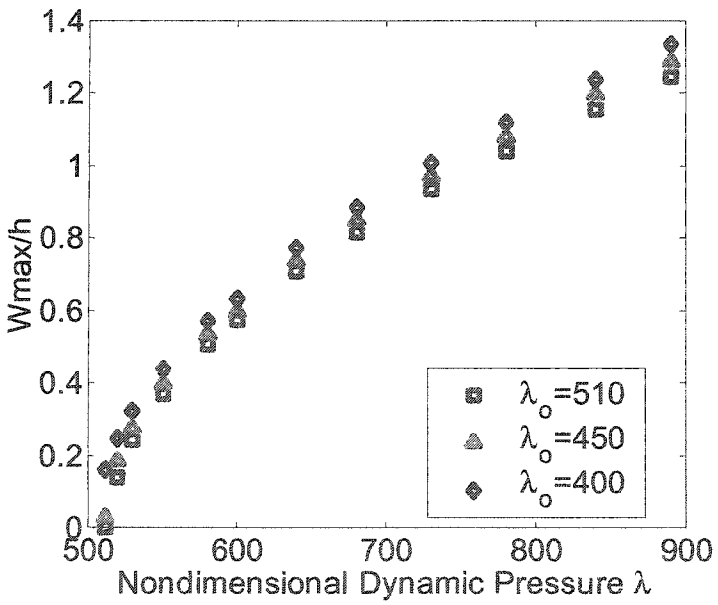

Fig. 6.4 LCO amplitudes for a simply supported isotropic square plate at $\Lambda = 0°$ using 2 AEMs selected at different λ_o.

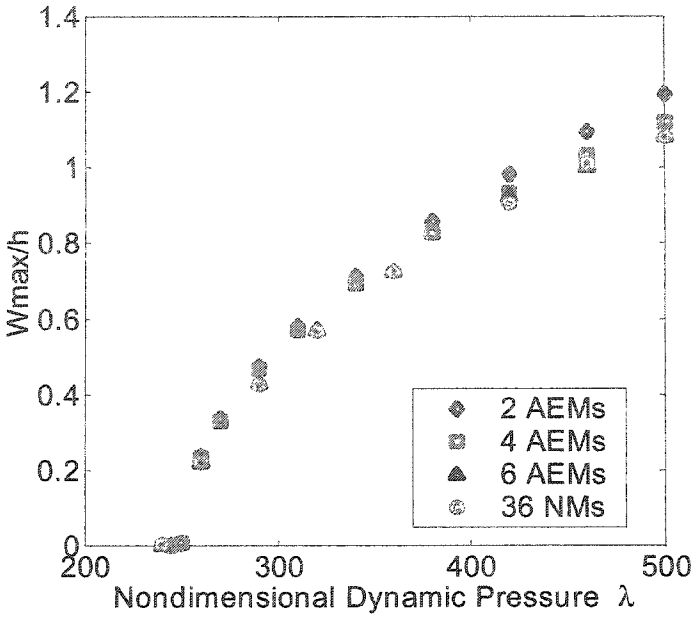

Fig. 6.5 Comparison of LCO amplitudes using 2, 4 or 6AEMs ($\lambda_o = 245$) and 36 NMs for a clamped rectangular [-40/40/-40] composite plate at $\Lambda = 0°$.

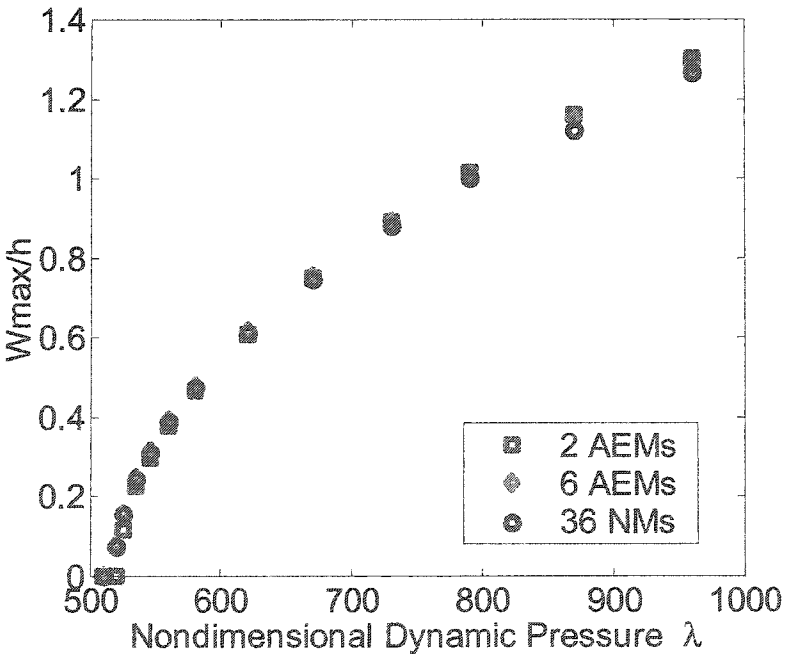

Fig. 6.6 Comparison of LCO amplitudes using 2 or 6 AEMs ($\lambda_o = 515$) and 36 NMs for a simply supported isotropic square plate at $\Lambda = 15°$.

Table 6.3 MP of 6 AEMs ($\lambda_o = 515$) for a simply supported isotropic square plate at $\Lambda = 15°$

	Modal Participation, %					
W_{max}/h	q1	q2	q3	q4	q5	q6
0.08	50.69	48.49	0.04	0.36	0.32	0.09
0.48	60.68	38.23	0.07	0.28	0.53	0.21
1.01	60.32	37.32	0.13	0.64	1.04	0.56

For the clamped rectangular [-40/40/-40] composite plate, the results are shown in Fig. 6.7 and Table 6.4. Again, it is observed that higher frequency AEMs gradually contribute more at larger amplitudes. Hence it is necessary to use more AEMs for large amplitude flutter analysis.

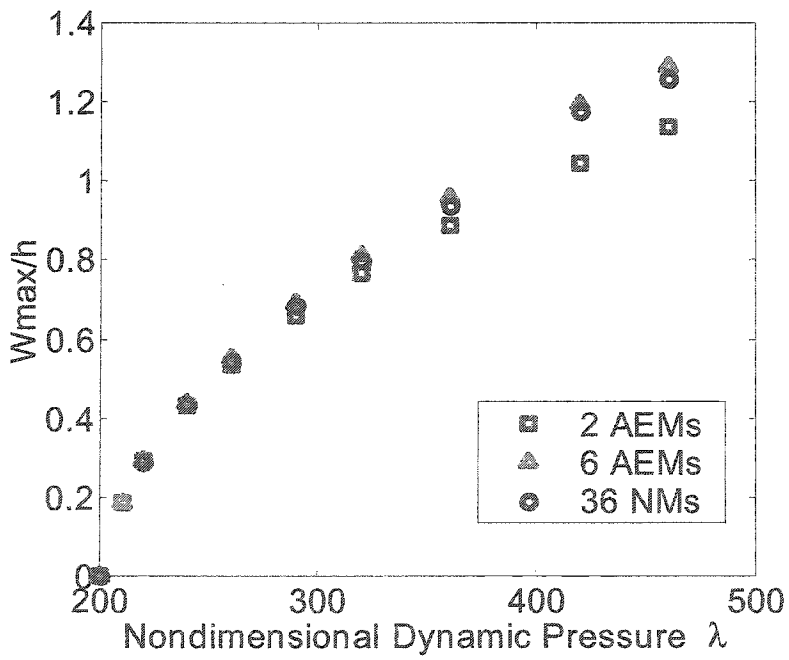

Fig. 6.7 Comparison of LCO amplitudes using 6 AEMs ($\lambda_o = 200$) and 36 NMs for a clamped rectangular [-40/40/-40] composite plate at $\Lambda = 15°$.

Table 6.4 MP of 6 AEMs ($\lambda_o = 200$) for a clamped [-40/40/-40] composite plate at $\Lambda = 15°$

$\frac{W_{max}}{h}$	Modal Participation, %					
	q1	q2	q3	q4	q5	q6
0.18	51.50	45.90	0.27	1.41	0.24	0.68
0.55	53.93	38.54	0.58	4.55	0.43	1.96
0.96	46.44	38.39	2.52	7.25	0.78	4.61

6.1.3 Nonzero Flow Angle ($\Lambda \neq 0°$) with Thermal Load

It is necessary to investigate whether AEMs can be used for panels under combined thermal and aerodynamic loads. For a given temperature and a particular flow angle, AEMs are first selected and generated with respect to the flow angle only (without the presence of aerothermal load), then the thermal buckling deflection and LCO response at the specified flow angle and temperature are determined.

The example given here is the simply supported isotropic square plate at a flow angle $\Lambda = 15°$ and temperature $\Delta T/\Delta T_{cr} = 1.5$. Both the static aerothermal deflection and the dynamic LCO response are determined and drawn versus dynamic pressure λ in Fig. 6.8 using 16 NMs and 6 AEMs ($\lambda_o = 515$), respectively. It is seen that the results are very close to each other. In Table 6.5, the MP values also show that the first two AEMs are the most dominant modes with all others having very small contribution except at $\lambda = 200$, where $W_{max}/h = 0$ and the MP values are meaningless.

Table 6.5 MP of 6 AEMs ($\lambda_o = 515$) for a simply supported isotropic square plate at $\Lambda = 15°$ and $\Delta T/\Delta T_{cr} = 1.5$

λ	W_{max}/h	Modal Participation, %					
		q1	q2	q3	q4	q5	q6
0	0.62	50.74	48.12	0.25	0.37	0.49	0.04
100	0.53	52.01	47.46	0.21	0.15	0.14	0.03
200	≈ 0	22.21	26.87	0.41	0.64	25.19	24.68
300	0.32	62.82	35.29	0.06	0.93	0.67	0.12
400	0.69	56.99	39.69	0.12	0.92	1.84	0.43
500	0.92	26.93	64.88	0.18	2.85	3.76	1.38
600	1.10	82.58	11.69	0.99	3.17	0.16	1.40

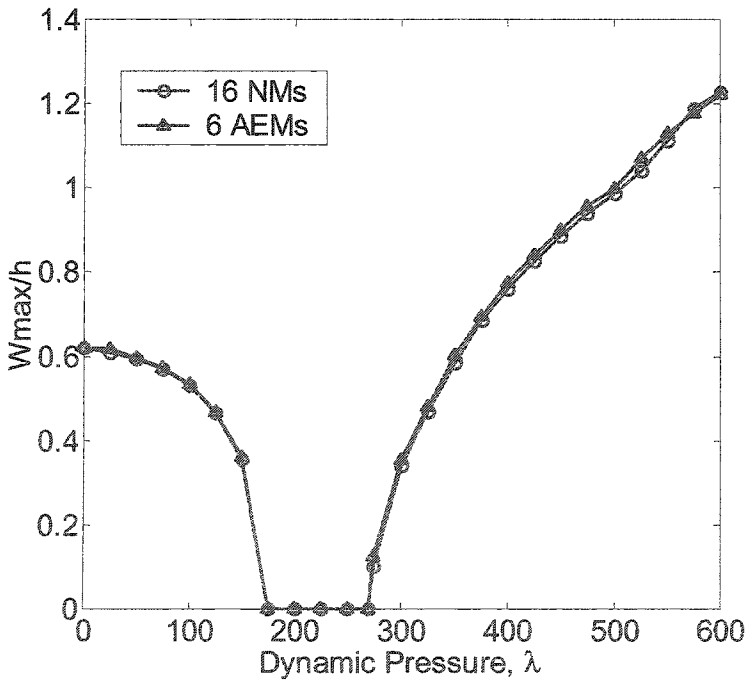

Fig. 6.8 Comparison of aerothermal deflection and LCO amplitude using 16 NMs and 6 AEMs for a simply supported square aluminum plate at $\Delta T/\Delta T_{cr} = 1.5$ and $\Lambda = 15°$.

Through the above validation, numerically, as long as the airflow aerodynamics is involved, the usually needed 25 or 36 NMs for flutter analysis could be reduced to 6 AEMs or less. The computational time is thus reduced greatly. For any case, of course, modal convergence study should be conducted first to determine the proper number of AEMs needed.

6.2 Flutter and Stability Regions

There are four types of panel behavior: flat and stable, buckled but dynamically stable, LCO and chaos. The plate's dynamic behaviors, i.e., LCO and chaotic motions, can be cataloged further into 4 types: nearly simple harmonic LCO, periodic LCO, non-periodic oscillation and chaotic oscillation. The clamped $[0/-45/45/90]_s$ composite plate, with the critical temperature ΔT_{cr} = 39.3°F (21.8°C), is investigated with ΔT varying from 0 to 280°F or 155.6° C (T_{ref} = 70°F, so T is 70°F to 350°F) and λ from 0 to 800, and two flow angles Λ = 0° and 45° are considered. The time responses at maximum deflection are obtained and analyzed with varying ΔT and λ.

A two-dimensional Poincare map[93] is employed to identify various types of motion. Compared with a normal phase plot, which is displacement versus velocity for all continuous instants of time, Poincare map plots two coordinates versus each other at the time instants when an event occurs. In present study, the two coordinates are selected as the displacements at maximum point and plate center. The event is defined as the velocity at maximum point reduces to zero from positive, indicating the point reaches the local maximum position. At the time instant that the event happens, plot the

displacement at maximum point versus the displacement at plate center (W_c in Poincare map).

6.2.1 Traditional Composite Plate

It is found that 6 AEMs are enough to obtain a converged solution for the traditional $[0/-45/45/90]_s$ composite plate, as shown in Fig. 6.9 and Table 6.6. W_{max}/h versus dynamic pressure is plotted in Fig. 6.9 for the traditional composite plate at $\Lambda = 0°$ and $\Delta T = 50°F$ ($\Delta T/\Delta T_{cr} = 1.26$) using 25 NMs and 6 AEMs, respectively. The comparison indicates that 6 AEMs result has excellent agreement with that of 25 NMs. Table 6.6 shows a fast convergence of solution with very small contributions from higher modes, e.g. the contribution form the fifth and sixth are all less than 2%.

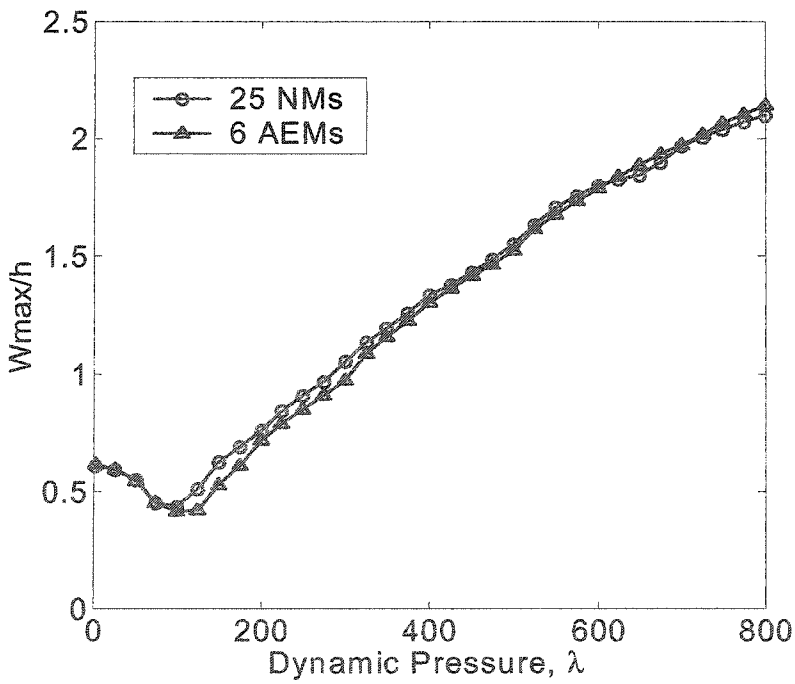

Fig. 6.9 Comparison of aerothermal deflection and LCO amplitude using 25 NMs and 6 AEMs for a clamped traditional $[0/-45/45/90]_s$ composite plate at $\Delta T = 50°F$ and $\Lambda = 0°$.

Table 6.6 MP of 6 AEMs ($\lambda_o = 464$) for a clamped traditional $[0/-45/45/90]_s$ composite plate at $\Lambda = 0°$ and $\Delta T = 50°F$

		Modal Participation, %					
λ	W_{max}/h	q1	q2	q3	q4	q5	q6
0	0.61	49.68	48.05	1.70	0.19	0.24	0.13
100	0.41	52.41	25.00	11.61	9.27	1.19	0.51
200	0.72	53.54	36.46	4.92	3.57	1.09	0.04
300	0.97	52.76	43.32	1.19	1.97	0.53	0.60
400	1.13	47.76	50.36	1.32	0.30	0.26	0.11
500	1.39	40.53	55.92	0.51	1.61	1.28	1.44
600	1.79	63.42	26.82	3.27	3.71	1.93	0.83
700	1.98	60.11	31.62	2.80	2.66	1.76	1.03
800	2.14	53.93	41.67	2.04	1.50	0.74	0.11

The four typical types of motions are shown in Figs. 6.10 - 6.13 using 6 AEMs, represented with time history, phase plot, power spectrum density (PSD) plot and Poincare map.

At $\lambda = 500$, $\Lambda = 0°$ and $\Delta T/\Delta T_{cr} = 1.0$, as shown in Fig. 6.10, the closed phase plot and one dominant frequency in the PSD plot clearly indicate a simple harmonic LCO. There is only one point in Poincare map, standing for when the maximum point reaches the local maximum value, the plate center has just one position corresponding to it. This one-one correlation indicates periodic motion.

At $\lambda = 275$, $\Lambda = 0°$ and $\Delta T/\Delta T_{cr} = 2.0$, the vibration type changes to periodic, as shown in Fig. 6.11. The phase plot comprises a small orbit about each buckled state and a large orbit. The PSD plot indicates three or four dominant frequencies. In general, one point in a Poincare map expresses the recurrent behavior of a motion, which in turn, stands for a periodic motion.

The plate may also show a more complex periodic motion at $\lambda = 200$, $\Lambda = 0°$ and $\Delta T/\Delta T_{cr} = 3.0$, as shown in Fig. 6.12. At such a combination of high $\Delta T/\Delta T_{cr}$ and moderate λ, the plate motion evolves from periodic oscillation to non-periodic oscillation. The Poincare map shows a cluster of points gathering in the upper right and lower left section of the plot, indicating that when the maximum point reaches the local maximum position, plate center can vibrate somewhere on a straight line position but shows no recurrence.

At the combination of medium dynamic pressure and high temperature, such as $\lambda = 325$, $\Lambda = 0°$ and $\Delta T/\Delta T_{cr} = 4.0$ as shown in Fig. 6.13, the plate is likely to undergo chaotic oscillation. Compared with non-periodic oscillation in Fig. 6.12, chaos shows diffusion on phase plot that almost fills the entire region from minima to maxima, and the broadening of power spectrum peaks in the PSD plot. In Poincare map, the cluster of points stretches over the entire region from negative and positive, indicating when the maximum point reaches the local maximum, plate center can vibrate anywhere, which leads to the unpredictability of the motion. The phase plot indistinctly shows the strange attractors at about $W_{max}/h = -1.8$ and 1.8, which is not seen in non-periodic oscillation.

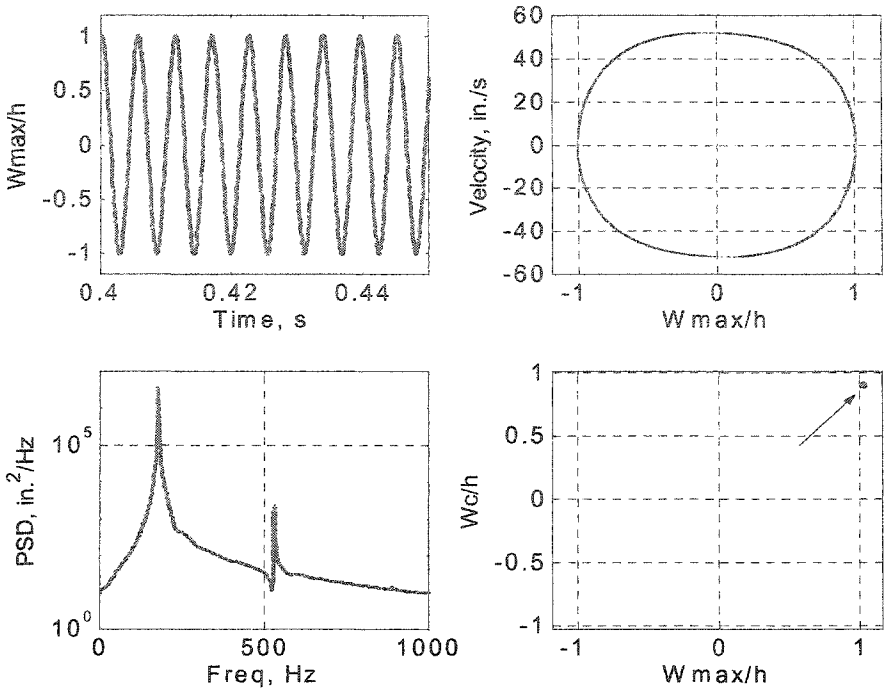

(a) Time Histroy (b) Phase Plot
(c) PSD (d) Poincare Map

Fig. 6.10 Simple harmonic LCO of a clamped traditional $[0/-45/45/90]_s$ composite plate at $\lambda = 500$, $\Lambda = 0°$ and $\Delta T/\Delta T_{cr} = 1.0$.

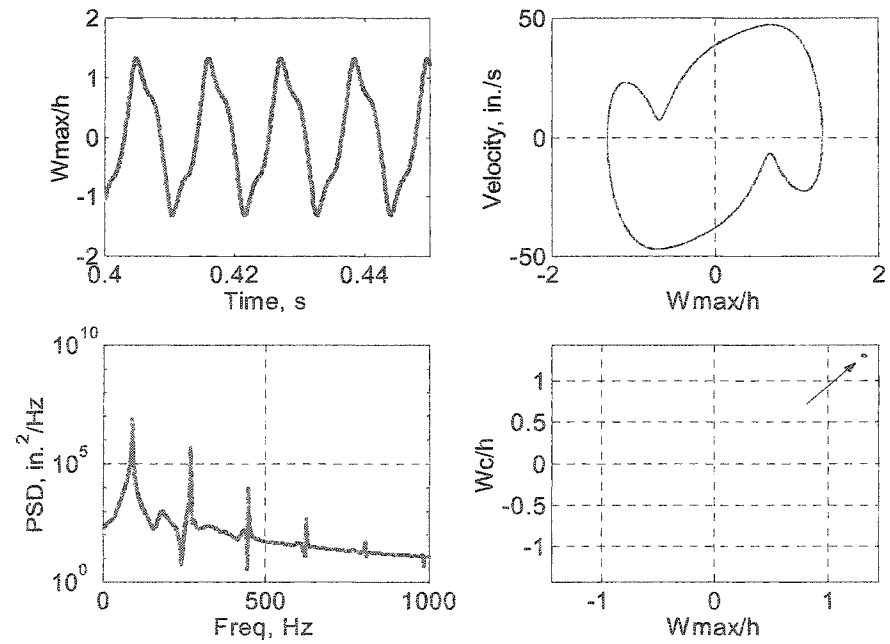

Fig. 6.11 Periodic LCO of a clamped traditional $[0/-45/45/90]_s$ composite plate at $\lambda = 275$, $\Lambda = 0°$ and $\Delta T/\Delta T_{cr} = 2.0$.

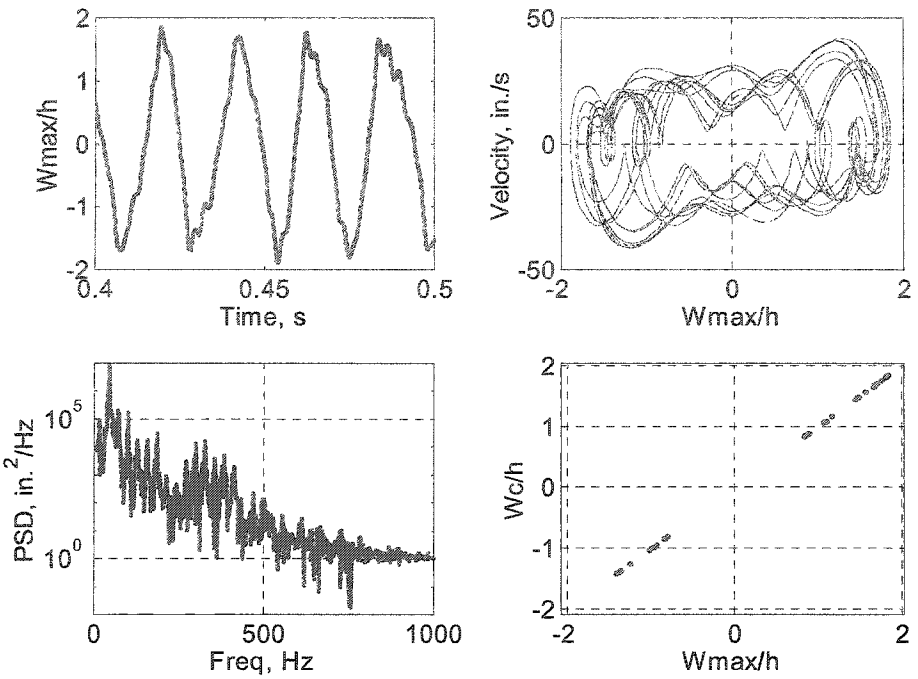

Fig. 6.12 Non-periodic oscillation of a clamped traditional $[0/-45/45/90]_s$ composite plate at $\lambda = 200$, $\Lambda = 0°$ and $\Delta T/\Delta T_{cr} = 3.0$.

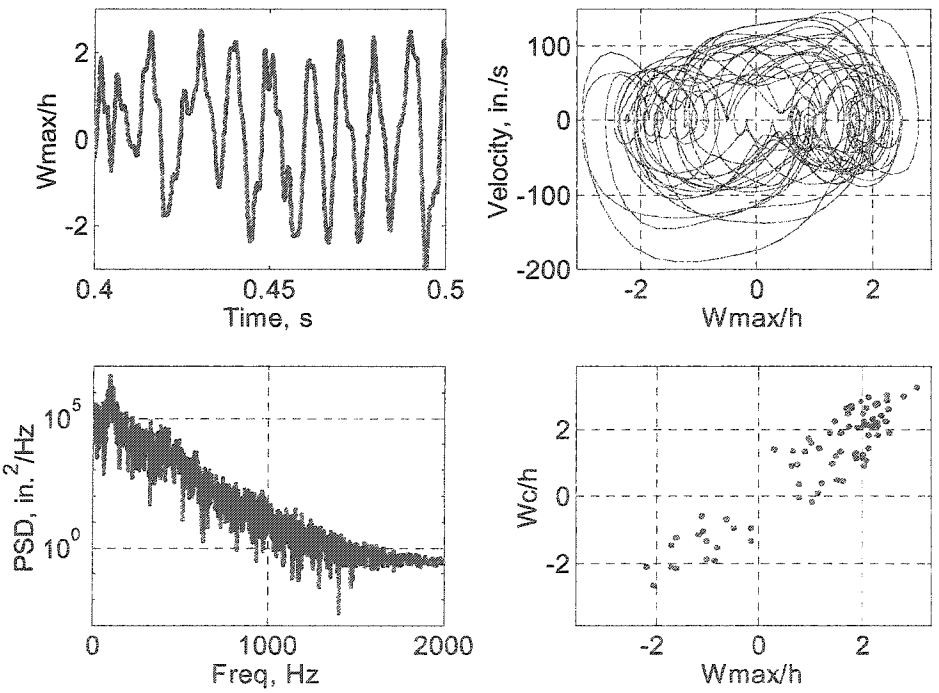

Fig. 6.13 Chaotic oscillation of a clamped traditional $[0/-45/45/90]_s$ composite plate at $\lambda = 325$, $\Lambda = 0°$ and $\Delta T/\Delta T_{cr} = 4.0$.

The plate's aerothermal deflection and LCO amplitude at the maximum point versus dynamic pressure at various temperatures are shown in Fig. 6.14 (see Fig. 6.9 for ΔT = 50°F). The left side curves show the aerothermal deflection, before λ has yet to reach the critical value (λ_{cr}) for flutter. The right side curves are the LCO amplitudes at different ΔT. It is seen that, with the increase of λ, aerothermal deflection decreases. The decrease is accredited to stiffened plate with the increase of λ. At $\Delta T > 60°F$, the plate cannot be blown to flat and begins periodic flutter at $\lambda > 150$, which is in between the left side and the right side curves. It is noticed that at low temperature, the LCO amplitudes increase smoothly with the increase of λ. This is where harmonic oscillation occurs. As temperature goes up, shown in dashed lines, the irregular motion begins to occur, indicating that the flutter has either periodic LCO, non-periodic or chaotic motions.

Figure 6.15 expresses the stability regions in the temperature - dynamic pressure (ΔT-λ) domain. There are essentially four regions: flat and stable, buckled but dynamically stable, LCO flutter (including harmonic, periodic and non-periodic motions), and chaos. The boundary between the LCO region and chaos region can be determined precisely using the bifurcation diagram and the Lyapunov exponent,[14] however, this is not the interest of this research. The periodic, non-periodic motions lie in between harmonic LCO and chaos. With the increase of ΔT and λ, the nearly simple harmonic LCO has the tendency to evolve into periodic LCO, the periodic region therefore resides in the lower right of LCO region, between LCO and Chaos. Figure 6.15 also shows the lines inside the LCO region on which the flutters have the same amplitudes, and the lines inside the buckling region on which the plate has the same maximum aerothermal deflections.

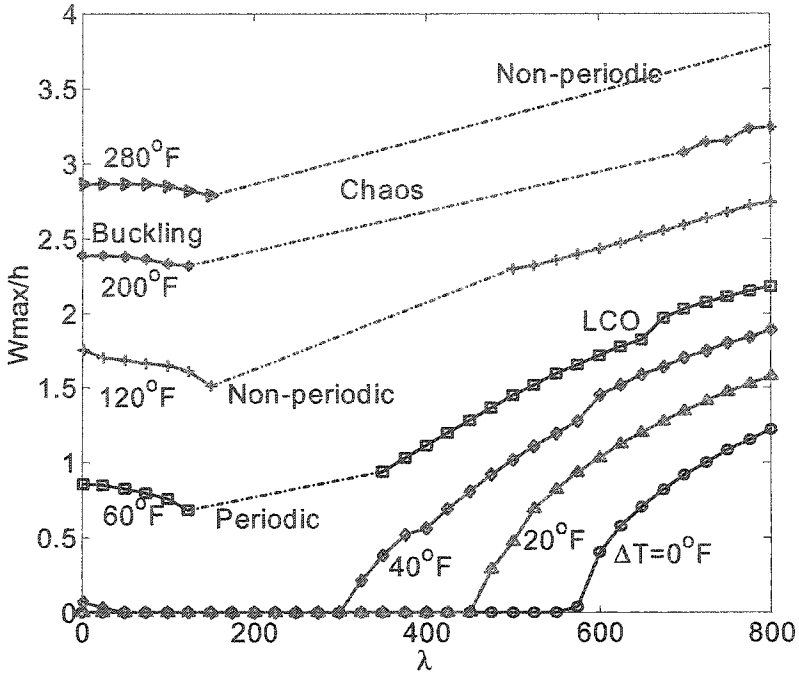

Fig. 6.14 Aerothermal deflection and LCO amplitude versus dynamic pressure λ of a clamped traditional $[0/-45/45/90]_s$ composite plate at $\Lambda = 0°$.

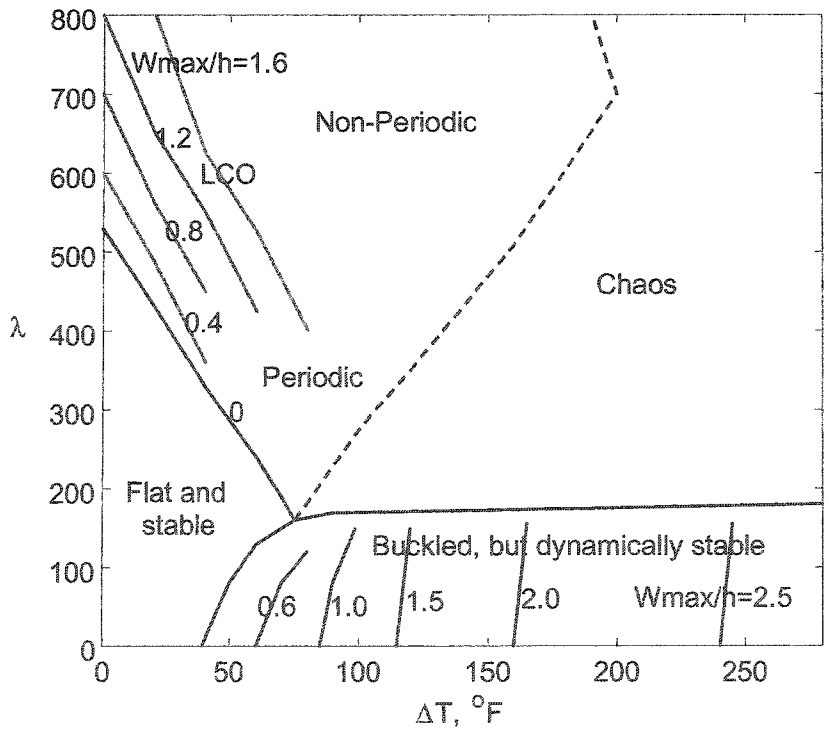

Fig. 6.15 Stability regions in temperature - dynamic pressure (ΔT-λ) domain of the clamped traditional $[0/-45/45/90]_s$ composite plate at $\Lambda = 0°$.

At flow angle $\Lambda = 45°$, the stability regions are plotted in temperature and dynamic pressure (ΔT-λ) domain as shown in Fig. 6.16. Compared with zero flow angle in Fig. 6.15, both the flat and buckled regions are decreased due to a weaker stiffness in the 45° direction, e.g., λ_{cr} is 344 at $\Lambda = 45°$ versus 532 at $\Lambda = 0°$, and buckled region is up bounded at $\lambda = 90$ versus 170 at $\Lambda = 0°$.

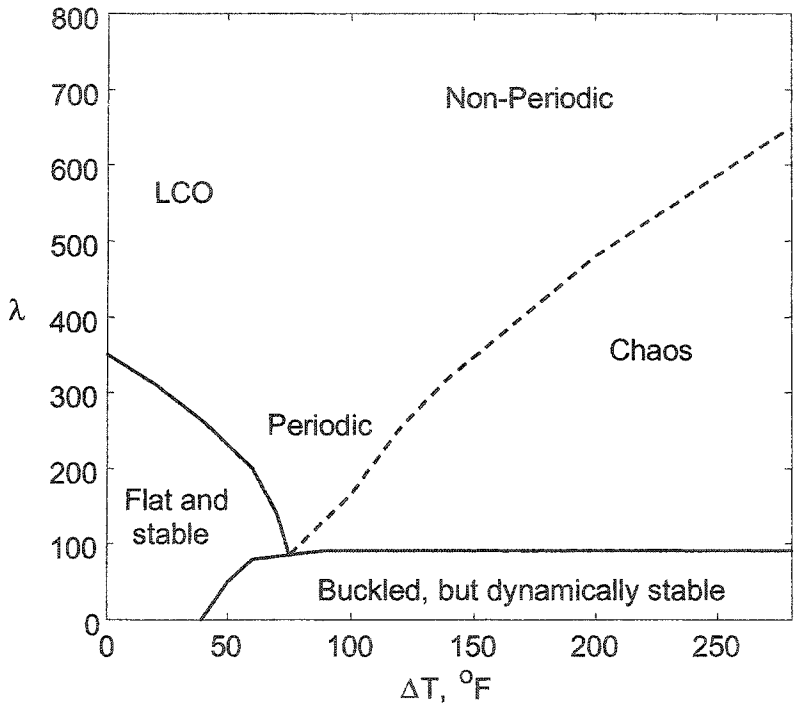

Fig. 6.16 Stability regions in temperature - dynamic pressure (ΔT-λ) domain of the clamped traditional $[0/-45/45/90]_s$ composite plate at $\Lambda = 45°$.

6.2.2 SMAHC plates

With the embedding of SMA, the flutter response of the SMAHC plates can be improved drastically. It is found that using 6 AEMs are more than enough to obtain a converged solution for SMAHC plates. Figure 6.17 shows the stability regions for an SMAHC plate with ($v_s = 10\%$ and $\varepsilon_r = 3\%$) at $\Lambda = 0°$. Compared with the traditional

composite plate shown in Fig. 6.15, the flat and stable region of the SMAHC plate is increased greatly. The critical thermal buckling temperature ΔT_{cr} is increased to 245°F at $\lambda = 0$. It is interesting to note that the boundary between the flat and stable region and LCO flutter region first goes up as temperature increases, then goes down. This is due to the counteraction between thermal expansion effect of the composite matrix and the recovery force of SMA. Thermal expansion has the tendency to soften the plate and reduce λ_{cr}, while the SMA recovery force stiffens the plate and increases λ_{cr}. At low temperature, the SMA recovery force overcomes thermal expansion, the plate is stiffened, and λ_{cr} is increased. With the increasing temperature, the SMA recovery force saturates and thermal expansion effect gradually becomes dominant, and the plate displays the reduced stiffness and reduced λ_{cr}. It is seen that at $\Delta T = 280°F$, the plate is buckled and the λ_{cr} is lower than that at T_{ref}. Therefore, SMA volume fraction v_s and prestrain ε_r can be further adjusted to suppress the buckling completely and increase the λ_{cr} at high temperature.

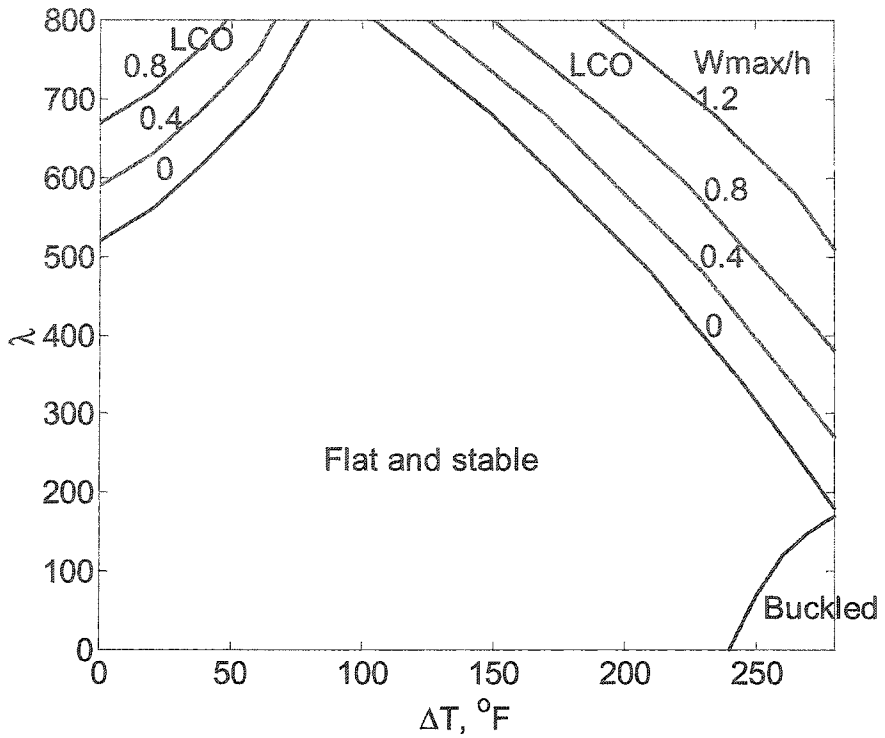

Fig. 6.17 Stability regions in temperature - dynamic pressure (ΔT-λ) domain of the clamped SMAHC (v_s = 10% and ε_r = 3%) plate at Λ = 0°.

For the SMAHC plate with (v_s = 10% and ε_r = 5%), which increases ε_r from 3% to 5% only, as shown in Fig. 6.18, it is seen that the flat and stable region occupies most of the area. Compared with Fig. 6.17, the flat and stable region is further increased and the buckled region is completely suppressed and disappeared from the ΔT-λ domain investigated. Moreover, λ_{cr} at ΔT = 280°F is almost the same as that at T_{ref}.

What is the effect of flow yaw angle on stability region? Figures 6.19 and 6.20 display the stability regions at flow angle Λ = 45° for the SMAHC plates with (v_s = 10% and ε_r = 3%) and (v_s = 10% and ε_r = 5%), respectively. Compared with the corresponding plots for flow angle Λ = 0°, the flat and stable region is smaller.

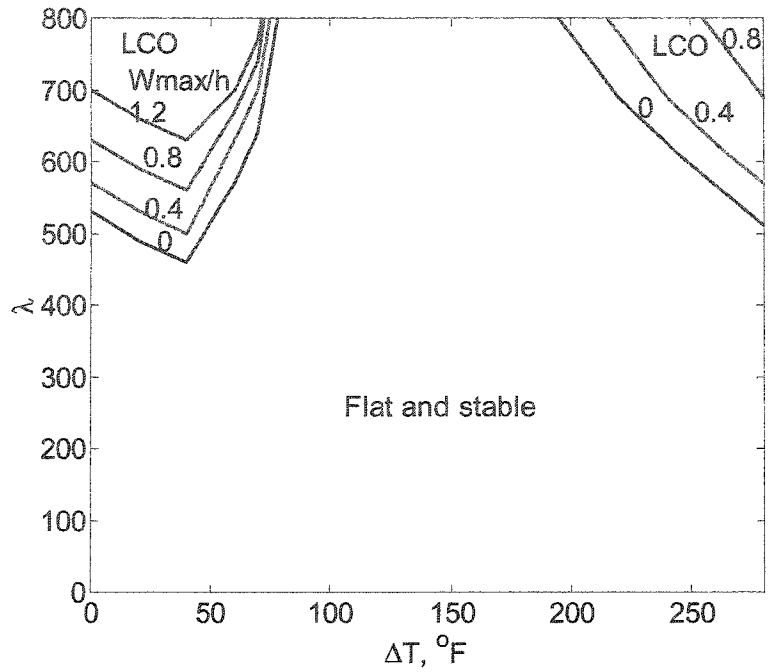

Fig. 6.18 W_{max}/h versus dynamic pressure λ and temperature ΔT of a clamped SMAHC ($v_s = 10\%$ and $\varepsilon_r = 5\%$) plate at $\Lambda = 0°$.

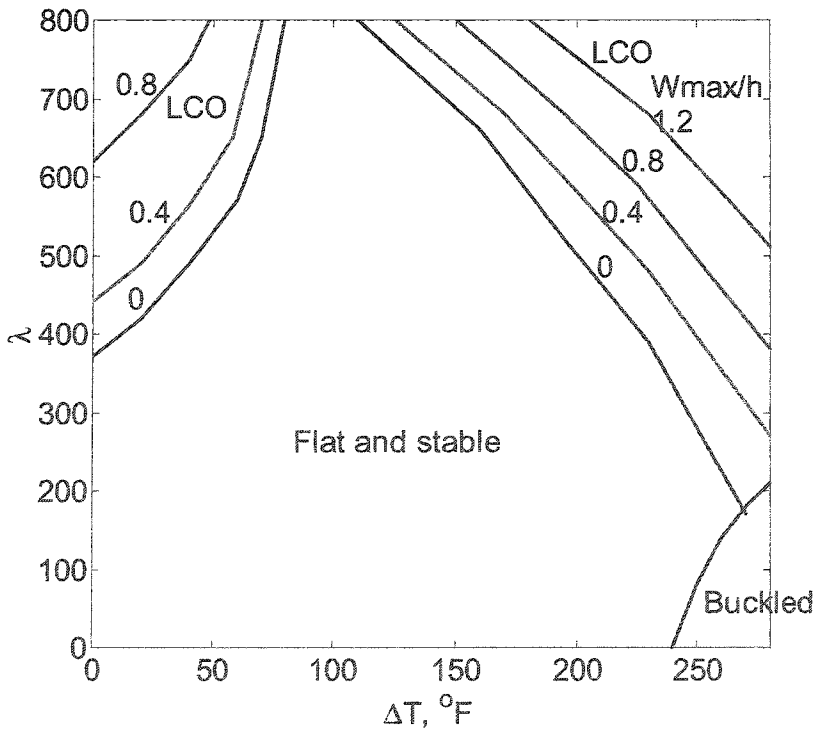

Fig. 6.19 Wmax/h versus dynamic pressure λ and temperature ΔT of a clamped SMAHC ($v_s = 10\%$ and $\varepsilon_r = 3\%$) plate at $\Lambda = 45°$.

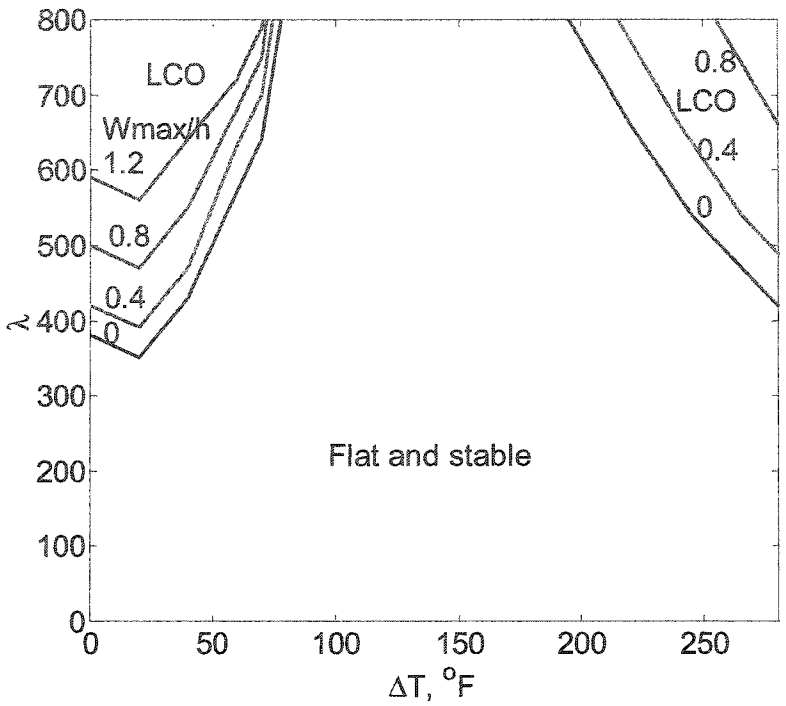

Fig. 6.20 W_{max}/h versus dynamic pressure λ and temperature ΔT of a clamped SMAHC ($v_s = 10\%$ and $\varepsilon_r = 5\%$) plate at $\Lambda = 45°$.

CHAPTER VII RANDOM VIBRATION AT ELEVATED TEMPERATURES

In this section, the response of traditional composite and SMAHC panels under combined acoustic pressure and thermal loads is investigated. The system dynamic equation of motion in modal coordinates is rewritten as

$$\left[\overline{M}_b\right]\{\ddot{q}\}+2[\zeta_r\omega_r]\left[\overline{M}_b\right]\{\dot{q}\}+\left(\left[\overline{K}\right]+\left[\overline{K}_q\right]+\left[\overline{K}_{qq}\right]\right)\{q\}=\{\overline{P}_c\} \tag{7.1}$$

where

$$([\overline{M}_b],[\overline{K}])=[\Phi]^T([M_b],[K_{lin}])[\Phi] \tag{7.2}$$

$$\left[\overline{K}_q\right]=[\Phi]^T\sum_{r=1}^{n}q_r\left([K_{1NB}]^{(r)}-[K_{1Nm}]^{(r)}-[K_{1bm}]^{(r)}[K_m]^{-1}[K_{mb}]-[K_{bm}][K_m]^{-1}[K_{1mb}]^{(r)}\right)[\Phi] \tag{7.3}$$

$$\left[\overline{K}_{qq}\right]=[\Phi]^T\sum_{r=1}^{n}\sum_{s=1}^{n}q_rq_s\left([K_{2b}]^{(rs)}-[K_{2Nm}]^{(rs)}-[K_{1bm}]^{(r)}[K_m]^{-1}[K_{1mb}]^{(s)}\right)[\Phi] \tag{7.4}$$

$$\{\overline{P}_c\}=[\Phi]^T\left(\{P_t(t)\}+\{P_{\Delta Tb}\}-\{P_{rb}\}-[K_{bm}][K_m]^{-1}\{P_m\}\right) \tag{7.5}$$

and the rth normal mode (NM) $\{\phi_r\}$ is determined from

$$\omega_r^2[M_b]\{\phi_r\}=\left([K_b]-[K_{bm}][K_m]^{-1}[K_{mb}]\right)\{\phi_r\} \tag{7.6}$$

The clamped rectangular $[0/-45/45/90]_s$ traditional composite plate and SMAHC plates with immovable in-plane boundary conditions u(0,y) = u(a,y) = v(x,0) = v(x,b) = 0 are studied. A quarter of the plate is modeled with a 10×10 mesh (100 BFS elements) by

taking advantage of geometrical symmetry for uniformly distributed acoustic and thermal loads. A proportional damping ratio of $\xi_r\omega_r = \xi_s\omega_s$ is used with the fundamental modal damping coefficient ξ_1 equal to 0.02. The FE modal formulation based on NMs is used here because no aerodynamic pressure is involved.

The accuracy of the nonlinear stiffness matrices in modal coordinates has been verified by Azzouz et al.[95] in comparison of the equation coefficients of 3-mode modal equations using finite element modal method and classical PDE/Glerkin method. The validation of simulated random loads is by comparison of the linear displacements with linear analytical results[96] for a simply supported 15×12×0.040 in. (38.1×30.5×0.1 cm) aluminum plate shown in Table 7.1.

The Fokker-Plank-Kolmogorov (FPK) method is an exact solution[61] to the single DOF forced Duffing equation under stationary, Gaussian excitations. The present time domain numerical simulation results are shown in Table 7.2. Although FPK method is applied with white noise, while finite element simulation has to use band-limited white noise, they showed good agreement, especially between FPK and FE 4-mode results.

Table 7.1 Comparison of RMS W_{max}/h of linear analysis between analytical and FE results for a simply-supported 15×12×0.040 in. isotropic plate

SPL	Linear Analytical	Linear FE	Err.
DB	4 modes	4 modes	%
90	0.2759	0.2760	0.0362
100	0.8725	0.8728	0.0362
110	2.7590	2.7600	0.0362
120	8.7248	8.7281	0.0362

Table 7.2 Comparison of RMS W_{max}/h of nonlinear analysis between FPK and FE results for a simply-supported 15×12×0.040 in. isotropic plate

SPL	FPK[61]	FE	
dB	1 mode	1 mode	4 modes
90	0.249	0.174	0.266
100	0.592	0.556	0.578
110	1.187	1.101	1.432
120	2.200	1.914	2.572

7.1 Traditional Composite Plate

In order to select the cut-off frequency used in the random load generation procedure, the frequencies in the whole range of temperature should be investigated. Figure 7.1 shows the lowest 8 frequencies of symmetric normal modes versus temperature. The lowest eight natural frequencies at T_{ref} for the traditional composite plate are also listed in Table 7.3. It is found that the highest natural frequency is 1245.6 Hz, the 8^{th} mode (5,3) at T_{ref} for the whole temperature range of $0°F < \Delta T < 280°F$. A cut-off frequency of 2048 Hz is thus selected for this simulation, which is large enough to cover the frequency shifting due to nonlinear effects and SMA stiffening effect at high temperatures.

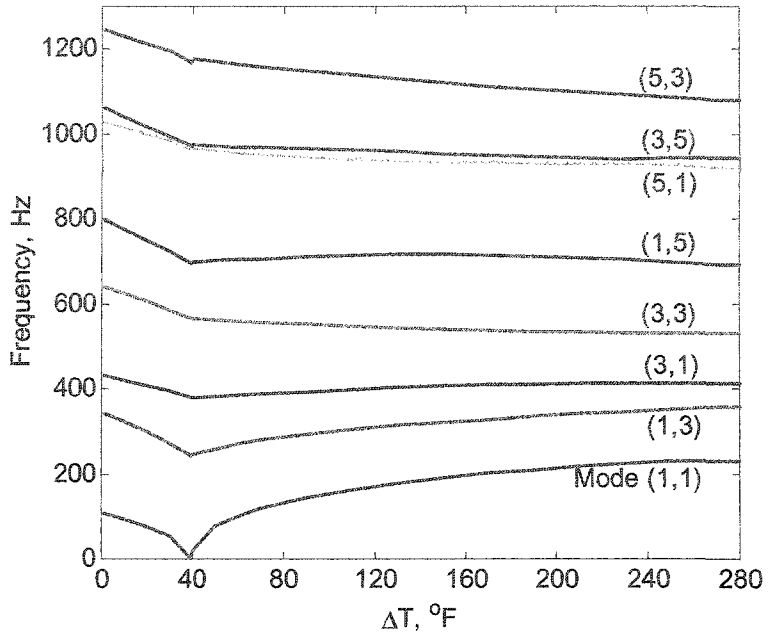

Fig. 7.1 Frequencies of the lowest 8 symmetric modes versus temperature for the thermally pre-buckled or postbuckled traditional composite plate.

In order to eliminate the effect from initial transient response, the first 0.25 sec out of a total period of 2 sec time history is excluded out of the statistical process. To obtain more accurate statistical results, the ensemble average is taken from 5 samples for the present example.

Table 7.3 Natural frequencies (Hz) of a clamped traditional $[0/-45/45/90]_s$ composite plate

Mode shape	(1,1)	(1,3)	(3,1)	(3,3)	(1,5)	(5,1)	(3,5)	(5,3)
Frequency	106.3	344.7	432.9	642.5	799.7	1028.6	1062.2	1245.6

The number of modal coordinates to be included in the analyses for converged deflection solutions is also studied. The Root Mean Square (RMS) maximum non-dimensional deflection (RMS W_{max}/h) versus numbers of modes at SPL = 130 dB and ΔT

= 0°F using 4, 5, 6, 7 and 8 modes are shown in Table 7.4. The results show that 5-8 modes are all to give converged deflection solutions, and six modes are used in the following calculations.

Table 7.4 Modal convergence of RMS W_{max}/h for a clamped traditional $[0/-45/45/90]_s$ composite plate at SPL = 130 dB and ΔT = 0°F

Number of Modes Used	4	5	6	7	8
RMS W_{max}/h	1.8985	1.9601	1.9754	1.9824	1.9869

Two other studies for accurate and converged response predictions are also performed. They are the finite element mesh sizes and the integration time steps. For a six-mode solution it was found that a quarter plate model with a 10×10 mesh is adequate. A time step of integration 1/16384 = 6.1036×10^{-5} sec was first selected, than the time step was cut into one-half. The time histories from the two time steps were found to be identical. Thus, the time step of 1/16384 sec is used. The maximum strain (ε_y) occurs at the middle point along the x-edge.

The time histories, probability density function (PDF) and power spectral density (PSD) of maximum deflection and strain are determined for at SPL = 90 – 130 dB, and ΔT = 0 – 280°F (T = 70 – 350°F). ΔT_{cr} is 39.3°F for the clamped traditional composite plate.

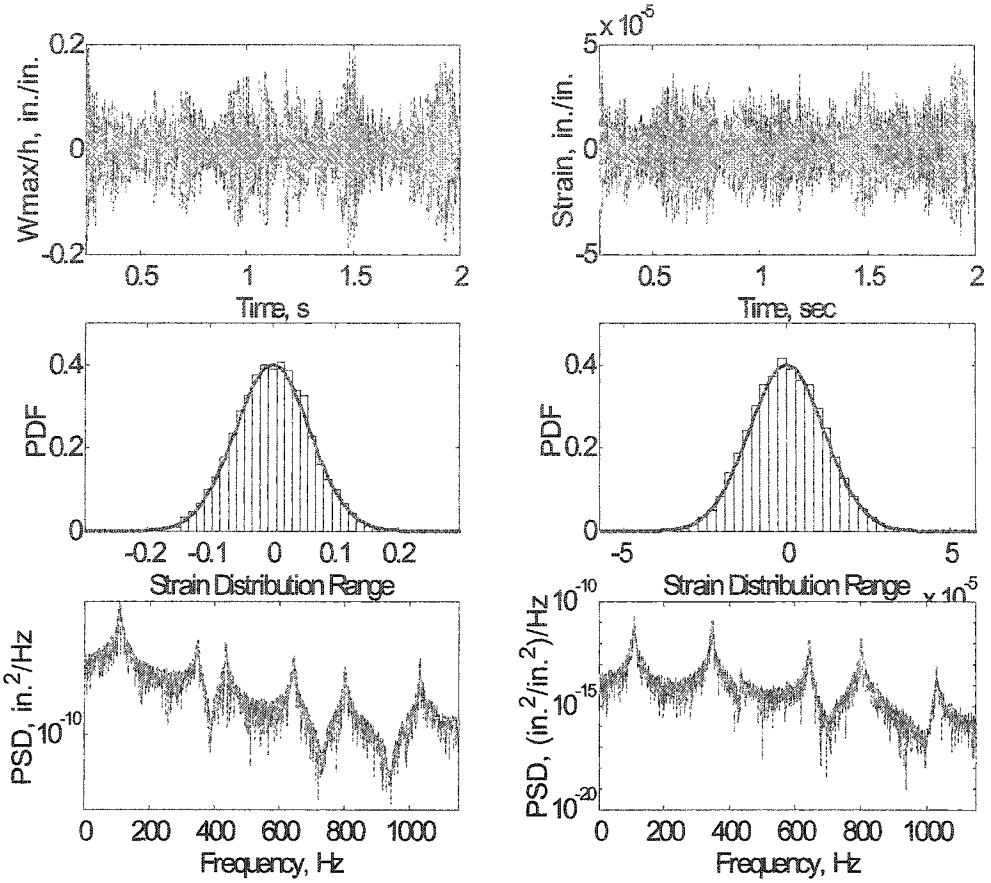

Fig. 7.2 Random response of a clamped traditional $[0/-45/45/90]_s$ composite plate at SPL = 90 dB and $\Delta T = 0°F$.

For $\Delta T = 0°F$, Figs. 7.2, 7.3 and 7.4 show the time history, PDF and PSD of the plate response at SPL = 90, 110 and 130 dB, respectively. At the low 90 dB SPL, the plate behaves basically small deflection (RMS $W_{max}/h = 0.0598$) random vibration dominated by the fundamental (1,1) mode as shown in the PSD plots of Fig. 7.2. All the six modes can be identified and they are close to frequencies obtained by eigen-solution shown in Table 7.1. The probability distributions for deflection and strain are both close to Gaussian. The time history at the high 130 dB SPL in Fig. 7.4 is clearly at large deflection ($W_{max}/h > 1.0$) nonlinear random vibration. This is demonstrated by the peaks

in PSD plot that they are broadening and shifting to the higher frequency, and by the presence of a non-zero mean in-plane strain shown in the strain plots. The large deviation from the Gaussian is shown by the strain PDF, which shows clearly a positive mean. The tensional in-plane stresses induced by large deflection always lead to a positive in-plain strain, which are in turn coupled with bending strain. At SPL = 110 dB in Fig. 7.3, RMS W_{max}/h is around 1.0 with six modes just identifiable and shifted to the right slightly (five modes is identified for strain). No snap-through was found in the ΔT = 0°F results.

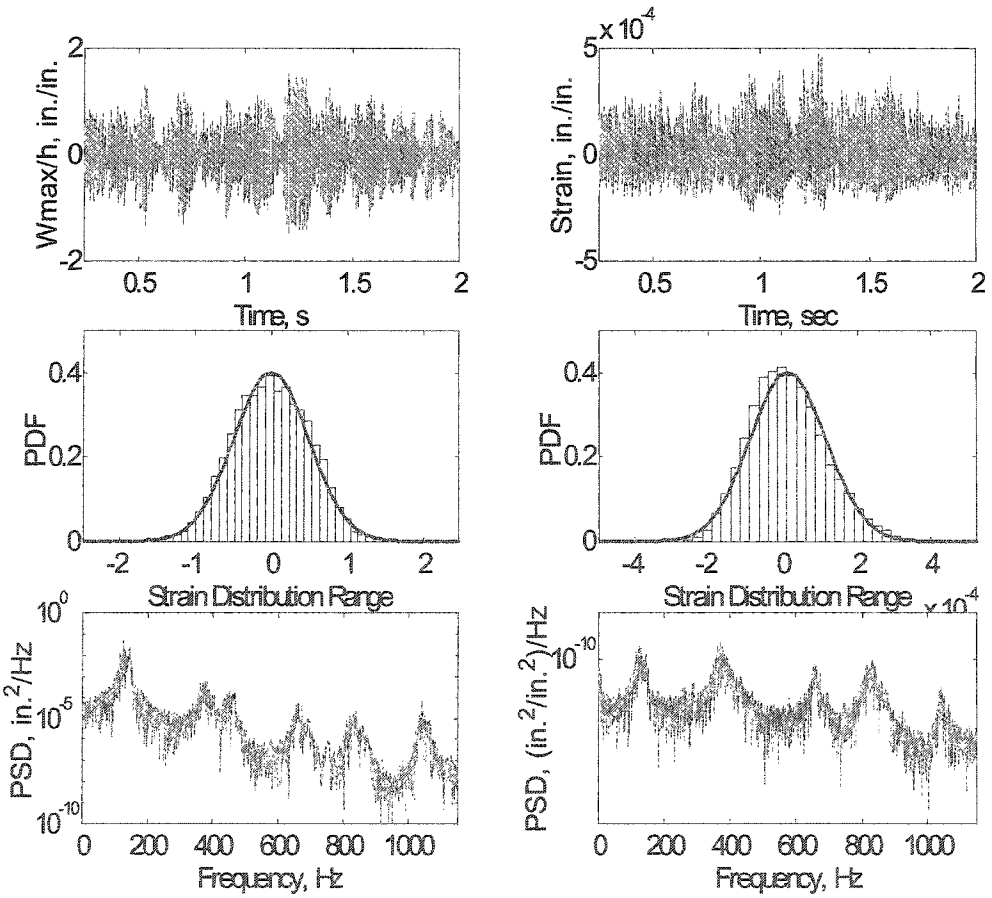

Fig. 7.3 Random response of a clamped traditional $[0/-45/45/90]_s$ composite plate at SPL = 110 dB and ΔT = 0°F.

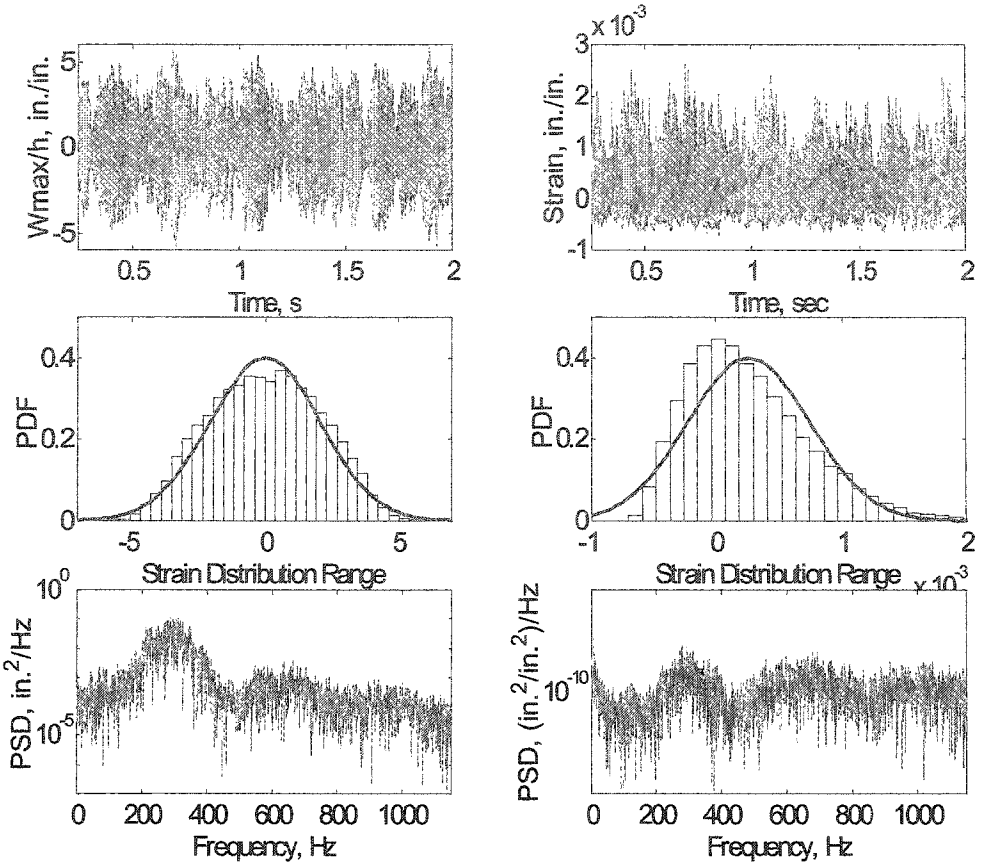

Fig. 7.4 Random response of a clamped traditional $[0/-45/45/90]_s$ composite plate at SPL = 130 dB and $\Delta T = 0°F$.

At combined acoustic and thermal loads, the panel responses indicate that there exist three distinct types of motion: (i) small deflection random vibration about one of the two buckled equilibrium positions (BEPs) as shown in Fig. 7.5, (ii) snap-through or oil-canning phenomenon between the two BEPs as shown in Fig. 7.6, and (iii) large amplitude nonlinear random vibration covering both BEPs shown in Fig. 7.7. At low 90 dB SPL and $\Delta T = 160°F$ ($\Delta T/\Delta T_{cr} = 4.07$), the time histories in Fig. 7.5 show clearly the linear random responses about one BEP: $(W_{max}/h)_{\Delta T} = -2.02$. The deflection PSD plot shows the domination of the fundamental mode, and the strain PSD plot shows the large

contribution from the fifth mode (1,5). Note the identified six modes are corresponding to panel vibration frequencies shown in Fig. 7.1 at $\Delta T = 160°F$. At moderate 110 dB SPL and $\Delta T = 120°F$ ($\Delta T/\Delta T_{cr} = 3.05$), the deflection time histories and PDF in Fig. 7.6 show a very clear snap-through motion and the deflection PDF shows highly non-Gaussian distribution. The six modes are also roughly identified. At high 130 dB SPL and $\Delta T = 160°F$ ($\Delta T/\Delta T_{cr} = 4.07$), shown in Fig. 7.7, the large deflection RMS W_{max}/h is 2.18 which covers both BEPs of $(W_{max}/h)_{\Delta T} = \pm 2.02$. All the six modes are smeared and can't be identified. Nonlinearity is further observed due to the broadening and shifting of the peaks in the PSD plots.

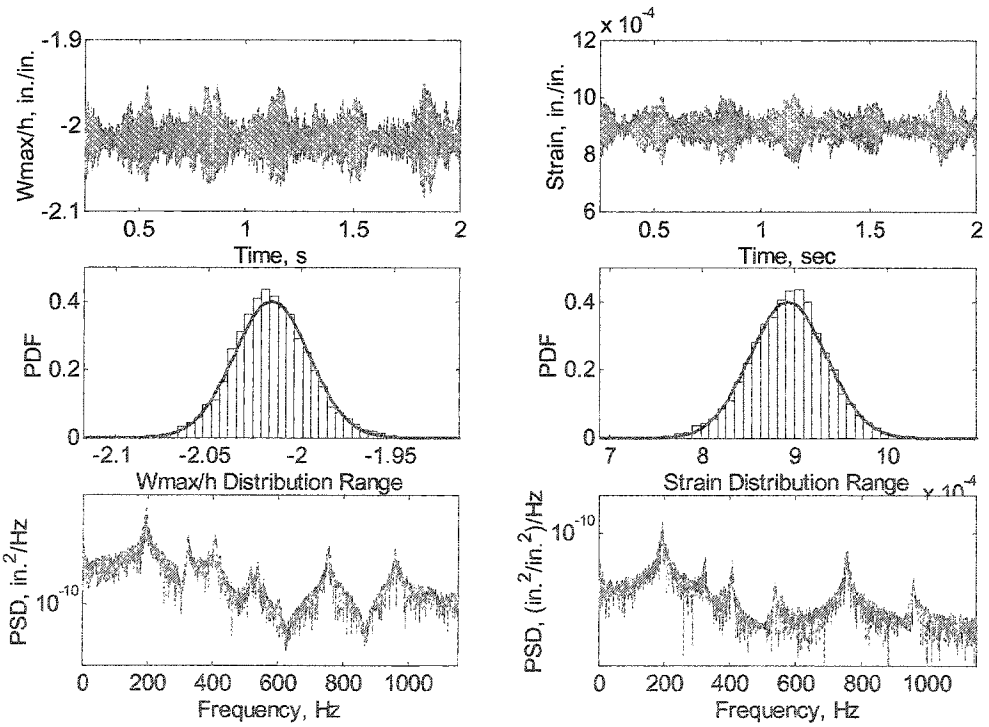

Fig. 7.5 Random response of a clamped traditional $[0/-45/45/90]_s$ composite plate at SPL = 90 dB and $\Delta T = 160°F$.

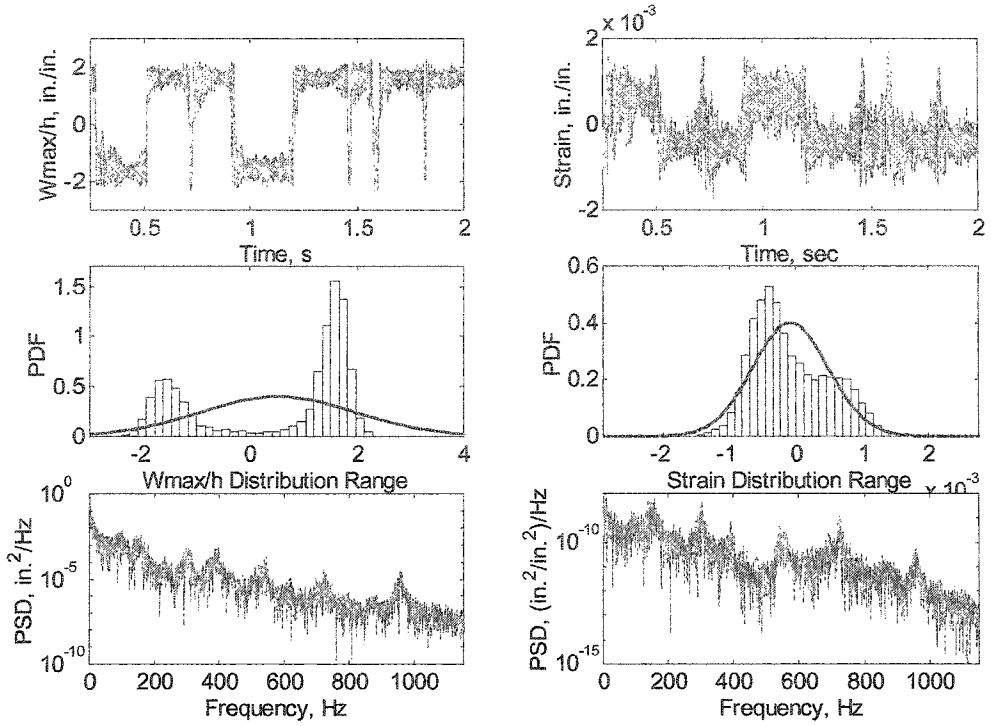

Fig. 7.6 Random response of a clamped traditional $[0/-45/45/90]_s$ composite plate at SPL = 110 dB and $\Delta T = 120°F$.

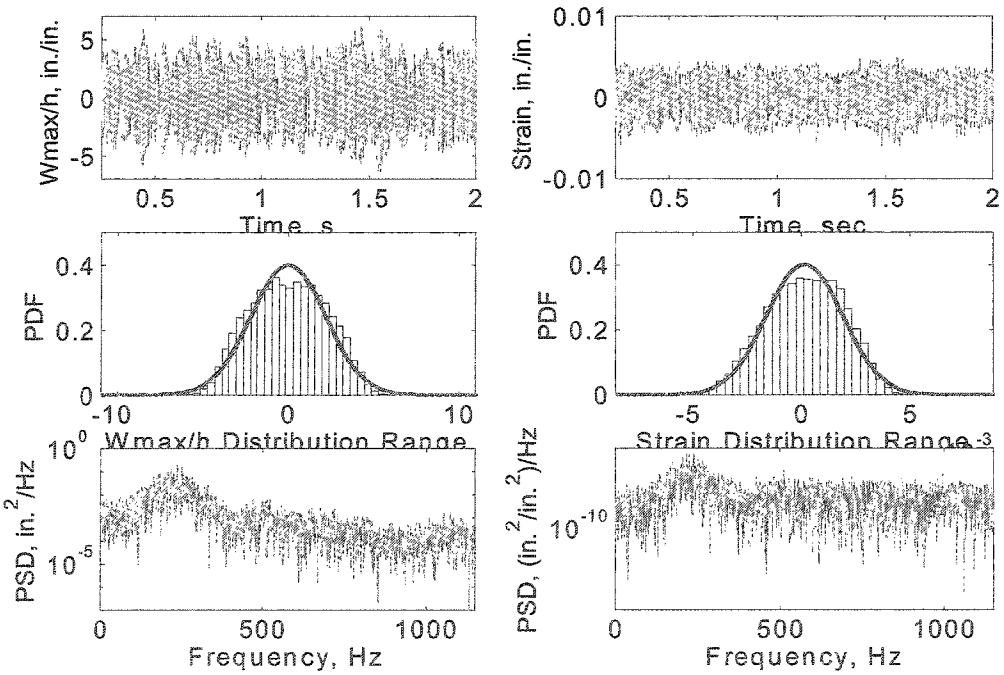

Fig. 7.7 Random response of a clamped traditional $[0/-45/45/90]_s$ composite plate at SPL = 130 dB and $\Delta T = 160°F$.

It is quite interesting to see what would happen at $\Delta T = 39.3°F$ ($\Delta T/\Delta T_{cr} = 1.0$) because the fundamental frequency at this temperature is zero theoretically. Figure 7.8 shows that the first mode is identified very close to zero under a small SPL = 90 dB acoustic load. The plate becomes very flexible at this temperature: RMS $W_{max}/h = 0.186$, which is much large than RMS $W_{max}/h = 0.0598$ at SPL = 90 dB and $\Delta T = 0°F$.

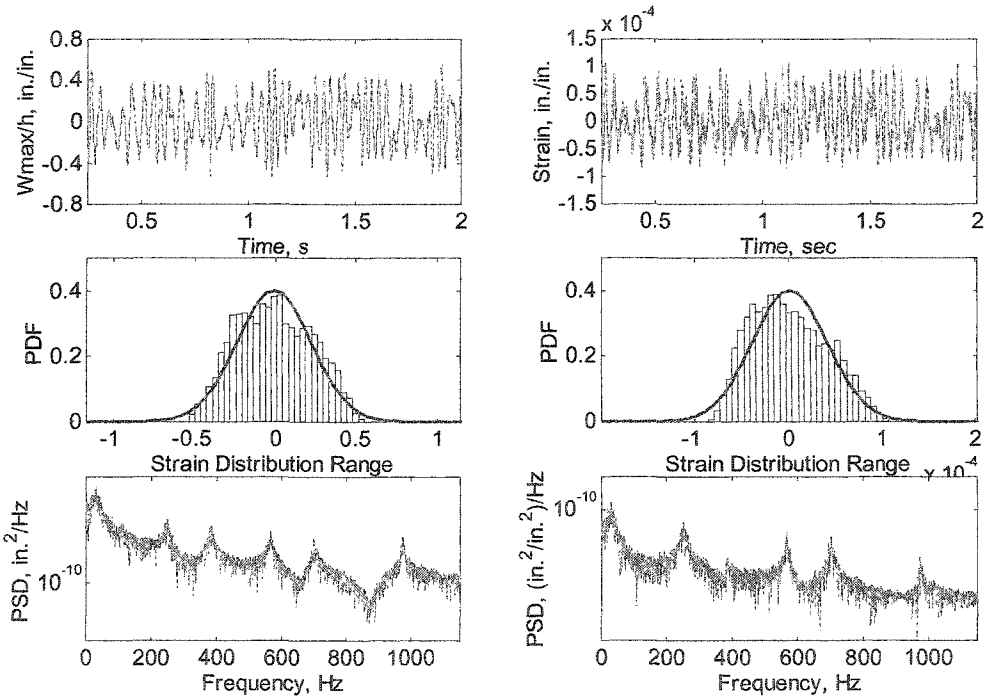

Fig. 7.8 Random response of a clamped traditional composite plate at SPL = 90 dB and $\Delta T = 39.3°F$.

What is the relation between RMS W_{max}/h and the two loading parameters: ΔT and SPL? Figure 7.9 plots RMS W_{max}/h versus ΔT and SPL, respectively. It is seen that when SPL is low, e.g. 90 dB, RMS W_{max}/h increases very fast with the increase of ΔT. Since W_{max}/h is actually the combination of static thermal deflection and dynamic

random vibration, the thermal static deflection is dominant at low SPLs and the dynamic response is the small random vibration about one of the two BEP's. At low SPLs it is also seen that RMS W_{max}/h decreases at high temperatures, but increases at low temperatures. It is known that thermally buckled panel would have asymmetric amplitudes, which will be more severe at high temperatures. It is the asymmetric amplitudes whose deflection is close to zero and thus is reason for the RMS to decrease at high temperatures. Figure 7.9 also shows that RMS W_{max}/h at different temperatures are close to each other for SPL = 130 dB. Although the plate is much stiffened as temperature increases, when snap-through or large random vibration over two BEP's occur, the compressive in-plane force induced by both the thermal effect is also very large. The compressive in-plane force tends to reduce the stiffness. The interaction of stiffening and softening leads to a temperature-irrelevant response at high SPLs.

7.2 SMAHC Plates

Two configurations of the SMAHC plates are studied here: (v_s = 10% and ε_r = 3%) and (v_s = 10% and ε_r = 5%). The natural frequencies of the SMAHC plates are different from the traditional $[0/-45/45/90]_s$ composite plate and thus should be investigated again. Figures 7.10 and 7.11 show the frequencies of the lowest 8 symmetric natural modes versus temperature for the two plates, respectively. It is decided that the same cut-off frequency 2048 Hz for both plates is high enough to cover the shifted frequency due to nonlinear large deflection. Repeat the previous procedures, six-mode solution was found giving converged RMS deflection and thus used; a quarter plate model with a 10×10 mesh and time step of 1/16384 sec is used as before.

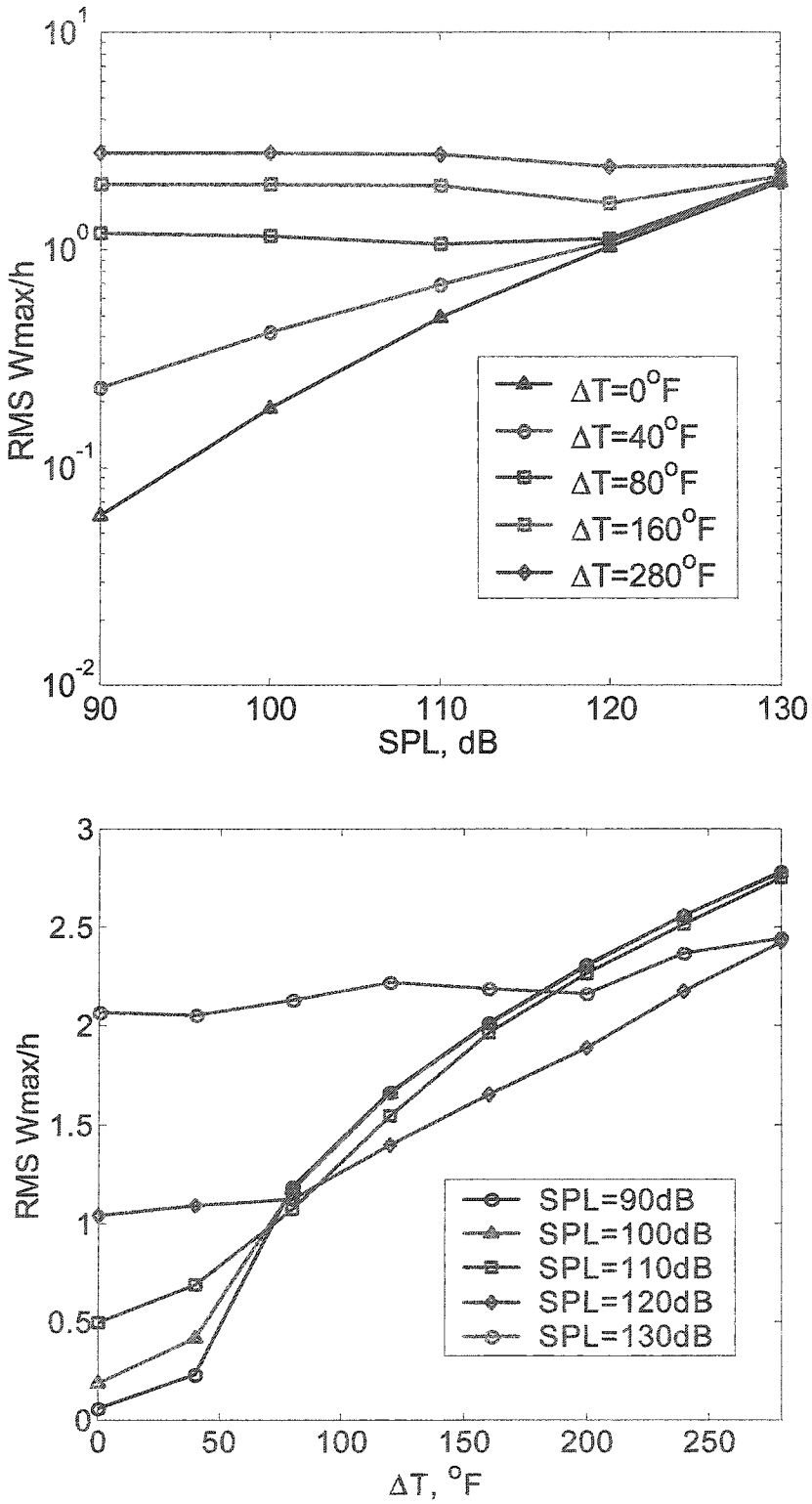

Fig. 7.9 Random response W_{max}/h versus temperature and sound pressure level of a clamped traditional $[0/-45/45/90]_s$ composite plate.

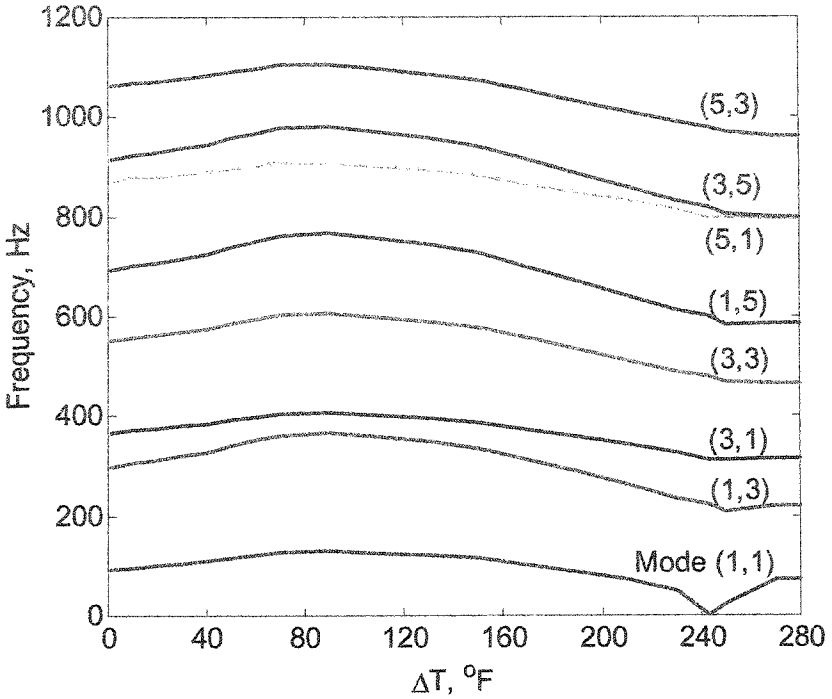

Fig. 7.10 Frequencies of the lowest 8 symmetric modes versus temperature for an SMAHC plate with $v_s = 10\%$ and $\varepsilon_r = 3\%$.

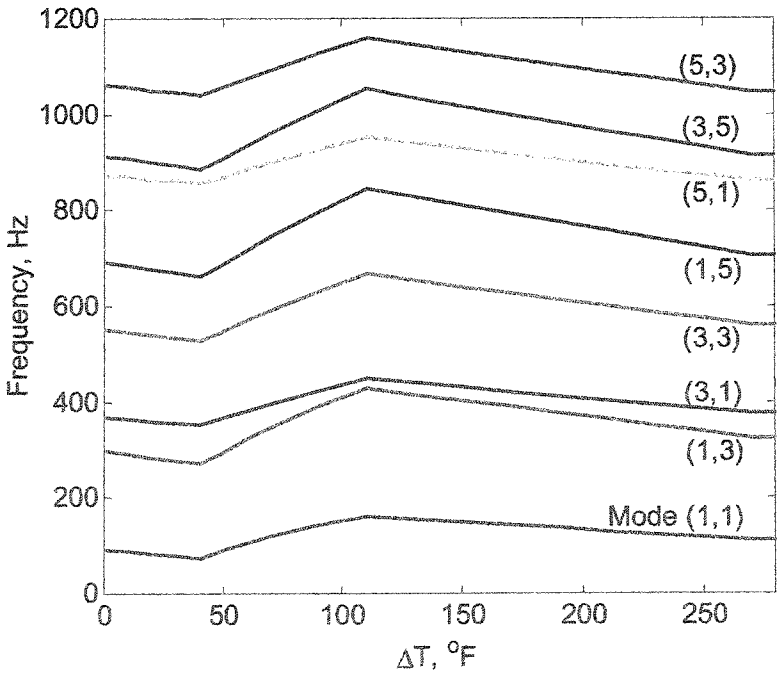

Fig. 7.11 Frequencies of the lowest 8 symmetric modes versus temperature for an SMAHC plate with $v_s = 10\%$ and $\varepsilon_r = 5\%$.

Figures 7.12 and 7.13 plot RMS W_{max}/h versus ΔT and SPL for the SMAHC plates with (v_s = 10% and ε_r = 3%) and (v_s = 10% and ε_r = 5%), respectively. It is found that at low and medium SPLs, the random response is almost temperature-irrelevant with a flat curve in the plot of RMS W_{max}/h versus ΔT, which is due to tuning of natural frequencies and delaying of critical buckling temperatures for the SMAHC plates.

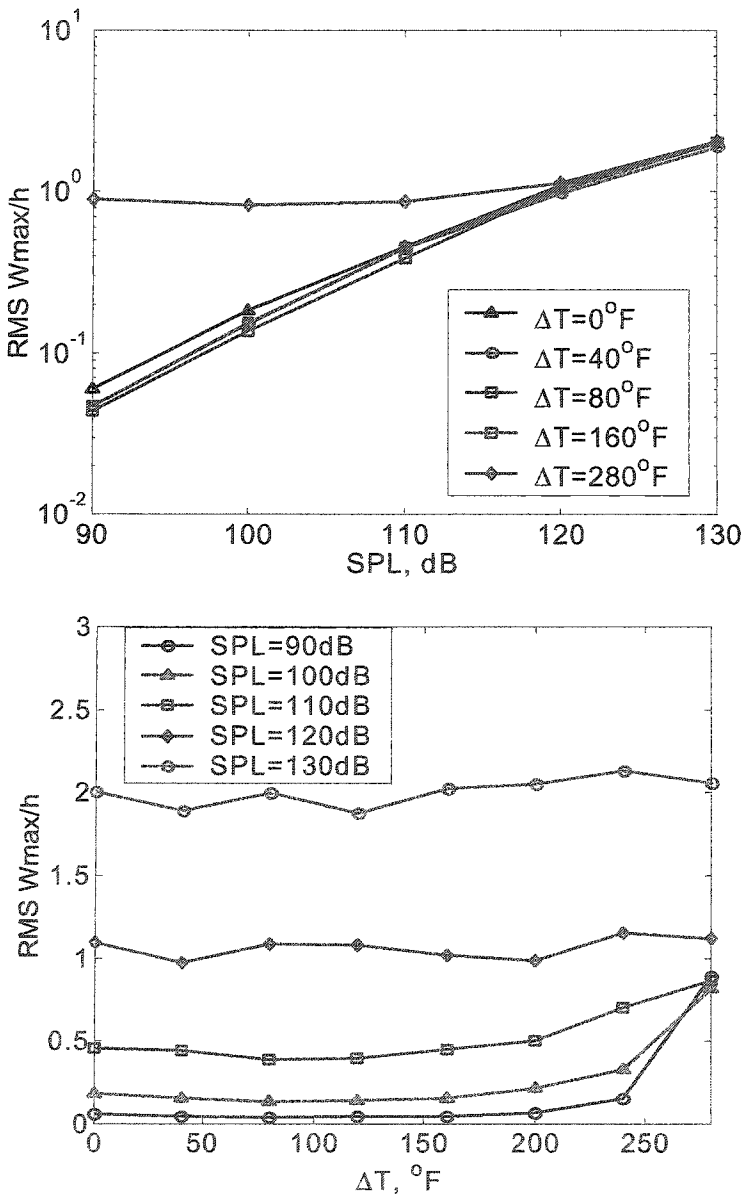

Fig. 7.12 Random response Wmax/h versus temperature and sound pressure level for an SMAHC plate with v_s = 10% and ε_r = 3%.

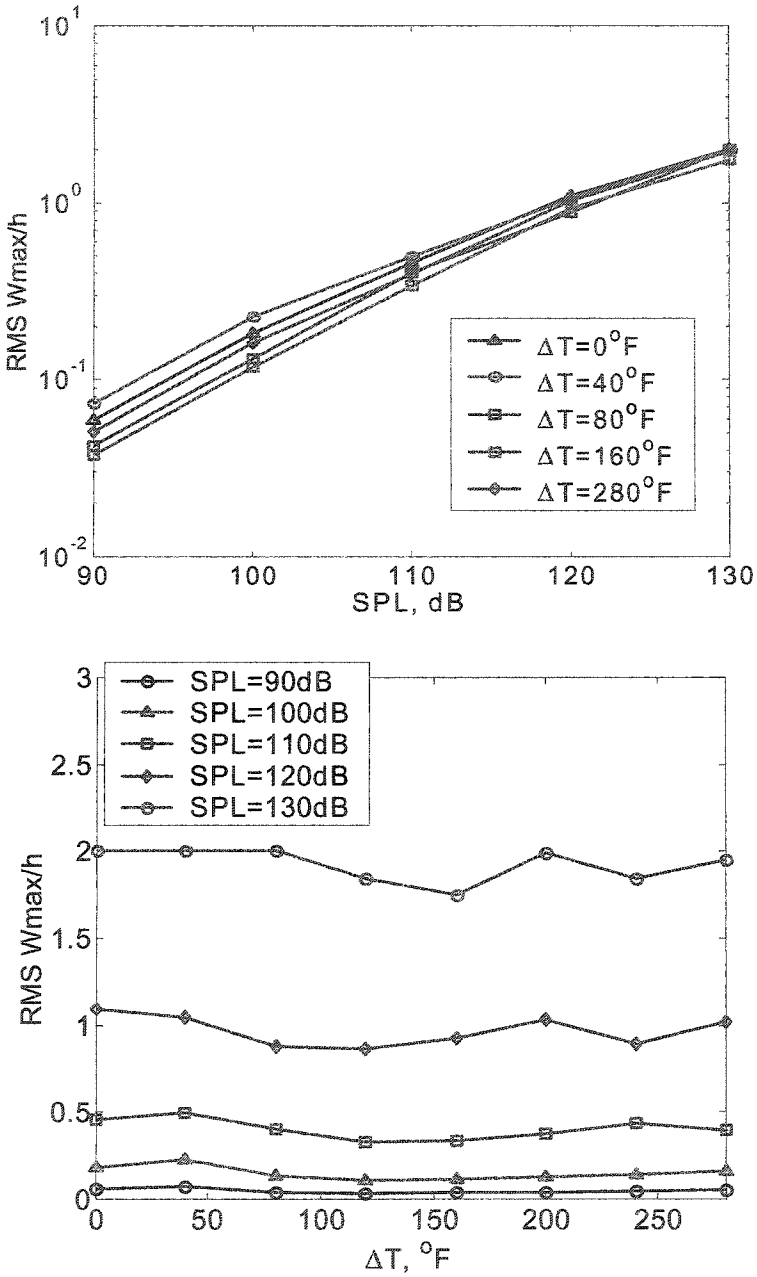

Fig. 7.13 Random response W_{max}/h versus temperature and sound pressure level for an SMAHC plate with $v_s = 10\%$ and $\varepsilon_r = 5\%$.

At low and medium SPLs, e.g. SPL = 110 dB, as shown in Fig. 7.14, RMS W_{max}/h of SMAHC plates turns out to be very small as temperature goes up as compared with the traditional $[0/-45/45/90]_s$ composite plate. This is because the thermal buckling is

suppressed partly (for v_s = 10% and ε_r = 3%) or completely (for v_s = 10% and ε_r = 5%). Compared with the traditional composite plate at high SPL, e.g. SPL = 130dB, as shown in Fig. 7.15, RMS W_{max}/h do not show that much differences. This is because the contribution of the acoustic load at high SPLs becomes dominated, and natural frequencies of the SMAHC or traditional composite plates are almost same, as shown in Figs. 7.1, 7.10 and 7.11.

The conclusion is therefore that, at low and medium SPLs, the SMAHC plates can reduce the RMS W_{max}/h greatly due to suppressing of the thermal buckling and tuning of the natural frequencies. It is also found that SMAHC plates can only reduce RMS W_{max}/h slightly at high SPLs, e.g. SPL = 130 dB, whereas the dominant factor is large random vibration. Increasing volume fraction or prestrain will not contribute much in controlling large random vibrations under combined acoustic and thermal loads.

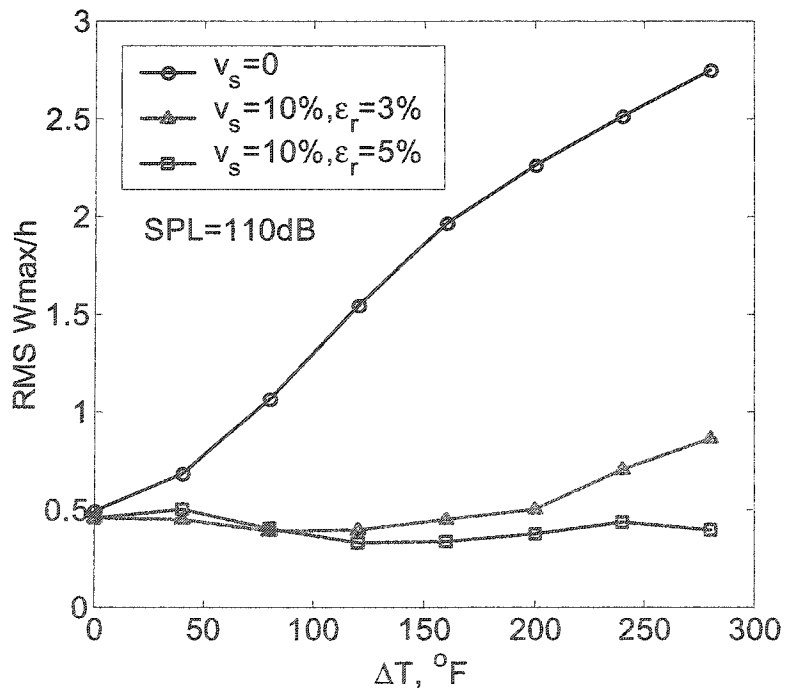

Fig. 7.14 Random response W_{max}/h versus temperature for traditional $[0/-45/45/90]_s$ composite and SMAHC plates at SPL = 110 dB.

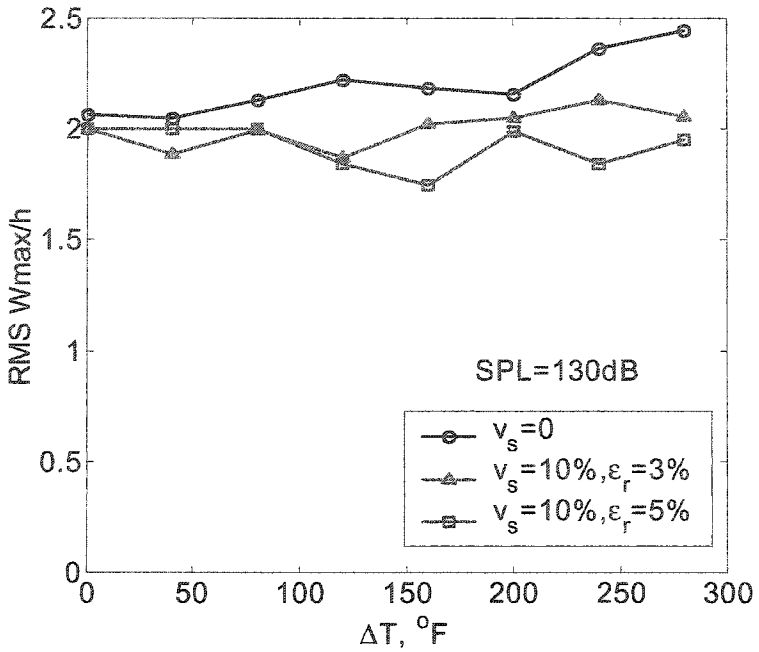

Fig. 7.15 Random response W_{max}/h versus temperature for traditional $[0/-45/45/90]_s$ composite and SMAHC plates at SPL = 130 dB.

CHAPTER VIII PANEL RESPONSE UNDER COMBINED THERMAL, AERODYNAMIC AND ACOUSTIC LOADS

The plate's dynamic behavior is investigated with three combined aerodynamic, acoustic and thermal loads, and the results are presented and compared for the traditional $[0/-45/45/90]_s$ composite and the SMAHC plates. The system dynamic equation of motion in modal coordinates can be rewritten as

$$[\overline{M}_b]\{\ddot{q}\}+[\overline{G}]\{\dot{q}\}+2[\zeta_i\omega_i][\overline{M}_b]\{\dot{q}\}+\left([\overline{K}]+[\overline{K}_q]+[\overline{K}_{qq}]\right)\{q\}=\{\overline{P}_c\} \tag{8.1}$$

where

$$([\overline{M}_b],[\overline{G}],[\overline{K}])=[\Phi_L]^T([M_b],[G],[K_{lin}])[\Phi] \tag{8.2}$$

$$[\overline{K}_q]=[\Phi_L]^T\sum_{r=1}^{n}q_r\left([K_{1NB}]^{(r)}-[K_{1Nm}]^{(r)}-[K_{1bm}]^{(r)}[K_m]^{-1}[K_{mb}]-[K_{bm}][K_m]^{-1}[K_{1mb}]^{(r)}\right)[\Phi] \tag{8.3}$$

$$[\overline{K}_{qq}]=[\Phi_L]^T\sum_{r=1}^{n}\sum_{s=1}^{n}q_rq_s\left([K_{2b}]^{(rs)}-[K_{2Nm}]^{(rs)}-[K_{1bm}]^{(r)}[K_m]^{-1}[K_{1mb}]^{(s)}\right)[\Phi] \tag{8.4}$$

$$\{\overline{P}_c\}=[\Phi_L]^T\left(\{P_t(t)\}+\{P_{\Delta Tb}\}-\{P_{rb}\}-[K_{bm}][K_m]^{-1}\{P_m\}\right) \tag{8.5}$$

and the matrix of AEMs $[\Phi]$ are obtained from

$$\omega_r^2[M_b]\{\phi_r\}=\left(\lambda_o[A_a]+[K_b]-[K_{bm}][K_m]^{-1}[K_{mb}]\right)\{\phi_r\} \tag{8.6}$$

The plate dynamic behaviors are investigated with four parameters in the study: ΔT, λ, Λ and SPL: ΔT varying from 0 – 280°F (T = 70 – 350°F), λ from 0 – 800, Λ from 0 – 45° and SPL from 90 – 130 dB. The full plate is modeled with a 12×12 mesh, or 144 BFS rectangular elements. The structural modal damping $\xi_r\omega_r = \xi_s\omega_s$ remains constant for all the modes with the fundamental damping coefficient ξ_1 equal to 0.02. The aerodynamic damping coefficient C_a is set to 0.1.

8.1 Traditional Composite Plates

The FE modal formulation based on AEMs is validated first as the follows. First, modal convergence is studied by utilizing concept of modal participations. The procedure starts with using more than enough number of modes with increasing frequencies for a typical case and checks their MP, and then retain those modes only with significant MP values. Table 8.1 gives MP values of 10 AEMs (λ_o = 530 at Λ = 0°) for a typical case: ΔT = 80°F, λ = 400, Λ = 0° and SPL = 130 dB. It can be seen that the MP values of the first six AEMs are all greater than 1% and they would be enough for a converged solution. Secondly, RMS W_{max}/h obtained using six AEMs of the lowest frequencies are compared with those using as many as 36 NMs for this typical case: ΔT = 80°F, λ = 400, Λ = 0°, as shown in Fig. 8.1. It is seen they agree very well. Therefore, six AEMs will yield accurate and converged response, and six AEMs will be used in all examples.

Table 8.1 MP of 10 AEMs for a clamped $[0/-45/45/90]_s$ composite plate at $\Delta T = 80°F$, $\lambda = 400$, $\Lambda = 0°$ and SPL = 130 dB

Modes #	1	2	3	4	5	6	7	8	9	10
MP (%)	48.0	40.4	4.69	1.47	1.46	2.14	0.81	0.25	0.27	0.49

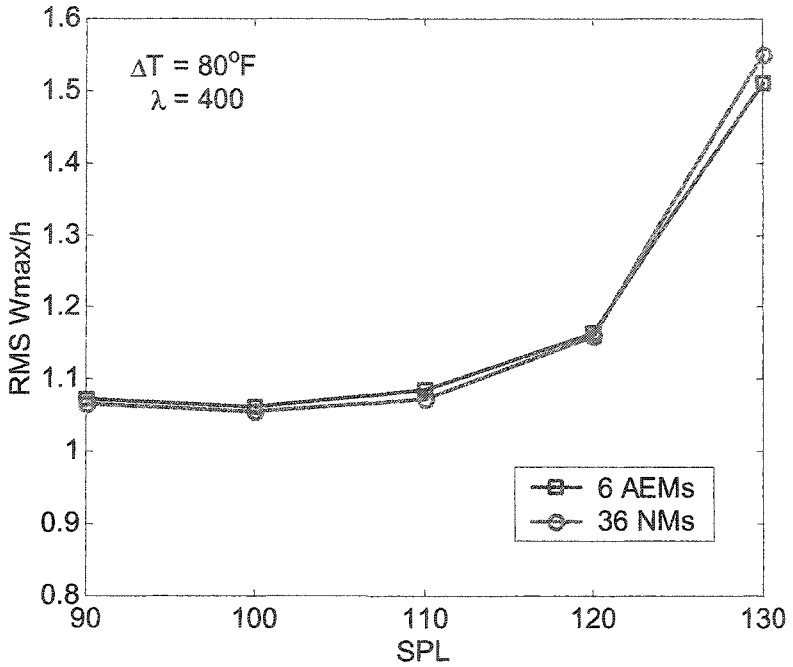

Fig. 8.1 Comparison of RMS W_{max}/h for a clamped traditional $[0/-45/45/90]_s$ composite plate at $\Delta T = 80°F$, $\lambda = 400$ and $\Lambda = 0°$ using 36 NMs and 6 AEMs, respectively.

Three types of plate behaviors can be observed for a traditional $[0/-45/45/90]_s$ composite plate: random vibration about the flat or buckled position, snap-through vibration, and large random vibration. The representative plot for each type are shown in Figs. 8.2 – 8.4 with time history, probability density function, and power spectrum density for the non-dimensional displacement W_{max}/h.

The time history, the Gaussian-like probability density, and first mode dominant PSD shown in Fig. 8.2 clearly indicate the small random vibration about the BEP (W_{max}/h

= 0.75) at $\Delta T = 60°F$, $\lambda = 100$, $\Lambda = 0°$ and SPL = 90 dB. The time history and PDF shown in Fig. 8.3 give a snap-through image at $\Delta T = 80°F$, $\lambda = 100$, $\Lambda = 0°$ and SPL = 110 dB. In Fig. 8.4, the time history, the peak's broadening and right-shifting demonstrate the large nonlinear random vibration at $\Delta T = 80°F$, $\lambda = 100$, $\Lambda = 0°$ and SPL = 130 dB.

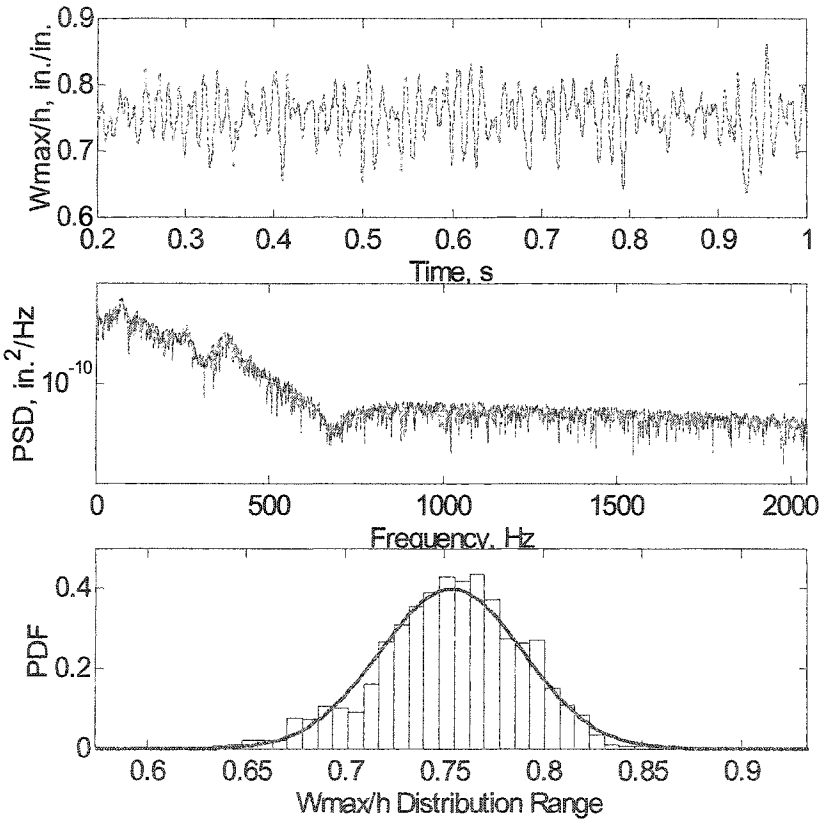

Fig. 8.2 Response of a clamped traditional $[0/-45/45/90]_s$ composite plate at $\Delta T = 60°F$, $\lambda = 100$, $\Lambda = 0°$ and SPL = 90 dB.

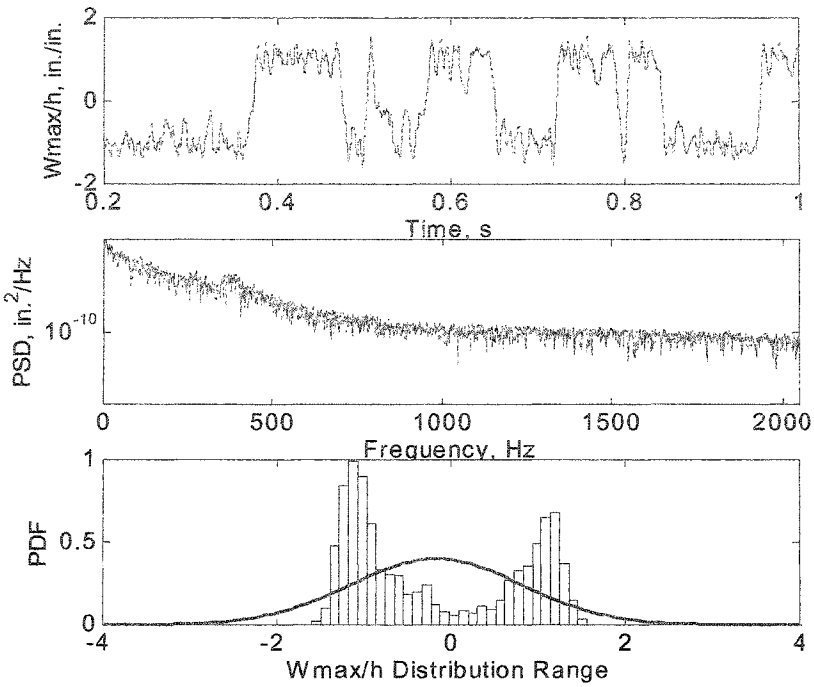

Fig. 8.3 Response of a clamped traditional $[0/-45/45/90]_s$ composite plate at $\Delta T = 80°F$, $\lambda = 100$, $\Lambda = 0°$ and SPL = 110 dB.

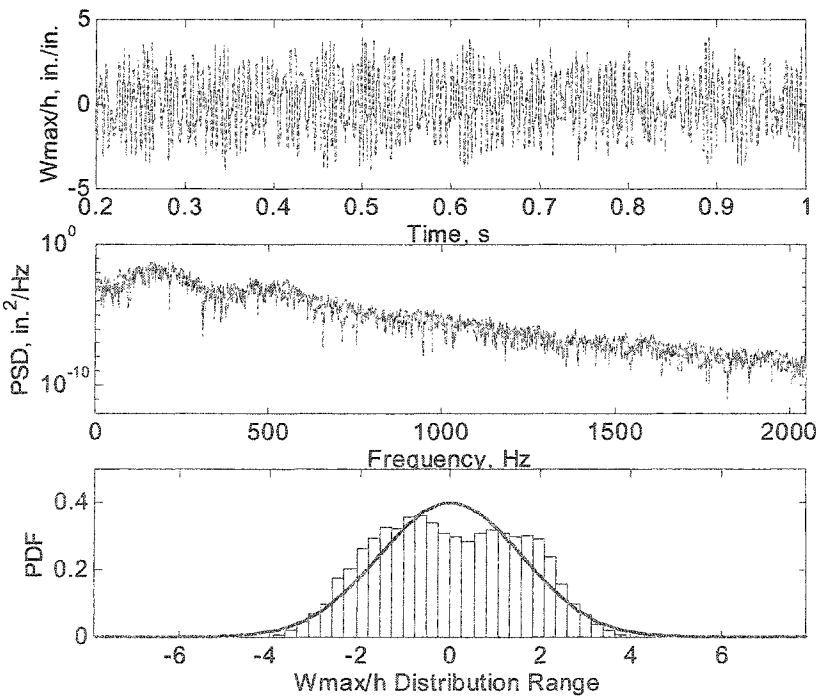

Fig. 8.4 Response of a clamped traditional $[0/-45/45/90]_s$ composite plate at $\Delta T = 80°F$, $\lambda = 100$, $\Lambda = 0°$ and SPL = 130 dB.

RMS W_{max}/h versus dynamic pressure λ at $\Lambda = 0°$ are shown in Fig. 8.5 with a set of plots at different temperatures. One can see that at $\Delta T = 0°F$, the figure shows that RMS W_{max}/h decreases first and then increases as λ goes up. This because at low dynamic pressure, the plate is stiffened due to the influence of airflow, and the plate is more like a pure random response. At high dynamic pressure, however, the flutter begins to occur and contributes to the total RMS W_{max}/h. One also sees that at low SPLs range, e.g. SPL $\leq$ 110 dB, RMS W_{max}/h nearly coincides with each other at very large dynamic pressure, because the flutter response is the dominant factor and the total response is in nature highly nonlinear.

As temperature increases, it is seen that thermal effect plays an important role in the total response from Fig. 8.5. Generally speaking, RMS W_{max}/h goes much larger at high temperatures. RMS W_{max}/h at $\Delta T = 200°F$ is much higher than that at $\Delta T = 80°F$ because the thermal buckling effects are accounted for. Another trend is that the spaces between the curves at various SPLs are getting closer and closer at high temperatures, especially for the lower two figures of $\Delta T = 200°F$ and 280°F in Fig. 8.5. It is also seen that RMS W_{max}/h drops sharply at some points such as $\Delta T = 200°F$, λ = 600 and 700, and SPL = 100 and 110 dB. Analyzing the time history shows that snap-through occurs, which lower the values of RMS W_{max}/h.

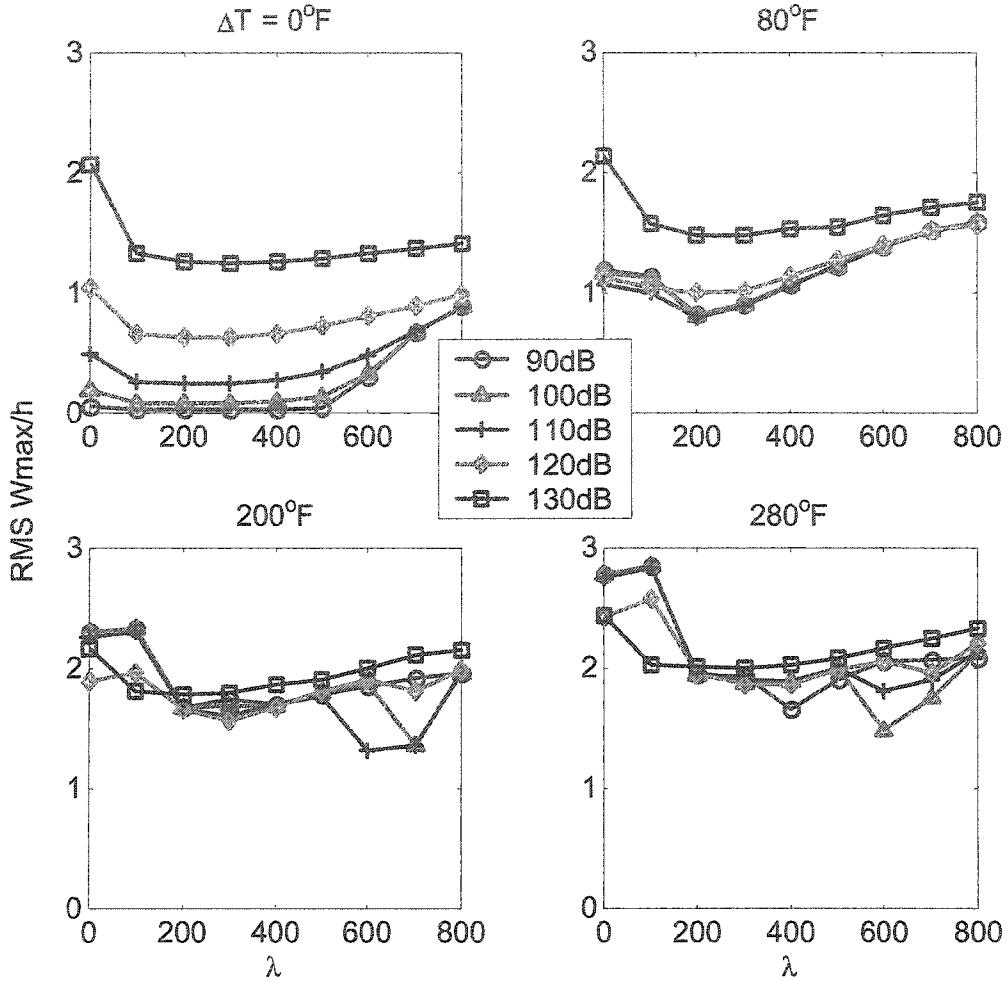

Fig. 8.5 RMS W_{max}/h versus λ of a clamped $[0/-45/45/90]_s$ composite plate at $\Lambda = 0°$.

It is seen that the response at $\Lambda = 45°$ as shown in Fig. 8.6 is very similar to that at $\Lambda = 0°$, although it is found before that the plate has a lower critical dynamic pressure λ_{cr} at $\Lambda = 45°$ than that at $\Lambda = 0°$.

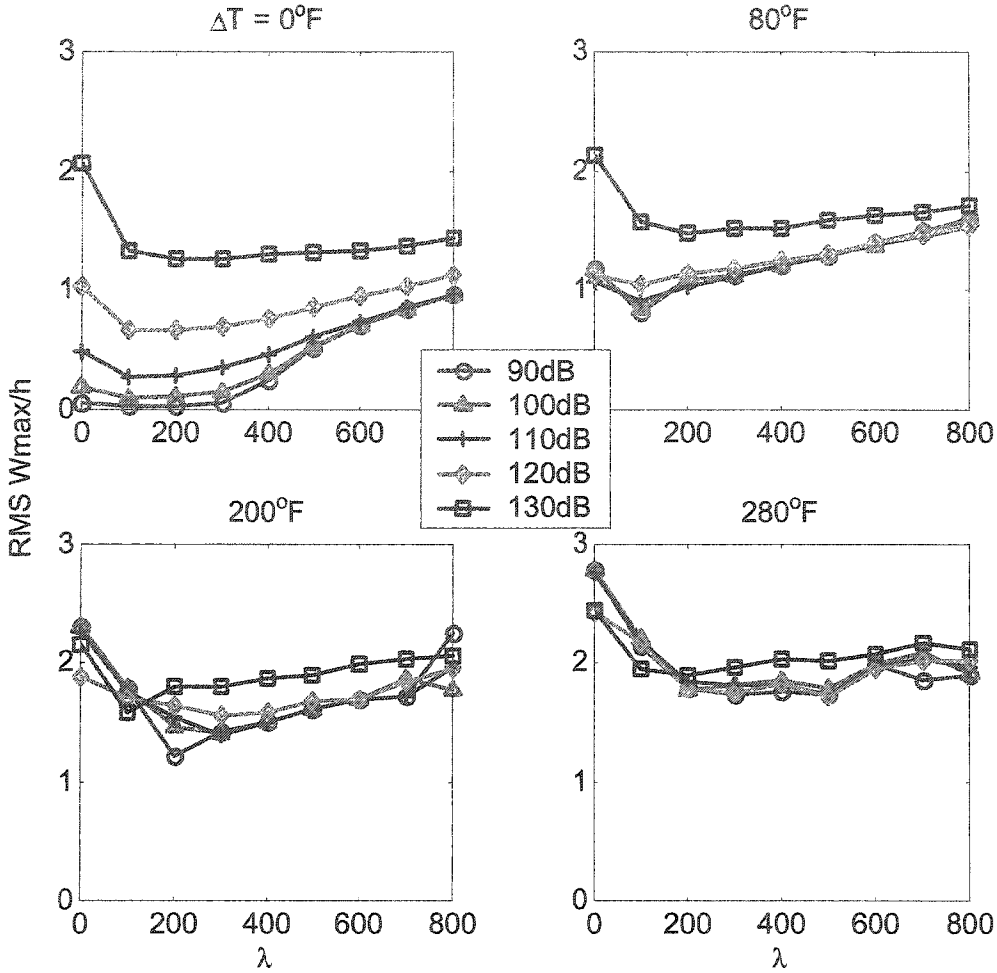

Fig. 8.6 RMS W_{max}/h versus λ for a clamped $[0/-45/45/90]_s$ composite plate at $\Lambda = 45°$.

8.2 SMAHC Plates

The SMAHC plates are investigated with three configurations: (v_s = 10% and ε_r = 3%), (v_s = 10% and ε_r = 5%) and (v_s = 15% and ε_r = 3%). The first configuration is for low volume fraction and small prestrain, whereas the second increases the prestrain, and the third increases only the volume fraction. Six AEMs are still used (λ_o = 510 at Λ = 0°). The responses for the configurations (v_s = 10% and ε_r = 3%) and (v_s = 10% and ε_r = 5%) at $\Lambda = 0°$ are shown in Figs. 8.7 and 8.8, respectively. The third configuration (v_s =

15% and ε_r = 5%) has similar results with the first two and thus it is not be plotted to avoid repetition.

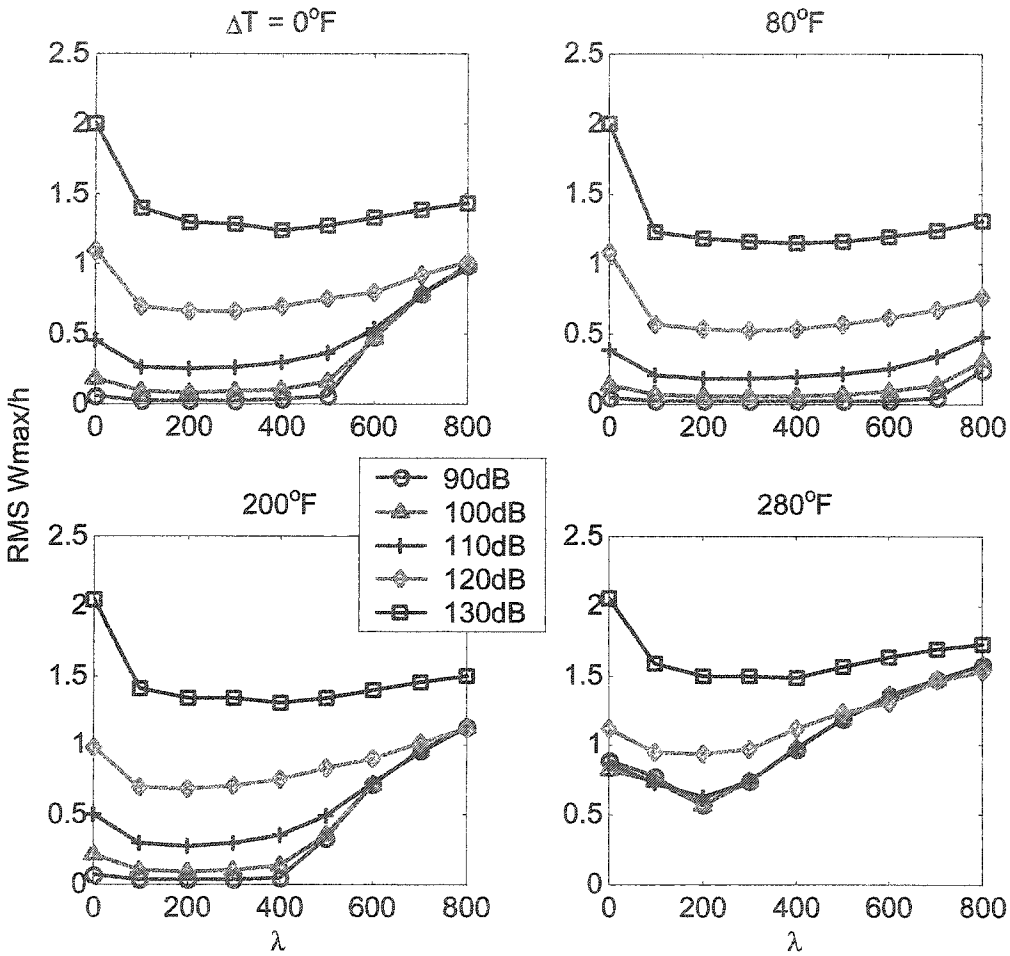

Fig. 8.7 RMS W_{max}/h versus λ for a clamped SMAHC plate (v_s = 10% and ε_r = 3%) at Λ = 0°.

For the SMAHC plate with (v_s = 10% and ε_r = 3%), as shown in Fig. 8.7, it is seen that RMS W_{max}/h was reduced greatly for most of the temperature range, especially at low SPLs, as compared with the traditional composite plate shown in Fig. 8.5. This is because the plate is more stiffened, and thermal buckling is eliminated as temperature

goes up until a quite high value. At $\Delta T = 200°F$, the response is almost the same with that at $\Delta T = 0°F$. This shows the ability of SMA to keep the stiffness within a given temperature range. At $\Delta T = 280°F$, the plate is buckled and the response at low SPLs becomes larger. But it is seen RMS W_{max}/h at SPL = 130 dB and $\lambda = 0$ is 2.0, which is still lower than 2.7 for the traditional composite plate.

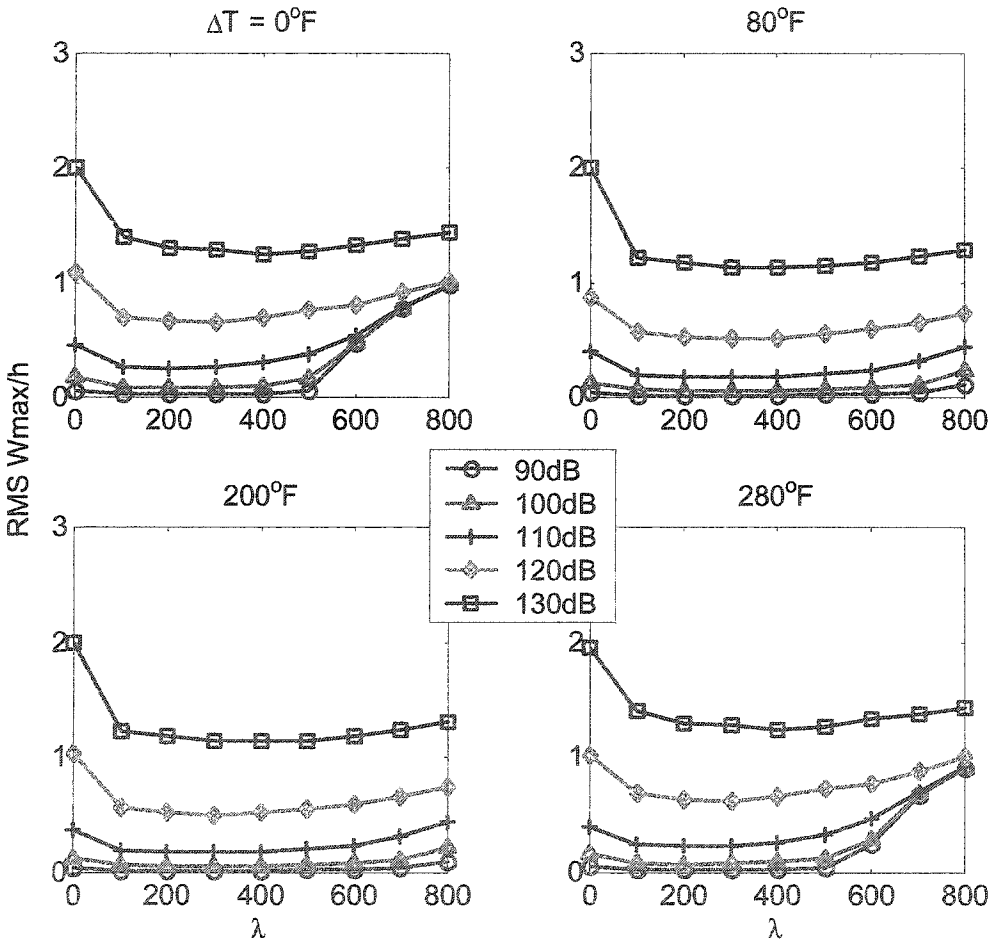

Fig. 8.8 RMS W_{max}/h versus λ for a clamped SMAHC plate ($v_s = 10\%$ and $\varepsilon_r = 5\%$) at $\Lambda = 0°$.

We can control the response of the SMAHC plates further by increasing either the prestrain or the volume fraction. For the second configuration (v_s = 10% and ε_r = 5%), as shown in Fig. 8.8, the response is decreased for the whole temperature range. The part of response that is flutter dominant was suppressed at some medium temperatures, e.g. ΔT = 80°F and ΔT = 200°F. It is also found that the thermal buckling is removed for the temperature range considered, which certainly benefits the control of the response. The results obtained show that the SMAHC plates have the ability to keep the dynamic responses irrelevant of temperature for a wide temperature range.

The comparisons of SMAHC plates with the traditional composite plate at SPL = 110 dB and 130 dB are shown in Figs. 8.9 and 8.10, respectively. It is seen that at low and medium SPLs, e.g. SPL = 110 dB in Fig. 8.9, the responses of the SMAHC plates are much lower than the traditional composite plate. In another words, SMA can reduce the response under three combined loads effectively and greatly. However, at high SPLs, e.g. SPL = 130 dB as shown in Fig. 8.10, the capability of SMA deteriorates although their responses are still lower than the traditional composite plate. This is because the recovery stress of SMA at high temperature saturates gradually and could not keep increasing. There are also some limitations for the volume fraction and prestrain of SMAHC, because of delamination and fatigue life considerations. The responses for the SMAHC plates at Λ = 45° are also investigated and compared with the traditional composite plate at Λ = 45°, similar conclusions could be drawn as above mentioned.

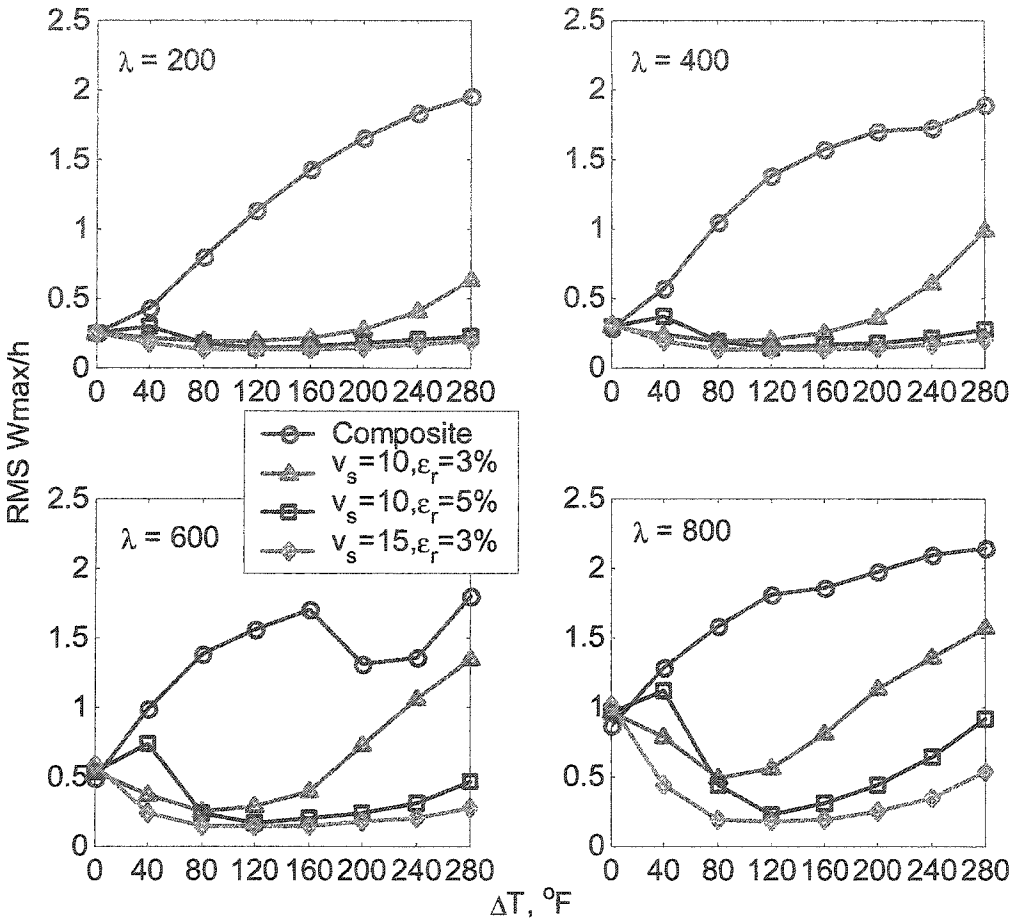

Fig. 8.9 Comparison of RMS W_{max}/h between a traditional composite $[0/-45/45/90]_s$ plate and the clamped SMAHC plates at SPL = 110 dB.

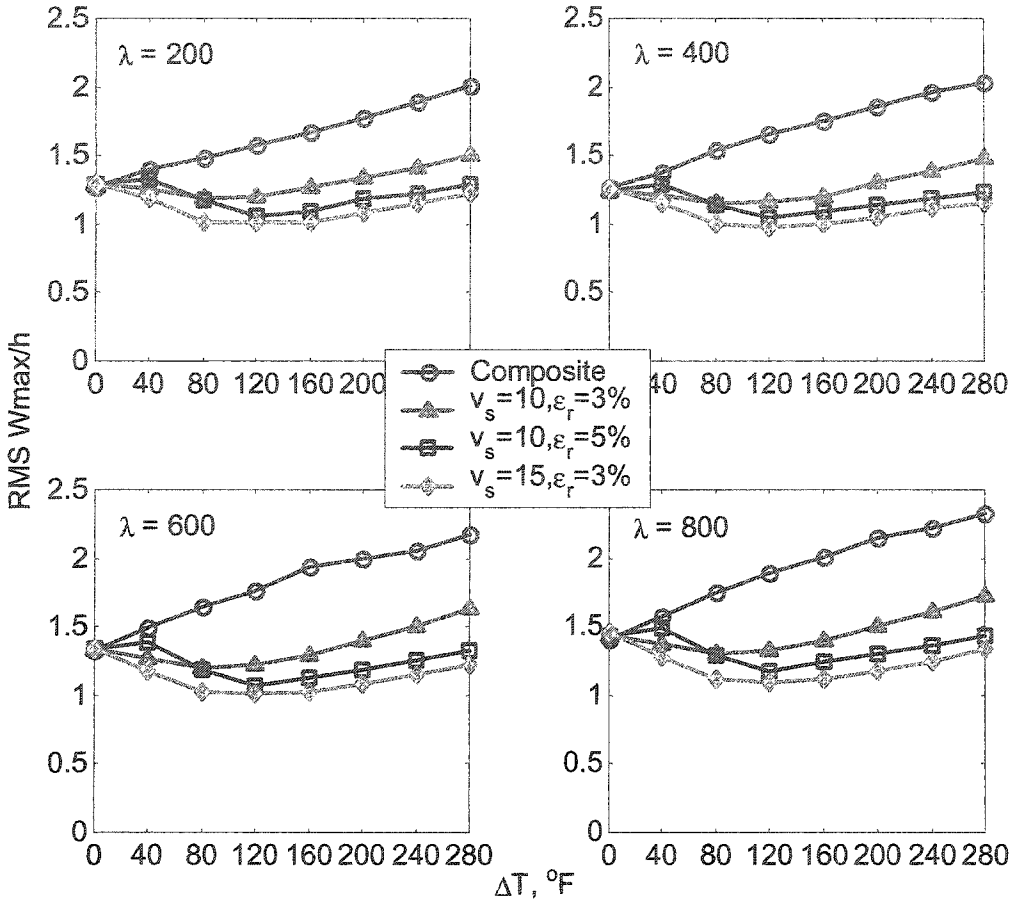

Fig. 8.10 Comparison of RMS W_{max}/h between a traditional composite $[0/-45/45/90]_s$ plate and the clamped SMAHC plates at SPL = 130 dB.

CHAPTER IX CONCLUSIONS

This dissertation research studies the static and dynamic behavior of traditional composite plates and SMAHC plates subjected to the combined thermal, aerodynamic and random acoustic loadings. The investigations include five categories: thermal buckling, aerothermal buckling, nonlinear panel flutter at elevated temperatures, random vibration under thermal effect, and flutter-random response under combined thermal, aerodynamic and acoustic loads. The TD material properties of composite matrix and SMA fibers are considered and employed into the formulation. The static response is determined using Newton-Raphson iterative scheme. The dynamic behavior is investigated numerically by time domain method. The finite element modal formulations and solution procedures are developed for time domain method. Two types of modes, i.e., normal modes and aeroelastic modes, are introduced to transform the system dynamic equations into modal coordinates. Numerical integration is employed to determine the displacement response time history, and Monte Carlo simulation method is used to determine the statistical parameters of random response.

Thermal buckling and postbuckling of a traditional composite plate and SMAHC plates are investigated first. The results show that the critical buckling temperature of the plate is greatly increased and thus thermal postbuckling deflection is greatly reduced for

the given temperature range. The shifting and crossings of the natural frequencies with temperature are also presented for the SMAHC plates with various configurations of SMA volume fraction v_s and prestrain ε_r.

Aerothermal deflections can be determined using same Newton-Raphson iterative scheme for the case before the flutter happens. The aerothermal deflection shapes is asymmetric due to the disturbance of airflow for traditional composite plates or SMAHC plates. It is also found that convergence could not be achieved when the combinations of temperature and dynamic pressure are close to the dynamic region.

Nonlinear panel flutter responses at elevated temperatures of traditional composite plates and SMAHC plates are investigated. The stability regions of a clamped traditional composite plate are studied. Four types of plate behaviors are found: flat and statically stable, buckled but dynamically stable, LCO and chaos. The plate's dynamic behaviors, besides generally defined LCO and chaotic motion, can be further cataloged in more detail as four types: nearly simple harmonic LCO, periodic LCO, non-periodic oscillation and chaotic oscillation. The finite element modal formulation that employs aeroelastic modes can reduce the number of modes greatly. The results also show that the LCO is very likely to evolve into chaos at combinations of moderate dynamic pressure and moderate or high temperatures. At higher dynamic pressure, with the increase of temperature, the motion is much likely to evolve from simple harmonic or periodic motion to non-periodic or chaotic motion. The SMAHC plates with various configurations of volume fractions and prestrains displayed their advantages: the increase of critical dynamic pressure, enlargement of static flat and stable region, and decrease of all the other regions, i.e. buckled, LCO and chaotic regions.

Random responses at elevated temperatures of a traditional composite plate and the SMAHC plates are investigated. Time domain numerical simulation is employed using finite element modal equations in normal modes. Three types of vibration can be identified in simulation results: linear small random vibration about one of two buckled equilibrium positions, snap-through, and large nonlinear random vibration over both buckled equilibrium positions. The RMS values of displacement responses are studied and compared for a traditional composite plate and SMAHC plates.

The responses under the combined aerodynamic, acoustic and thermal loads for a traditional composite plate and the SMAHC plates are also investigated. The aeroelastic modes are used to greatly reduce the number of modes used in the nonlinear modal equations. The RMS values of displacement responses of a traditional composite plate in temperature-dynamic pressure-SPL domain are studied. The results show that the airflow has the tendency to stiffen the plate when $\lambda < \lambda_{cr}$, and thus RMS (W_{max}/h) reduces with the increase of dynamic pressure. In postbuckling region, at certain dynamic pressure with the increase of temperature, the vibration motion is likely starting from vibration oscillation about the flat position then evolving to snap-through to vibration about one buckled position; while at certain temperature and with increasing dynamic pressure, the evolution of the vibration motion is reversed. At $\lambda = \lambda_{cr}$, panel flutter motion gradually becomes dominant with the increasing dynamic pressure. Compared with traditional composite plates, SMAHC plates are found to be able to reduce RMS values and prompt the evolution of vibration about buckled position and snap-through to vibration on flat position.

Further additional studies need to be carried out continuously. First, the experiments are needed to verify the analytical results, although it would be a difficult task. Second, all the above studies was for flat plates only. The finite element procedures need to be extended to imperfect plates, shallow shells and other structures. Third, for supersonic environments, high-temperature composite materials need to be studied and selected as the matrix for SMAHC. Last, the SMA fatigue analysis and service life estimation should be studied because of thermal cyclic load for the SMAHC plates.

REFERENCES

1. Vaicaitis, R., "Generalized Random Forces for Rectangular Panels," AIAA Journal, Vol. 11, No. 7, 1973, pp. 984-988.

2. Dowell, E. H., "Aeroelasticity of Plates and Shells," Noordhoff International Publishing, The Netherlands, 1975.

3. Bueher, W. J., and Wang, F. E., "A Summary of Recent Research on the Nitinol Alloys and Their Potential Application in Ocean Engineering," Ocean Engineering, Vol. 1, 1967, pp. 105-120.

4. Cross, W. B., Kariotis, A. H., and Stimler, F. J., "Nitinol Characterization Study," NASA CR-1433, (Goodyear Aerospace Corp. Report No. Ger 14188, Akron, OH), 1970.

5. Rogers, C. A., Liang, C., and Barker, D. K., "Dynamic Control Concepts Using Shape Memory Alloy Reinforced Plates," Smart Material Structures and Mathematical Issues, Technomic Publishing Co., Lancaster, PA, 1989, pp. 3962.

6. Thornton, E. A., "Thermal Buckling of Plates and Shells," Applied Mechanics Reviews, Vol. 46, No. 10, 1993, pp. 485-506.

7. Chia, C. Y., "Geometrically Nonlinear Behavior of Composite Plates: A Review," Applied Mechanics Reviews, Vol. 41, No. 12, 1988, pp. 439-451.

8. Hilburger, M., Waas, A., and Starnes, J., "Modeling the Dynamic Response and Establishing Postbuckling/Post Snap-Thru Equilibrium of Discrete Structures via a Transient Analysis," Journal of Applied Mechanics, Vol. 64, 1997, pp. 590-595.

9. Irschik, H., "Large Thermoelastic Deflections and Stability of Simply Supported Polygonal Panels," Acta Mechanica, Vol. 59, No. 1, 1986, pp. 31-46.

10. Birman, V., and Bert, C. W., "Buckling and Postbuckling of Composite Plates and Shells Subjected to Elevated Temperature," Journal of Applied Mechanics, Vol. 60, 1993, pp. 514-519.

11. Noor, A. K., and Peters, J. M., "Postbuckling of Multilayered Composite Plates Subjected to Combined Axial and Thermal Loads," Thermal Structures and Material for High-Speed Flight, Progress in Astronautics and Aeronautics, Vol. 140, 1992, pp. 183-203.

12. Noor, A. K., and Burton, W. S., "Computational Models for High Temperature Multilayered Composite Plates and Shells," Applied Mechanics Reviews, Vol. 45, No. 10, 1993, pp. 419-446.

13. Kamiya, N., and Fukui, A., "Finite Deflection and Postbuckling Behavior of Heated Rectangular Plates with Temperature-Dependent Properties," Nuclear Engineering and Design, Vol. 72, 1982, pp. 415-420.

14. Chen, L. W., and Chen, L. Y., "Thermal Buckling Behavior of Laminated Composite Plates with Temperature-Dependent Properties," Composite Structures, Vol. 13, No. 4, 1989, pp. 275-287.

15. Chen, L. W., and Chen, L. Y., "Thermal Postbuckling Behavior of Laminated Composite Plates with Temperature-Dependent Properties," Composite Structures, Vol. 19, No. 3, 1991, pp. 267-283.

16. Noor, A. K., and Burton, W. S., "Three-Dimensional Solutions for the Thermal Buckling and Sensitivity Derivatives of Temperature-Sensitive Multilayered Angle-Ply Plates," Journal of Applied Mechanics, Vol. 59, 1992, pp. 848-856.

17. Lee, I. K., and Lee, D. M., "Vibration and Flutter Analysis of Stiffened Composite Plate Considering Thermal Effect," Proceeding of the ASME Aerospace Division, International Mechanical Engineering Congress, Dallas, TX, AD-Vol. 55, 1997, pp. 133-141.

18. Lee, J. J., and Choi, S., "Thermal Buckling and Postbuckling Analysis of a Laminated Composite Beam with Embedded SMA Actuators," Composite Structures, Vol. 47, No. 1-4, December 1999, pp. 695-703.

19. Lee, H. J., Lee, J. J., and Huh, J. S., "A Simulation Study on the Thermal Buckling Behavior of Laminated Composite Shells with Embedded Shape Memory Alloy (SMA) Wires," Composite Structures, Vol. 47, No. 1-4, December 1999, pp. 463-469.

20. Thompson, S. P., and Loughlan, J., "Enhancing the Postbuckling Response of a Composite Panel Structure Utilizing Shape Memory Alloy Actuators – a Smart Structural Concept," *Composite Structures*, Vol. 51, No. 1, January 2001, pp. 21-36.

21. Zhong, Z. W., "Reduction of Thermal Deflection and Random Response of Composite Structures with Embedded Shape Memory Alloy at Elevated Temperature," Ph.D. Dissertation, Old Dominion University, Norfolk, VA, 1998.

22. Mei, C., Duan, B., and Zhong, Z. W., "Large Thermal Deflections of Composite Plates with Temperature Dependent Properties," AFWL-VA-WP-TR-1999-3036, Wright-Patterson AFB, OH. Feb. 1999.

23. Duan, B., Tawfik, M., Goek, S. N., Ro, J. J., and Mei, C., "Analysis and Control of Large Thermal Deflection of Composite Plates Using Shape Memory Alloy," SPIE 7th Annual International Symposium on Smart Structures and Materials, Newport Beach, CA, March 2000. No. 3991-45.

24. Gary, C. E. Jr., and Mei, C., "Large Amplitude Finite Element Flutter Analysis of Composite Panels in Hypersonic Flow," AIAA Journal, Vol. 31, No. 6, 1993, pp. 1090-1099.

25. Mei, C., Abdel-Motagaly, K., and Chen, R., "Review of Nonlinear Panel Flutter at Supersonic and Hypersonic Speeds," Applied Mechanics Reviews, Vol. 52, No. 10, 1999, pp. 321-332.

26. Cheng, G., "Finite Element Modal Formulation for Panel Flutter at Hypersonic Speeds and Elevated Temperatures," Old Dominion University, Norfolk, VA, December, 2002.

27. Dowell, E. H., "Nonlinear Oscillation of a Fluttering Plate I," AIAA Journal, Vol. 4, No. 7, 1966, pp. 1267-1275.

28. Dowell, E. H., "Nonlinear Oscillation of a Fluttering Plate II," AIAA Journal, Vol. 5, No. 5, 1967, pp. 1856-1862.

29. Ye, W. L., and Dowell, E. H., "Limit Cycle Oscillation of a Fluttering Cantilever Plate," AIAA Journal, Vol. 29, No. 11, 1991, pp. 1929-1936.

30. Kuo, C. C., Morino, L., and Dugundji, J., "Perturbation and Harmonic Balance Methods for the Nonlinear Panel Flutter," AIAA Journal, Vol. 10, No. 10, 1972, pp. 1479-1484.

31. Yuen, S., and Lau, S., "Effect of In-Plane Load on Nonlinear Panel Flutter by Incremental Harmonic Balance Method," AIAA Journal, Vol. 29, No. 9, 1991, pp. 1472-1479.

32. Eastep, F., and McIntoch, S. Jr., "Analysis of Nonlinear Panel Flutter and Response under Random Excitation or Nonlinear Aerodynamic Loading," AIAA Journal, Vol. 9, No. 3, 1971, pp. 411-418.

33. Morino, L., "A Perturbation Method for Treating Nonlinear Panel Flutter Problems," AIAA Journal, Vol. 7, No. 3, 1969, pp. 405-410.

34. Olson, M. D., "Finite Element Approach to Panel Flutter," AIAA Journal, Vol. 5, No. 2, 1967, pp. 226-227.

35. Olson, M. D., "Some Flutter Solutions using Finite Element," AIAA Journal, Vol. 8, No. 4, 1970, pp. 747-752.

36. Liaw, D. G., and Yang, T. Y., 'Reliability and Nonlinear Supersonic Flutter of Uncertain Laminated Plates," AIAA Journal, Vol. 31, No. 12, 1993, pp. 2304-2311.

37. Han, A. D., and Yang, T. Y., "Nonlinear Panel Flutter using High Order Triangular Finite Element," AIAA Journal, Vol. 21, No. 5, 1983, pp. 1453-1461.

38. Dixon, I. R., and Mei, C., "Finite Element Analysis of Large Amplitude Panel flutter of Thin Laminates," AIAA Journal, Vol. 31, No. 4, 1993, pp. 701-707.

39. Gray, C. E. Jr., "Large Amplitude Finite Element Flutter Analysis of Composite Panels in Hypersonic Flow," Ph.D. Dissertation, Old Dominion University, Norfolk, VA, 1991.

40. Xue, D. Y., "A Finite Element Frequency Domain Solution of Nonlinear Panel Flutter with Temperature Effects and Fatigue Life Analysis," Ph.D. Dissertation, Old Dominion University, Norfolk, VA, 1991.

41. Abdel-Motagaly, K., Duan B., and Mei, C., "Nonlinear Response of Composite Panels under Combined Acoustic Excitation and Aerodynamic Pressure," 40th Structures, Structural Dynamics and Materials Conference, St Louis, MO, 1999, pp. 1963-1972. Also AIAA Journal, Vol. 38, No. 9, 2000, pp. 1534-1542.

42. Abdel-Motagaly, K., Chen, R. and Mei, C., "Nonlinear Flutter of Composite Panels Under Yawed Supersonic Flow Using Finite Elements," AIAA Journal, Vol. 37, No. 9, 1999, pp.1025-1032.

43. Friedmann, P., and Hanin, M., "Supersonic Nonlinear Flutter of Orthotropic or Isotropic Panels with Arbitrary Flow Direction," Israel Journal Technology, Vol. 6, No.1-2, 1968, pp. 46-57.

44. Chandiramani, N. K., Plaut, R.H., and Librescu, L., "Nonperiodic Flutter of a Buckled Composite Panel," Sadhana Journal, Vol. 20, Parts 2-4, April-August, 1995, pp. 671-689.

45. Chandiramani, N. K., Plaut, R.H., and Librescu, L., "Nonlinear Flutter of Buckled Shear-Deformable Composite Panel in a High Supersonic Flow," Journal Nonlinear Mechanics, Vol. 30, No.2, 1995, pp. 149-167.

46. Zhou, R. C., Mei, C., and Huang, J. K., "Suppression of Nonlinear Panel Flutter at Supersonic speeds and Elevated Temperatures," AIAA Journal, Vol. 34, No. 2, 1996, pp347-354.

47. Abdel-Motagaly, K., "Finite Element Analysis and Active Control for Nonlinear Flutter of Composite Panels Under Yawed supersonic Flow," Ph.D. Dissertation,

Department of Aerospace Engineering, Old Dominion University, Norfolk, VA, December 2001.

48. Guo, X., and Mei, C., "Using Aeroelastic Modes for Nonlinear Panel Flutter At Arbitrary Supersonic Yawed Angle," AIAA Journal, Vol. 41, No. 2, 2003, pp. 272-279.

49. Houbolt, J. C., "A Study of Several Aerothermoelastic Problems of Aircraft in High Speed Flight," Ph.D. Dissertation, Mitteilung aus dem Institute fur Flugzeugstatikund Leichtbau, ETH, Zurich, 1958.

50. Xue, D. Y., and Mei, C., "Finite Element Nonlinear Panel Flutter with Arbitrary Temperatures in Supersonic Flow," AIAA Journal, Vol. 31, No. 1, 1993, pp. 154-162.

51. Liaw, D. G., "Nonlinear Supersonic Flutter of Laminated Composite Plates under Thermal Load," Computers and Structures, Vol. 65, No. 5, 1997, pp. 733-740.

52. Zhou, R. C., "Finite Element Analysis for Nonlinear Flutter Suppression of Composite Panels at Elevated Temperatures using Piezoelectric Materials," Ph.D. Dissertation, Old Dominion University, Norfolk, VA, 1994.

53. Crandall, S., and Zhu, W., "Random Vibration: A Survey of Recent Development," Journal of Applied Mechanics, Vol. 50, No. 5, 1983, pp. 953-962.

54. Clarkson, B. L., "Review of Sonic Fatigue Technology," NASA CR-4587, 1994.

55. Wolfe, H. F., Shroger, C.A., Brown, D.L. and Simmons, L.W., "An Experimental Investigation of Nonlinear Behavior of Beams and Plates Excited to High Levels of Dynamic Response," WL-TR-96-3057, Wright-Patterson AFB, OH, 1995.

56. Istenes, R. R., Rizzi, S. A. and Wolfe, H. F., "Experimental Nonlinear Random Vibration Results of Thermally Buckled Composite panels," Proceedings of 36th Structures, Structural Dynamics, and Materials Conference, New Orleans, LA, April 1995, pp. 1559-1568.

57. Ng, C. F., and Clevenson, S. A., "High-Intensity Acoustic Tests of a Thermally Stressed Plate," *Journal of Aircraft*, Vol. 28, No. 4, 1991, pp. 275-281.

58. Murphy, K. D., Virgin, L. N., and Rizzi, S. A., "Characterizing the Dynamic Response of a Thermally Loaded Acoustically Excited Plate," Journal of Sound and Vibration, Vol. 196, No. 5, 1996, pp. 635-658.

59. Gordon, R. W., Hollkamp, J. J., Spottswood, S. M., "Nonlinear Response of a Clamped Beam to Random Base Excitation", 8th International Conference on Recent Advances in Structural Dynamics, Southampton, UK, July 2003 (CDROM).

60. Iwan, W. D., and Yang, M. I., "Application of Statistical Linearization Techniques to Nonlinear Multi-Degree of Freedom Systems," Journal of Applied Mechanics, Vol. 39, 1972, pp. 545-550.

61. Bolotin, V. V., Random Vibration of Elastic Systems, Martinus Nijhoff Publishers, 1984, pp. 290-292.

62. Heuer, R., Irschik, H., and Ziegler, F., "Nonlinear Random Vibrations of Thermally Buckled Skew Plates," Probabilistic Engineering Mechanics, Vol. 8, No. 3-4, 1993, pp. 265-271.

63. Elishakoff, I., and Zhang, X., "An Appraisal of Different Stochastic Linearization Techniques," Journal of Sound and Vibration, Vol. 153, No. 2, 1992, pp. 370-375.

64. Roberts, J. B., and Spanos, P. D., "Random Vibration of Statistical Linearization," John Wiley & Sons, 1990.

65. Ng, C. F., "Nonlinear and Snap-Through Response of Curved Panels to Intense Acoustic Excitation," Journal of Aircraft, Vol. 26, No. 3, 1989, pp. 281-288.

66. Lee, J., "Large Amplitude Plate Vibration in an Elevated Thermal Environment," Applied Mechanics Reviews, Vol. 46, part 2, No. 11, 1993, pp. 242-254.

67. Locke, J., and Mei, C., "Finite Element, Large Deflection Random Response of Thermally Buckled Beams," AIAA Journal, Vol. 28, No. 12, 1990, pp. 2125-2131.

68. Mei, C., and Chen, R. R., "Finite Element Nonlinear Random Response of Composite Panels of Arbitrary Shape to Acoustic and Thermal Loads Applied Simultaneously," WL-TR-97-3085, Wright-Patterson AFB, OH, 1997.

69. Shinozuka, M., and Jan, D. M., "Digital Simulation of Random Processes and Its Applications," Journal of Sound and Vibration, Vol. 25, No. 1, 1972, pp. 111-128.

70. Shinozuka, M., and Wen, Y. K., "Monte Carlo Solution of Nonlinear Vibrations," AIAA Journal, Vol. 10, No. 1, 1972, pp. 37-40.

71. Arnold, R. R., and Vaicaitis, R., "Nonlinear Response and Fatigue of Surface Panels by the Time Domain Monte Carlo Approach," WRDC-TR-90-3081, Wright-Patterson AFB, OH, 1990.

72. Vaicaitis, R., "Recent Advances of Time Domain Approach for Nonlinear Response and Sonic Fatigue," Proceeding, 4th International Conference on Structural Dynamics, ISVR, 1991, pp. 84-103.

73. Green, P. D. and Killey, A., "Time Domain Dynamic Finite Element Modeling in Acoustic Fatigue Design," Proceedings 6th International Conference on Structural Dynamics, ISVR, 1997, pp. 1007-1026.

74. Robinson, J. H., "Finite Element Formulation and Numerical Simulation of the Large Deflection Random Vibration of Laminated Composite Plates," MS Thesis, Old Dominion University, Norfolk, VA, August 1990.

75. Dhainaut, J. M., Duan, B., Mei, C., Spottswood, S. M., and Wolfe, H. F., "Nonlinear Response of Composites Panels to Random Excitations at Elevated Temperatures," 7th International Conference on Recent Advances in Structural Dynamics, Southampton, England, July 2000, pp. 769-784.

76. Przekop, A., "Nonlinear Response and Fatigue Estimation of Aerospace Curved Surface Panels to Acoustic and Thermal Loads," Ph.D. Dissertation, Old Dominion University, Norfolk, VA, August 2003.

77. Duan B., "Suppression of Composite Panel Vibration Under Combined Aerodynamic and Acoustic Excitations at Elevated Temperatures Using Shape Memory Alloy," Ph.D. Dissertation, Old Dominion University, Norfolk, VA, May 2001.

78. Birman, V., "Review of Mechanics of Shape Memory Alloy Structures," Applied Mechanics Reviews, Vol. 50, part 1, No. 11, 1997, pp. 629-645.

79. Rogers, C. A., Liang, C., and Jia, J., "Behavior of Shape Memory Alloy Reinforced Composite Plates—Part I: Model Formulation and Control Concepts," Proceeding, 30th Structures, Structural Dynamics and Materials Conference, 1989, pp. 2011-2017.

80. Baz, A., and Tampe, L., "Active Control of Buckling of Flexible Beams," Proceeding, 8th Biennial Conference on Failure Prevention and Reliability, Montreal, Canada, 1989, ASME DE-Vol. 16, pp. 211-218.

81. Baz, A., Ro, J. J., Mutua, M., and Gilheany, J., "Active Control of Buckling of Nitinol-Reinforced Composite Beams," Proceeding, Active Materials and Adaptive Structures Conference, Arlington, VA, 1992, pp. 167-176.

82. Rogers, C. A., Liang, C., and Barker, D. K., "Dynamic Control Concept using Shape Memory Alloy Reinforced Plates," Smart Materials, Structures and Mathematical Issues, US Army Research Office Workshop, Blacksburg, VA, Sept. 15-16, 1988.

83. Rogers, C. A., Liang, C., and Fuller, C. R., "Modeling of Shape Memory Alloy Hybrid Composites for Structural Acoustic Control," Journal of Acoustic Society of America, Vol. 89, No. 1, 1991, pp. 210-220.

84. Duan, B., Tawfik, M., Ro, J. J., and Mei, C., "Vibration of Laminated Composite Plates Embedded with SMA at Elevated Temperatures," SPIE 7th Annual

International Symposium on Smart Structures and Materials, Newport Beach, CA, March 2000. No 3991-46.

85. Suzuki, S., and Degaki, T., "Supersonic Panel Flutter Suppression Using Shape Memory Alloy," International Journal of Intelligent Mechatronics: Design and Production, Vol. 3, No. 1, 1998, pp. 1-10.

86. Tawfik, M., Duan, B., Ro, J. J., and Mei, C., "Suppression of Postbuckling Deflection and Panel Flutter Using Shape Memory Alloy," SPIE 7th Annual International Symposium on Smart Structures and Materials, Newport Beach, CA, March 2000. No. 3991-44.

87. Turner, T. L., "Thermomechanical Response of Shape Memory Alloy Hybrid Composites," NASA/TM-2001-210656, Langley Research Center, January 2001.

88. Jones, R. M., *Mechanics of Composite Materials*, 2nd Edition, Taylor & Francis, 1999.

89. Bogner, F. K., Fox, R. L., and Schmit, L. A., "The Generation of Inter-Element Compatible Stiffness and Mass Matrices by the Use of Interpolation Formulas," *AFFDL-TR-66-80*, Wright-Patterson AFB, OH, 1966, pp. 396-443.

90. Meirovitch, L., *Fundamentals of Vibrations*, McGraw-Hill, New York, 2001, pp.346.

91. Barlow, J., "Optimal Stress Locations in Finite Element Models," *International Journal for Numerical Methods in Engineering*, Vol. 10, No. 2, 1976, pp. 243-251.

92. Cook, R. D., Malkus, D. S. and Plesha, M. E., *Concepts and Applications of Finite Element Analysis*, 3rd Edition, John Wiley, New York, 1989, pp. 189.

93. Dowell, E. H., "Observation and Evolution of Chaos for an Autonomous System," *Journal of Applied Mechanics*, Vol. 51, No. 3, 1984, pp. 664-673.

94. Cheng, G. F. and Mei, C., "Finite Element Modal Formulation for Hypersonic Panel Flutter Analysis with Thermal Effects," AIAA Journal, Vol. 42, No. 4, 2004, pp. 687-695.

95. Azzouz, M. S., Guo, X., Przekop, A., and Mei, C., "Comparison of PDE/Galekin and FEM for Nonlinear Aerospace Structure Analysis," AIAA 2003-1516, 44th Structures, Structural Dynamics, and Materials Conference, Norfolk, VA, April 2003.

96. Lutes, L.D. and Sarkani, S., "Stochastic Analysis of Structural and Mechanical Vibrations," Prentice Hall, Upper Saddle River, NJ, 1997, pp. 227-235.

CURRICULUM VITA

for

Xinyun Guo

DEGREES:

Doctor of Philosophy (Aerospace Engineering), Old Dominion University, Norfolk, Virginia, The United States of America, December 2004

Master of Science (Aerospace Engineering), Beijing Institute of Technology, Beijing, People's Republic of China, March 1995

Bachelor of Science (Mechanical Engineering), Beijing Institute of Technology, Beijing, People's Republic of China, July 1992

PROFESSIONAL CHRONOLOGY:

Department of Aerospace Engineering, Old Dominion University, Norfolk, Virginia
Research Assistant, August 2000 - December 2003

Beijing Electronic System Engineering Institute, Beijing, People's Republic of China
Aerospace Engineer, April 1995 - July 2000

SCIENTIFIC AND PROFESSIONAL SOCIETIES MEMBERSHIP:

AIAA Student Member

HONORS AND AWARDS:

"Excellent Young Engineer" Award, Beijing Electronic System Engineering Institute, Beijing, People's Republic of China, 1996, 1997 and 1999.

MAJOR SERVICE ACTIVITIES:

President of Chinese Student and Scholar Association (CSSA), Old Dominion University. Norfolk, Virginia, February 2001 - February 2002.

SCHOLARLY ACTIVITIES COMPLETED:

1. Guo, X., and Mei, C., "Using Aeroelastic Modes for Nonlinear Panel Flutter At Arbitrary Supersonic Yawed Angle," AIAA Journal, Vol. 41, No. 2, 2003, pp. 272-279.

2. Dhainault, J.-M., Guo, X., Mei, C., Spottswood, S. M. and Wolfe, H. F., "Nonlinear Response of Panels in an Elevated Thermal-Acoustic Environment," Journal of Aircraft, Vol. 40, No. 4, July-August 2003, pp. 683-691.

3. Guo, X., Przekop, A., Mei, C., and Lee, Y. Y., "Suppression of Thermal Buckling of Composite Surface Panels Using SMA for Supersonic Vehicles," To appear in Journal of Aircraft 2004.

4. Lee, Y. Y., Ng, C. F., and Guo, X., "Nonlinear Random Response of Cylindrical Panels to Acoustic Excitations Using Finite Element Modal Method," Nonlinear Dynamics, Vol. 31, No.3, February 2003, pp. 327-345.

5. Cheng, W. F., Lee, Y. Y., Ng, C. F., Cheng, G. F., and Guo, X., "An Application of a New Roadside Barrier to Traffic Noise Mitigation," JSME International Journal Series C, Vol. 46 (1), March 2003, pp. 155-160.

6. Lama, H.F., Lee, Y.Y., Sun, H.Y., Cheng, G.F., and Guo, X. "Application of the Spatial Wavelet Transform and Bayesian Approach to the Crack Detection of a Partially Obstructed Beam," Thin-Walled Structures, Vol. 43, November 2004.

7. Przekop, A., Azzouz, M. S., Guo, X., Mei, C., and Azrar, L., "Multimode Large Amplitude Free Vibration of Shallow Shells Considering Inplane Inertia," To appear in AIAA Journal.

8. Abdel-Motagaly, K., Guo, X., Duan, B., and Mei, C., "Active Control of Nonlinear Panel Flutter under Yawed Supersonic Flow," Accepted by AIAA Journal.

9. Duan, B., Guo, X., Abdel-Motagaly, K., and Mei, C., "Flutter and Thermal Deflection Suppression of Composite Plates by Embedded Shape Memory Alloy Fibers," submitted to AIAA Journal for review.

10. Guo, X., Mei, C., "Application of Aeroelastic Modes on Nonlinear Supersonic Panel Flutter at Elevated Temperatures," submitted to Computers and Structures for review.

11. Guo, X., Mei, C., "Aeroelastic Modes for Nonlinear Panel Flutter at Elevated Temperatures," CST2004-83, The Seventh International Conference on Computational Structures Technology, Lisbon, Portugal, September, 2004.

12. Guo, X., Przekop, A., Mei, C., "Nonlinear Random Response of Shallow Shells at Elevated Temperatures Using Finite Element Modal Method," AIAA 2004-1558, 45th Structures, Structural Dynamics, and Materials Conference, Palm Springs, CA, April 2004.

13. Guo, X., Przekop, A., Mei, C., "Reduction of Random Response of Composite Plates Using Shape Memory Alloy in Thermal Environments," AIAA 2004-1635, 45th Structures, Structural Dynamics, and Materials Conference, Palm Springs, CA, April 2004.

14. Przekop, A., Guo, X., Azzouz, S., Mei, C., "Reinvestigation of Nonlinear Random Response of Shallow Shells Using Finite Element Modal Formulation," AIAA 2004-1553, 45th Structures, Structural Dynamics, and Materials Conference, Palm Springs, CA, April 2004.

15. Przekop, A., S. Azzouz, Guo, X., Mei, C., "Nonlinear Stiffness Estimation for Modal Finite Element Approach to Free Vibrations of Shallow Shells," AIAA 2004-1615, 45th Structures, Structural Dynamics, and Materials Conference, Palm Springs, CA, April 2004.

16. Azzouz, M., Guo, X., Przekop, A., Mei, C., "Nonlinear Flutter of Cylindrical Shell Panels Under Yawed Supersonic Flow Using FE," AIAA 2004-2043, 45th Structures, Structural Dynamics, and Materials Conference, Palm Springs, CA, April 2004.

17. Guo, X., Przekop, A., Mei, C., and Lee, Y. Y., "Thermal Buckling Suppression of Composite Laminates Using SMA for Supersonic Vehicle Applications," WA-1-4, 5th International Congress on Thermal Stresses and Related Topics, Virginia Tech, Blacksburg, VA, June 2003.

18. Duan, B., Abdel-Motagaly, K., Guo, X., and Mei, C., "Suppression of Supersonic Panel Flutter and Thermal Deflection Using Shape Memory Alloy," AIAA 2003-1513, 44th Structures, Structural Dynamics, and Materials Conference, Norfolk, VA, April 2003.

19. Azzouz, M. S., Guo, X., Przekop, A., and Mei, C., "Comparison of PDE/Galekin and FEM for Nonlinear Aerospace Structure Analysis," AIAA 2003-1516, 44th Structures, Structural Dynamics, and Materials Conference, Norfolk, VA, April 2003.

20. Przekop, A., Guo, X., Azzouz, M. S., and Mei, C., "Nonlinear Responses and Fatigue of Curved Panels to Acoustic Excitation Using Finite Element," AIAA 2003-1710, 44th Structures, Structural Dynamics, and Materials Conference, Norfolk, VA, April 2003.

21. Przekop, A., Azzouz, M. S., Guo, X., Mei, C., and Azrar, L., "On Large Amplitude Free Vibration of Curved Panels Considering Inplane Inertia," AIAA 2003-1772, 44th Structures, Structural Dynamics, and Materials Conference, Norfolk, VA, April 2003.

22. Przekop, A., Guo, X., Azzouz, M. S., and Mei, C., "Large Amplitude Response of Shallow Shell Panels to Acoustic Excitations," Proceedings 8th International Conference on Structural Dynamics, ISVR, Southampton, UK, 2003.

23. Guo, X., and Mei, C., "Using Aeroelastic Modes for Nonlinear Panel Flutter At Arbitrary Supersonic Yawed Angle," AIAA 2002-1486, 43rd Structures, Structural Dynamics, and Materials Conference, Denver, CO, April 2002.